UNIVERSITY OF SOUTHAMPTON

FACULTY OF ENGINEERING AND THE ENVIRONMENT

Aerodynamics and Flight Mechanics

Interacting Synthetic Jets:
Fundamentals and Applications

by

Tim Berk

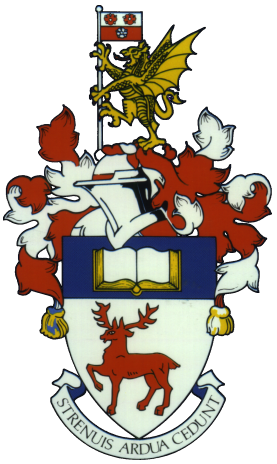

Thesis for the degree of Doctor of Philosophy

Supervised by Prof. B. Ganapathisubramani

November 14, 2017

UNIVERSITY OF SOUTHAMPTON

ABSTRACT

FACULTY OF ENGINEERING AND THE ENVIRONMENT
Aerodynamics and Flight Mechanics

INTERACTING SYNTHETIC JETS
FUNDAMENTALS AND APPLICATIONS

by Tim Berk

Synthetic jets are zero-net-mass-flux devices that create a train of vortical structures from alternating blowing and suction cycles through an orifice. In this thesis the interaction of synthetic jets with three different flows is investigated: neighbouring synthetic jets interacting with each other, a synthetic jet interacting with the separated flow over a backward-facing step and the interaction of a synthetic jet with a turbulent boundary layer. In general, for these different flows, it is proposed that the vortical structures of the jet are the leading driver behind observed interactions. This supplements the literature where interactions are often explained based on the low pressure behind jet pulses, viscous blockage of jet pulses or frequency modes amplified by the jet frequency. Using the physical mechanisms presented in this thesis, a higher level of control over interacting synthetic jets can be obtained. This includes control over the direction of two parallel synthetic jets, control over the reattachment length of the separated flow behind a backward-facing step and control over the trajectory and the wake of a synthetic jet issuing into a turbulent boundary layer. The focus in the present thesis is on the physical mechanisms behind observed interactions rather than on optimal control. The underlying idea is that the obtained physical understanding can be used in subsequent studies to develop optimal control.

Contents

List of Figures

List of Tables

Declaration of Authorship

I, Tim Berk, declare that the thesis entitled *Interacting Synthetic Jets, Fundamentals and Applications* and the work presented in the thesis are both my own, and have been generated by me as the result of my own original research. I confirm that:

- this work was done wholly or mainly while in candidature for a research degree at this university;
- where any part of this thesis has previously been submitted for a degree or any other qualification at this university or any other institution, this has been clearly stated;
- where I have consulted the published work of others, this is always clearly attributed;
- where I have quoted from the work of others, the source is always given. With the exception of such quotations, this thesis is entirely my own work;
- I have acknowledged all main sources of help;
- where the thesis is based on work done by myself jointly with others, I have made clear exactly what was done by others and what I have contributed myself, as outlined in Chapter 4;
- parts of this work have been published or submitted for publication as outlined in Chapter 4;

Signed:.....

Date:.....

Acknowledgements

I owe some thanks to Google, for without it I would have never known about the existence of professor Ganapathisubramani or even the University of Southampton.

Above all I like to thank my supervisor, Bharath, to whom I am grateful for giving me the opportunity to do this PhD in the first place and all the opportunities he has given me since. Thanks for giving me your trust when flying me across the world while at the same time trying to keep me with both feet on the ground.

I am grateful for all the good and smart PhDs and postdocs I have worked with in Southampton. I made sure to learn something from each of you and hope I have been of some help in return.

Thanks to Guillaume in particular who helped me jumpstart the PhD by working together on discovering the vibrant world of synthetic jets and showing me how to do experiments.

Thanks to Phillipe and Ronnie for welcoming me in Toronto, both inside the university and outside.

Thanks to Ivan and Nick for giving me the opportunity to work in an amazing facility in Melbourne and to Bagus, Rio and Charitha for always being ready to help.

To whomever reads this, thanks for opening my thesis. Please don't forget to read past the acknowledgements.

Thank you to my family and friends back home who understand and/or accept that I choose to live abroad.

Last but not least, a big thanks to my parents who have always stimulated me to keep learning and not be afraid to live far away.

I feel happy that luck has been on my side, almost every step of the way, for

"I am a great believer in luck,
and I find the harder I work
the more I have of it."
– Thomas Jefferson

Part I

Introduction

1. Overview

The core of this thesis consists of four papers (two published, one under review and one in preparation) that investigate the physics behind multiple applications of interacting synthetic jets. The first paper, *Vectoring of parallel synthetic jets: a parametric study*, studies the interaction between two synthetic jets. When actuated with a phase difference between their actuation cycles, the symmetry between the vortex pairs of the two jets is removed and the resulting jet can be vectored and/or bifurcated, driven by the trajectories of the produced vortices. The second paper, *Entrainment effects in periodic forcing of the flow over a backward-facing step*, investigates the interaction of a synthetic jet with a separated flow. The vortices created by the synthetic jet induce entrainment of momentum into the separation region, reducing the reattachment length. The third and fourth papers consider the interaction between a synthetic jet and a smooth-wall turbulent boundary layer. In the third paper, *Trajectory of a synthetic jet issuing into high Reynolds number turbulent boundary layers*, scaling of the trajectory of the jet with cross-flow and actuation parameters is explored. The relevant non-dimensional group containing the frequency – which is the distinctive parameter of a synthetic jet compared to a steady jet – shows that the ratio of the size of the created vortical structures to the separation between subsequent structures is important. For the fourth paper, *Effects of vortex-induced velocity on the wake of a synthetic jet issuing into a turbulent boundary layer*, the velocity deficit caused by a synthetic jet in a cross flow is investigated. A reconstruction from measurement data, as well as a predictive inviscid-flow model shows that the velocity field around a synthetic jet in a cross flow is dominated by the velocity induced by the vortical structures of the jet.

The unifying concept between the physical mechanisms identified in each paper is that all these interactions are driven by the vortical structures of the jet. This is in contrast to most of the literature where the importance of these vortical structures is often overlooked (e.g. vectoring based on pressure differences, control of separation based on amplified frequency modes, trajectory based on velocity ratio and momentum deficit based on viscous blockage). The goal of the present work is not to disprove these mechanisms given in the literature but rather to propose additional, possibly leading order, driving physical mechanisms.

The thesis consists of two parts, with Part I providing an introduction and Part II containing the four papers. Following this overview, a background is presented in Chapter 2 to introduce the concepts of synthetic jets, separated flows and turbulent boundary layers and motivate the studies presented in Part II. Next, the used experimental techniques and set-ups are described in Chapter 3. The conclusions and author contributions per paper are presented in Chapter 4.

In Part II the papers are presented with the text as published (Papers 1 and 2), submitted for review (Paper 3) or under preparation (Paper 4). This implies that some introductions, definitions and equations are repeated multiple times. Since each paper has its own introduction, the introduction to the thesis is kept brief to minimise redundancy. Where equal symbols are used with different meaning in different papers this is clearly stated in the Nomenclature.

2. Background

This chapter introduces the most important concepts used in the present thesis. First, a brief general introduction into synthetic jets is given along with some specific aspects of synthetic jets used in this work. Next, the state of the literature on the interaction between two synthetic jets as studied in Paper 1 is discussed. Then, actuation of separated flows as investigated in Paper 2 is reviewed and the gap in the literature this paper addresses is identified. Finally, high-Reynolds number turbulent boundary layers and their importance are discussed. The need for – and state of skin-friction control in these boundary layers is discussed and the motivation for Papers 3 and 4 is presented.

2.1 Synthetic jets

Fluid pushed through an orifice creates a vortex ring at the edge of the orifice driven by the roll-up of its shear layers (e.g. Saffman and Baker (1979)). Repeated blowing pulses lead to a train of vortex rings that are advected downstream by their self-induced velocity, break-down at some distance away from the orifice and form a turbulent jet (Glezer and Amitay, 2002). Synthetic jets are similar to pulsed jets with the distinction that blowing pulses are followed by equal suction pulses such that vortical structures are formed entirely from the working fluid (Smith and Glezer, 1998). A schematic of a synthetic jet actuator is presented in Figure 2.1(a). Under the right conditions, the vortical structure created by a blowing pulse is far enough away from the orifice at the onset of suction to prevent it from being re-ingested (Holman et al., 2005). The zero-net-mass-flux jet that is created under these conditions has non-zero net momentum flux and can be used as an actuator for flow control (Cattafesta and Sheplak, 2011). One of the advantages of synthetic jets over pulsed jets or steady jets is that the former does not require a fluid supply.

2.1.1 Actuators and actuation types

Synthetic jet actuators consist of a cavity bounded by a driver and an orifice (see Figure 2.1(a)). Typical drivers include pistons, piezoelectric membranes or loudspeakers (Cattafesta and Sheplak, 2011). These drivers are actuated using an oscillating

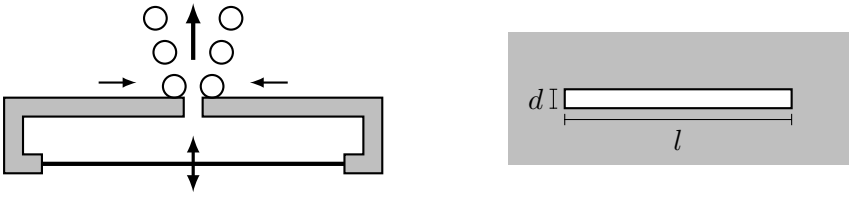

(a) Side view (b) Top view

Figure 2.1: Schematic of synthetic jet actuator consisting of a cavity with an oscillating driver and an orifice at which a vortex pair/vortex ring is formed.

waveform, causing the effective cavity volume to vary accordingly and driving the time-periodic flow through the orifice. In the present thesis a loudspeaker with a sinusoidal actuation waveform is used. It can be assumed that this generates a near-sinusoidal velocity at the jet exit (see for example velocity cycles in Smith and Glezer (1998); Milanovic and Zaman (2005); Carpy and Manceau (2006); Yang (2009); Goodfellow et al. (2013)). This sinusoidal velocity can be fully described by a frequency f and a velocity magnitude $\bar{u}$. In the present work the mean blowing velocity of the jet is used as the relevant velocity magnitude, which is analogous to a slug model of the synthetic jet as employed by Glezer (1988). The velocity profile across the jet exit can be described as a constant (top-hat) profile which only decreases near the edge of the jet due to the internal boundary layers at the sides of the orifice (see for example velocity profiles in Shuster et al. (2005); Zhou et al. (2009); Jabbal and Zhong (2010); Kim et al. (2012); Lawson and Dawson (2013)). This implies that across a small orifice dimension the velocity profile is parabolic (as in fully developed channel flow), while across a large orifice dimension the profile can be assumed constant. The velocity distribution across the slot is not considered in any of the studies in this thesis. Instead, the jet-centreline velocity is used to characterize the jet.

2.1.2 Rectangular orifice

Most studies consider synthetic jets through an axisymmetric orifice. The present work uses finite-span rectangular orifices (also called slots). These rectangular orifices have a slot length l and a slot width d as defined in Figure 2.1(b). Rectangular synthetic jets can be advantageous over circular jets when actuating a spanwise range of a given flow or when studying the flow in a two-dimensional setting. The formation and evolution of a synthetic jet using a rectangular orifice has been studied by Amitay and Cannelle (2006) and Van Buren et al. (2014a,b). These jets create a rectangular vortical structure which deforms due to its asymmetry in induced velocity and switches its minor and major axes at some point downstream. This three-dimensional effect starts at the far edges of the rectangular orifice and travels towards the centre of the vortical structure as the structure travels downstream (Amitay and Cannelle, 2006). Van Buren et al. (2014a) showed the effect of aspect ratio on the three-dimensional development of the jet. At

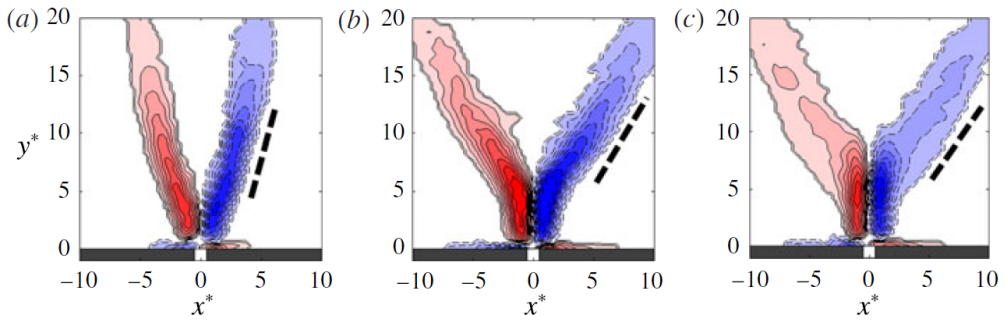

Figure 2.2: Effect of slot length on the streamwise development at the centreline of the jet ($z^* = 0$). x^*, y^* and z^* are normalized by the slot width (in x-direction). Slot lengths (in z-direction) equal l^* = (a) 6, (b) 12, and (c) 18. Red and blue contours represent positive and negative vorticity respectively. Taken from Van Buren et al. (2014a).

the centreline (see Figure 2.2) of the jet, the jet exits the orifice in vertical direction up to some distance which increases with aspect ratio. Beyond this point the jet starts to spread due to axis switching (the three-dimensional effect originating from the far edges of the orifice). The distance from the orifice where these three-dimensional effects reach the centreline can be determined from Figure 2.2 to be approximately equal to $y^* = y/d$ = (a) 3, (b) 6, and (c) 9, corresponding to slot lengths of $l^* = l/d$ = 6, 12 and 18 respectively. This shows that the flow can be assumed two-dimensional up to a distance of $l/2$ downstream.

2.1.3 Relevant parameters

When using a rectangular synthetic jet with a sinusoidal velocity profile, the flow of a single synthetic jet issuing into quiescent fluid can be described using three non-dimensional parameters (Glezer and Amitay, 2002): the aspect ratio, Strouhal number and Reynolds number, defined as

$$AR = l/d, \tag{2.1}$$

$$St = fd/\bar{u}, \tag{2.2}$$

$$Re = \bar{u}d/\nu. \tag{2.3}$$

In the literature, the non-dimensional stroke length, $L/d = \bar{u}/(fd)$ is often used instead of the Strouhal number (note that $L/d = 1/St$).

2.1.4 Formation criterion

When the ratio of the velocity of the jet to the frequency of the jet is too low, the created vortical structures do not have sufficient time to escape the subsequent suction part of the cycle and will be re-ingested into the actuator. A formation criterion has been proposed by Holman et al. (2005), who demonstrated that for $St > 1/\pi$ no time-averaged jet is formed. Throughout the papers presented in this thesis it is observed that

the vortical structures created by the synthetic jet decrease in strength when approaching this criterion.

2.1.5 Vortex formation

The circulation created at the jet exit is given by $\mathrm{d}\Gamma/\mathrm{d}t \approx u^2(t)/2$ (Shariff and Leonard, 1992), which is the circulation in the shear layers of the jet. These shear layers roll up into a vortical structure. At some point this vortical structure will pinch off (separate) from the trailing shear layer, meaning that the circulation in the vortical structure stops growing. Gharib et al. (1998) proposed a constant formation number at which this pinch-off occurs, $L/D \approx 4$ where D is the diameter of a circular orifice. O'Farrell and Dabiri (2014) demonstrated that this formation number holds for a rectangular orifice when expressed as L/D_{eq} where D_{eq} is the equivalent diameter of a circular orifice with the same cross-sectional area. In addition to this limit on the size of a vortex, Aydemir et al. (2012) proposed a limiting time-scale at which pinch-off occurs for synthetic jets. Using sinusoidal forcing, they found this time-scale to be $t/T = 1/3$, where $T = 1/f$ is the period of actuation. A vortical structure is assumed to pinch off at either $L/D_{eq} = 4$ or $t/T = 1/3$, whichever happens first.

2.2 Interaction between two jets

The interaction between two parallel (rectangular) jets is considered at the centreline of the jets and treated as a two-dimensional flow. As discussed above, three-dimensional effects originating at the far edges of the slot reach the centreline at a distance of $l/2$ downstream, where l is the length of the slot (Van Buren et al., 2014a). It is assumed that the flow is fully two-dimensional for $r < l/2$, where r is the radial distance from the orifice.

2.2.1 Merging

In a two-dimensional view, the vortex ring created by a synthetic jet appears as a counter-rotating vortex pair. For two neighbouring synthetic jets actuated with equal frequency, amplitude and phase, two counter-rotating vortex pairs are created. When the actuators are spaced close enough to each other, the inner-vortices – of opposite signed vorticity – will cancel and the two jets merge into a single, larger jet (Smith and Glezer, 1998) (see Figure 2.3(a)).

2.2.2 Vectoring

When one of the jets is leading in phase (i.e. a time-lag between the jet cycles), the symmetry between the jets is removed and the jets are vectored towards the leading

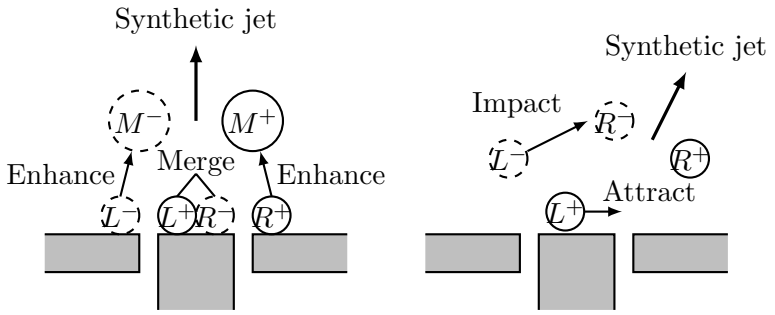

(a) Enhancing mechanism (b) Vectoring mechanism

Figure 2.3: Interaction mechanisms between synthetic jets, taken from Berk et al. (2016) redrawn from Luo and Xia (2008). Synthetic jets in absence of a phase difference, leading to an enhanced merged jet (a) and synthetic jets with a phase difference, leading to a vectored jet (b).

jet (Smith and Glezer, 2005; Luo and Xia, 2008). Luo and Xia (2008) proposed a vectoring mechanism in which the lagging vortex pair is attracted by the low-pressure region of the leading vortex pair. This attraction leads to the lagging pair impacting on the leading pair at an angle, thereby vectoring the resultant jet towards the leading actuator (see Figure 2.3(b)). For an increasing phase difference from 60° to 150° the vectoring angle keeps growing until the resultant jet is fully attached to the surface (Smith and Glezer, 2005). The effect of variations in the Strouhal number of the jets, Reynolds number of the jets and spacing between the two actuators on the vectoring behaviour is investigated in Berk et al. (2016) (Paper 1) where an alternative physical mechanism is proposed based on vortex trajectories and their induced velocity.

2.3 Interaction with a separated flow

The low pressure in the separated flow behind a bluff body accounts for a substantial amount of the drag on the body and can account for up to 50% of fuel consumption in road-based transport (Hucho and Sovran, 1993). Two control strategies for drag reduction are common in the literature: increasing the pressure recovery (i.e. decreasing the length of the separation region) or streamlining the virtual body (i.e. increasing the length of the separation region) (Barros et al., 2016b). It has been shown that periodic forcing can be used to control the length of the separation region using for example an oscillating flap (Nagib et al., 1985), pulsed jets (Barros et al., 2016a,b), plasma actuators (Roupassov et al., 2009) or synthetic jets (Chun and Sung, 1996; Dandois et al., 2007; Henning and King, 2007; Dahan et al., 2012; Oxlade et al., 2015).

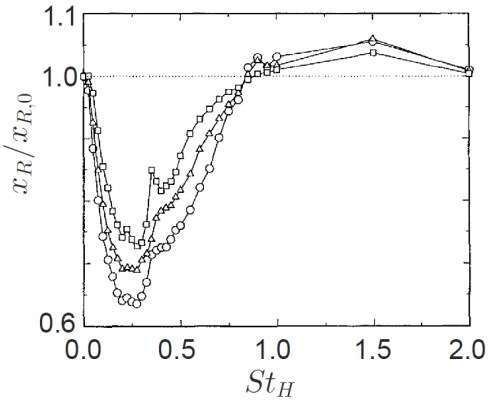

Figure 2.4: Effect of step-based Strouhal number on reattachment length for three forcing amplitudes. Adapted from Chun and Sung (1996).

2.3.1 Effect of frequency

Classically, the effect of forcing on the flow has been described as the actuation or amplification of different frequency-modes naturally occurring in the flow (Nagib et al., 1985; Kiya et al., 1993; Chun and Sung, 1996). The reattachment length normalized by the unforced length $x_R/x_{R,0}$ as function of the step-based Strouhal number St_H ($St_H = fH/U_\infty$ where H is the step height) as measured by Chun and Sung (1996) is presented in Figure 2.4. The reattachment length shows a clear minimum between $0.2 < St_H < 0.3$, recovers to the unforced length around $St_H \approx 0.8$, is slightly increased for larger Strouhal numbers and ultimately returns to the unforced length. In this curve Chun and Sung (1996) observed two actuated frequency-modes corresponding to the two minima around $St_H \approx 0.27$ and $St_H \approx 0.40$. The main minimum, around $St_H \approx 0.27$ is observed to be associated with the shedding frequency of the separated shear layer (Nagib et al., 1985). Actuation at this frequency would increase the shear-layer growth rate (Chun and Sung, 1996) and lead to a reduction of the reattachment length.

2.3.2 Reduction of perturbations

More recently, an effect of periodic forcing (using synthetic jets) on perturbations in the incoming flow has been observed. Rathnasingham and Breuer (2003) showed that synthetic jets can dampen the fluctuations in the incoming flow, leading to a reduction of up to 30% in the streamwise velocity fluctuations. Using high-frequency forcing ($St_H = 1.15$) of the separated flow over a backward-facing ramp Dandois et al. (2007) observed a lower amplitude of velocity fluctuations. This reduction in fluctuations causes an increase in reattachment length, explaining the overshoot observed for high Strouhal numbers in Figure 2.4. Similar results are observed for the separating flow over a backward-facing step using both large-eddy simulations (LES) (Dahan et al., 2012) and particle image velocimetry (PIV) (Vukasinovic et al., 2010). This effect has been observed up to high

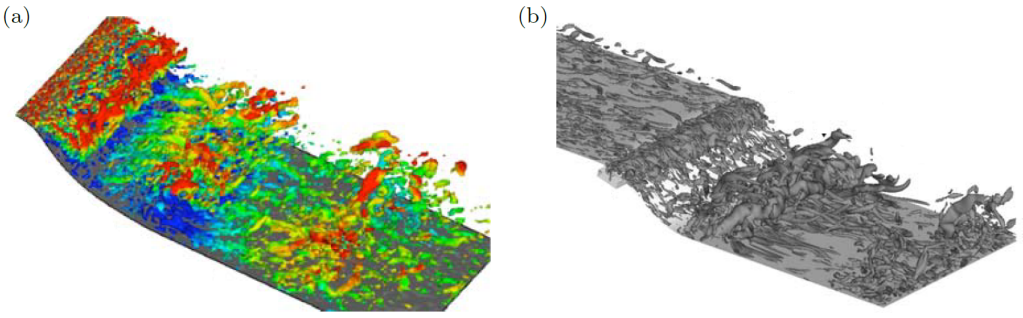

Figure 2.5: LES results showing vortical structures of periodically-forced separated flow over a backward-facing ramp. Taken from Avdis et al. (2009) (a) and Dandois et al. (2007) (b).

frequencies far beyond the formation criterion for synthetic jets discussed above, where no vortical structures are created by the jet but the actuator influences the flow through acoustic waves (Dandois et al., 2007).

Advances in both computational (DNS, LES) and experimental (PIV) techniques over the past decades have aided the qualitative and quantitative study of flow fields. Results from large-eddy simulations by Avdis et al. (2009) and Dandois et al. (2007) indicating vortical structures in the periodically forced separating flow over a backward-facing ramp are presented in Figure 2.5. These instantaneous snapshots show iso-contours of the Q-criterion which highlights vortices by taking the difference between the vorticity tensor and the rate-of-strain tensor. Both results show an incoming turbulent flow upstream of the ramp, identified by the homogeneously distributed vortical structures. Periodic forcing at the edge of the ramp groups the vortical structures into distinct spanwise-aligned regions associated with the vortical structures created by the forcing. An important feature of this low-frequency forcing is the reattachment of the flow between subsequent vortical structures. This reattachment between spanwise-aligned vortical structures has also been documented for experimental studies, using PIV in streamwise–wall-normal planes (Yoshioka et al., 2001).

2.3.3 Entrainment effect

The observed reattachment between subsequent vortical structures created by the jet suggests that the flow is not dominated by a spatially growing shear layer as was proposed by Nagib et al. (1985), Kiya et al. (1993) and Chun and Sung (1996). It can be argued that these vortical structures carry high-momentum fluid from the free stream towards the wall by an entrainment effect (Dandois et al., 2007). This entrainment of high-momentum fluid leads to an increase of momentum in the separation region and subsequently to a reduction in the (time-averaged) reattachment length. Using this momentum entrainment driven by vortices, the shape of the curve in Figure 2.4 for $0 < St_H < 0.8$ might be explained by the effect of Strouhal number on the ability to entrain momentum into the separation region instead of by specific frequency-modes.

In fact, close inspection of Figure 2.4 shows that two small peaks at $St_H \approx 0.27$ and $St_H \approx 0.40$ are superimposed on the general shape of the graph. It may be assumed that these small peaks correspond to the actuation of frequency-modes as proposed in the past while the general shape of the curve is driven by the entrainment of momentum. The effect of the Strouhal number on the entrainment of momentum and on the reattachment length is studied in Berk et al. (2017b) (Paper 2) where it is proposed that the shape of the curve in Figure 2.4 for $0 < St_H < 0.8$ can be recreated based on this entrainment effect.

2.4 Interaction with a turbulent boundary layer

Frictional drag caused by turbulent boundary layers accounts for up to 50% of the drag on modern airliners (Marusic et al., 2010a), up to 90% of the drag on some ship types (Schultz, 2007) and up to 100% of losses in pipe lines (Gad-el-Hak, 1994). Worldwide the shipping industry consumes over 2 billion barrels of oil per year and the airline industry over 1.5 billion barrels of jet fuel (numbers from over a decade ago) (Kim and Bewley, 2007). Given the direct link between drag and fuel expenditure, the potential savings resulting from even a small reduction in skin-friction drag are enormous. In order to achieve such a reduction, turbulent boundary layers need to be better understood and efficient control strategies need to be developed.

2.4.1 Experiments versus applications

One of the challenges in turbulent boundary layer research is the difference in orders of magnitude between lab-experiments and practical applications (Gad-el-Hak, 2007). As a reference the Reynolds number $Re_L = LV/\nu$, based on total length L and cruising speed V, for both an Airbus A320 (the most common airliner) and a large oil tanker are presented in Table 2.1. In general Reynolds numbers in the shipping and airline industry are of $\mathcal{O}(10^9)$. Comparable Reynolds numbers of three world-leading high-Reynolds number boundary layer research facilities are presented based on the test-section length, maximum velocity and kinematic viscosity of the working fluid. These facilities, the pressurised superpipe at Princeton University, the high-Reynolds number boundary layer wind tunnel at the University of Melbourne and the long pipe facility at CICLoPE have Reynolds numbers of $\mathcal{O}(10^8)$ (although the CICLoPE pipe is approaching Reynolds numbers of airliners and smaller ship types). This can be compared to a Reynolds number for more common research facilities such as the wind tunnels at the University of Southampton of $\mathcal{O}(10^7)$. On top of this mismatch in Reynolds numbers between (common) experimental facilities and practical applications, measurement of the full range of length scales present in a high-Reynolds number turbulent boundary layer is a challenge due to the decreasing size of the smallest scales for increasing Reynolds numbers as will be discussed below. This means that these scales can not

Table 2.1: Examples of Reynolds numbers based on length and bulk velocity for an Airbus A320, a large oil tanker, pressurized superpipe facility at Princeton University, high-Reynolds number boundary layer facility at the University of Melbourne, the Long Pipe Facility at the Center for International Cooperation in Long Pipe Experiments (CICLoPE) and the $3' \times 2'$ wind tunnel at the University of Southampton.

		L (m)	V (m/s)	ν (m^2/s)	Re_L
Airbus A320	Airbus (2017)	38	230	$1.5 \cdot 10^{-5}$	$0.6 \cdot 10^9$
Oil tanker	Monty et al. (2016)	320	8.7	$0.9 \cdot 10^{-6}$	$3.1 \cdot 10^9$
Superpipe	Jiménez et al. (2010)	2.40	10	$1.3 \cdot 10^{-7}$	$0.2 \cdot 10^9$
HRNBLWT	Nickels et al. (2005)	27	45	$1.5 \cdot 10^{-5}$	$0.1 \cdot 10^9$
CICLoPE	Talamelli et al. (2009)	115	60	$1.5 \cdot 10^{-5}$	$0.5 \cdot 10^9$
$3' \times 2'$		4.4	30	$1.5 \cdot 10^{-5}$	$0.01 \cdot 10^9$

be accurately measured with conventional measurement techniques (Fan et al., 2015). These complexities along with the technological importance make the research field of turbulent boundary layers a very actively studied field where the knowledge has drastically increased over the past decades, aided by the development of new facilities and measurement techniques (Marusic et al., 2010b).

2.4.2 Near-wall streaks

Two distinct wall-normal regions can be identified in turbulent boundary layers: a viscous-dominated near-wall or inner region and an outer region in which viscosity plays only a small role (e.g. Smits et al. (2011)). The relevant scaling parameters for the viscous inner layer are the kinematic viscosity ν and the friction velocity $U_\tau = \sqrt{\tau_w/\rho}$ where τ_w is the mean wall-shear stress and ρ is the fluid density. These can be combined as an inner length scale ν/U_τ and time scale ν/U_τ^2 (e.g. Klewicki (2010)). Relevant scaling parameters for the outer region are the boundary layer thickness δ and the free stream velocity U_∞ (combined in an outer time scale δ/U_∞). For wall-bounded turbulence the most relevant Reynolds number is the friction Reynolds number $Re_\tau = \delta U_\tau/\nu$, which is the ratio of the outer and inner length scales (e.g. Marusic et al. (2010a)). These different length scales can be observed in a spectrogram as presented in Figure 2.6. These spectrograms show the premultiplied energy associated with fluctuations of a given streamwise length scale λ_x at a wall-normal location y. These length scales are presented normalised by the outer length scales λ_x/δ as well as the inner length scales λ_x^+ where superscript + denotes normalization with inner variables (i.e. $\lambda_x^+ = \lambda_x U_\tau/\nu$, $y^+ = yU_\tau/\nu$). For both presented Reynolds numbers an inner peak is visible (white cross) which is centred around $y^+ = 15$ and $\lambda_x^+ = 1000$. This peak is caused by a type of coherent structures referred to as inner streaks with a typical streamwise length of $\lambda_x^+ = 1000$ and a spanwise scale of $\lambda_z^+ = \mathcal{O}(100)$ (e.g. Marusic et al. (2010b)). An example of these structures is presented in Figure 2.7a (bottom left), based on DNS of a channel flow. This figure shows velocity fluctuations near the wall (bottom left), further away from the wall (top left) and the same but with a spatial filter applied,

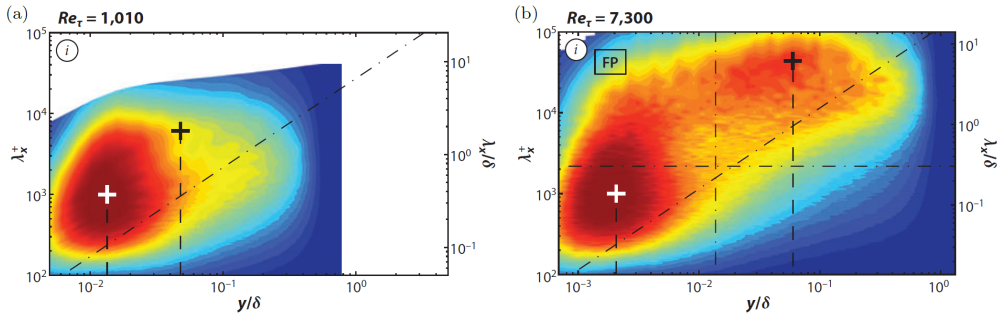

Figure 2.6: Spectrograms of premultiplied energy associated with fluctuations of streamwise length λ_x as function of wall-normal location y for $Re_\tau = 1010$ (a) and 7300 (b). Taken from Smits et al. (2011) where it was adapted from Hutchins and Marusic (2007a).

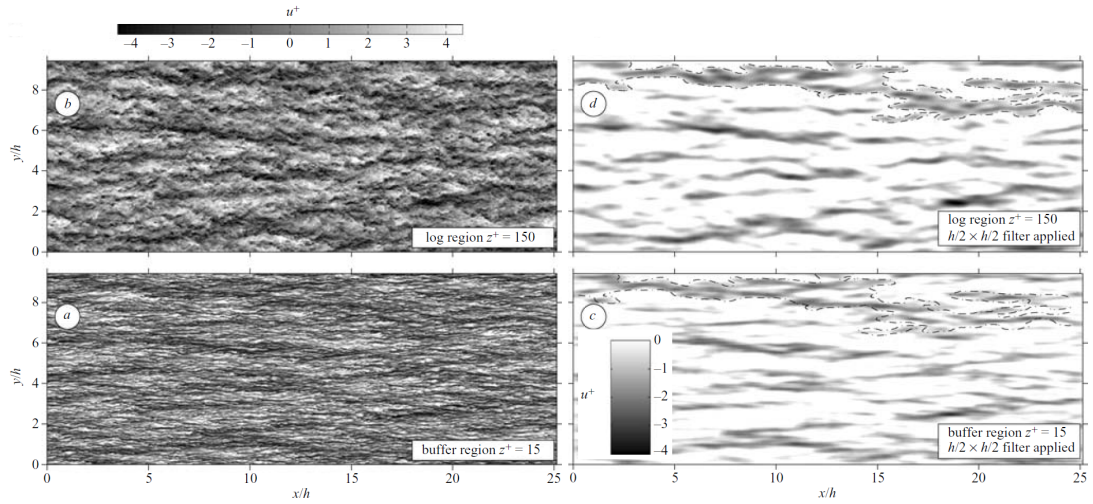

Figure 2.7: Velocity fluctuations near the wall (a, bottom left) and further away from the wall (b, top left). Same fluctuations but with a spatial filter applied (c and d, right). Adapted from Hutchins and Marusic (2007a) based on del Álamo et al. (2004).

highlighting large structures (right). These inner streaks, close to the wall, are generally assumed to be directly responsible for most of the turbulent friction drag and are therefore the focus of most control strategies (Kasagi et al., 2009; Smits et al., 2011). For increasing Reynolds numbers (as encountered in practical applications), U_τ generally increases and the inner length scales become smaller (Head and Bandyopadhyay, 1981) and subsequent down-scaling of sensors and actuators to match these length scales becomes a challenge (Abbassi et al., 2017). For example, Rathnasingham and Breuer (2003) developed an actuator for fluidic control of near-wall streaks with an orifice measuring $l_x^+ = 150$ by $l_z^+ = 10$ (8 by 0.6 mm), based on the characteristics of the flow in their wind-tunnel experiment. Scaling these dimensions for application on the oil tanker mentioned in Table 2.1 ($U_\tau \approx 0.5$ m/s, $\nu \approx 0.9 \cdot 10^{-6}$ m^2/s (Monty et al., 2016)) would result in a required orifice dimension of 0.3 mm by 18 µm which is at the least very demanding, if not technologically impossible with currently existing techniques.

2.4.3 Large-scale structures

For increasing Reynolds numbers (Re_τ) a second peak can be identified in the premultiplied energy spectrograms (peak visible in Figure 2.6b, black cross) at a wall-normal location of about $y/\delta = 0.06$ and corresponding to a wavelength of $\lambda_x/\delta = 6$. Hutchins and Marusic (2007a) proposed that while this peak indicates a streamwise wavelength of $\lambda_x/\delta = 6$, the measured length of the corresponding structures might be smaller than their actual length due to spanwise-meandering of the structure, causing it to move into and out-of the sensor location. Their actual length is observed to be around $\lambda_x/\delta = 20$ and is often referred to as the more general $\lambda_x/\delta = \mathcal{O}(10)$ (Marusic et al., 2010b). Due to these structures being orders of magnitude larger than the previously discussed inner streaks, they are usually termed either very large-scale motions (VLSMs, Kim and Adrian (1999)) or superstructures (Hutchins and Marusic, 2007a). A schematic of these large-scale structures is presented in Figure 2.8 where low- and high-speed streaks are drawn in blue and red respectively. These large-scale structures in the outer region have been found to correlate with small-scale structures in the near wall region (Hutchins and Marusic, 2007b; Mathis et al., 2009; Ganapathisubramani et al., 2012) as well as with the skin friction at the wall (Hutchins et al., 2011). These small-scale structures are indicated in grey in Figure 2.8. The top-right plot of this figure indicates a time series of velocity data. This velocity data is decomposed into large- and small-scale contributions in the lower two plots. The envelope of the small-scale signal is well described by the large-scale signal, indicating modulation of the small-scales by the large-scales. Some correlations between small-scales and large-scales can also be observed in Figure 2.7 where a spatial filter is applied to fluctuations, highlighting only large-scale fluctuations (right plots). These large-scale fluctuations correlate with the small-scale fluctuations (left plots). The interaction between large-scale structures in the outer layer and small-scale structures in the inner layer has led to the development of models which predict the near-wall turbulence based on large-scale fluctuations in the outer layer (Marusic et al., 2010a; Mathis et al., 2011).

2.4.4 Control

Given this link between outer- and inner-structures it has been suggested that large-scale structures could be specifically targeted in order to control near-wall turbulence and skin-friction (Hutchins et al., 2011). The main advantage compared to direct control of near-wall streaks is that for increasing values of Re_τ as encountered in practical applications the large-scale structures grow and subsequent up-scaling of sensors and actuators is considered to be more feasible than the down-scaling required for controlling near-wall streaks. Passive control systems using large-eddy break-up devices (solid plates immersed in the outer region) have been reported to reduce local skin friction by as much as 30% through the break-up of these outer structures (Savill and Mumford, 1988). However, the pressure drag caused by such devices makes it almost impossible

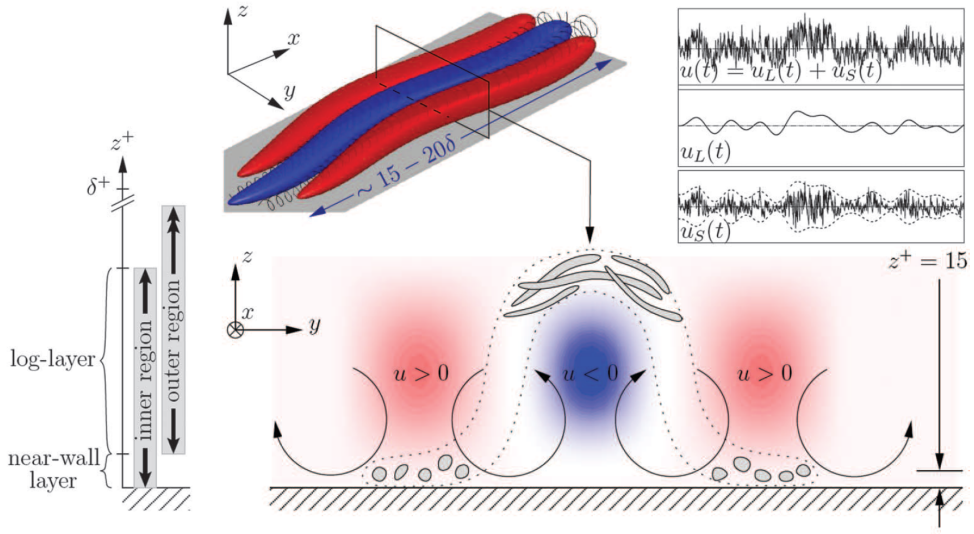

Figure 2.8: Schematic of large-scale structures and amplitude modulation. Note that y denotes spanwise direction and z wall-normal direction. Taken from Marusic et al. (2010a).

to obtain a net drag reduction. Active control using a pulsed jet has been performed by Kang et al. (2008). Using a sensor and a nozzle, both based outside the boundary layer, large-scale structures were detected and actively targeted by the jet, successfully leading to their break-up. Although this study showed the feasibility of active control of large-scale structures, wall-based control would be preferable due to practical limitations in engineering applications. Active wall-based control was performed by Abbassi et al. (2017) with both the sensor and actuator flush with the wall. Actively targeting large-scale structures locally led to a skin-friction drag reduction of 3.2% while random actuation led to a reduction of 2.4%. Given the increasing impact of outer-layer structures on skin friction for increasing Reynolds numbers (Hutchins and Marusic, 2007b; Mathis et al., 2009) as well as the enormous fuel savings even a small reduction in skin-friction drag would bring, this 3.2% reduction is assumed significant.

In order to actively target large-scale structures through impacting on them with fluidic pulses, it is important to be able to actively predict both the advection of the large-scale structures between sensor and impact location (Abbassi et al., 2017) as well as the advection of the fluidic pulse between the orifice and impact location (i.e. the trajectory). The trajectory of a pulsed jet or synthetic jet in a turbulent boundary layer has not been systematically studied in the literature. The effects of both the cross-flow parameters and actuation parameters on the trajectory of a synthetic jet issuing into a turbulent boundary layer are investigated in Berk et al. (2017a) (Paper 3).

Similar to the drag created by large-eddy break-up systems, a synthetic jet issuing into a cross flow also leads to a momentum deficit in the cross flow. In the literature this momentum deficit is often referred to as caused by viscous blockage (e.g. Lardeau

and Leschziner (2011)) or by the vortex-induced up-wash of low-momentum fluid (e.g. Rathnasingham and Breuer (2003)). However, these are qualitative descriptions and do not quantify the momentum deficit in detail. Both blockage and up-wash depend on the geometry of the vortical structures created by the jet. The vortical structures created by the interaction of a synthetic jet with a laminar boundary layer have been mapped on to a parameter space by Sau and Mahesh (2008) (based on numerical simulations) and Jabbal and Zhong (2008) (based on experiments). Depending on the actuation conditions, these structures can be classified as hairpin vortices, vortex rings or a combination of the two. The type of vortical structures created by a synthetic jet issuing into a turbulent boundary layer, and more specifically the momentum deficit these structures cause in the cross flow is studied in Berk and Ganapathisubramani (2017) (Paper 4). An additional source of momentum deficit is proposed: a velocity induced by the vortical structures in the direction opposite to the cross flow. Evidence is presented that this newly proposed source is in fact the leading source of the momentum deficit created by a synthetic jet in a cross flow. A physical understanding of this momentum deficit aids the optimisation of active control of large-scale structures by minimizing the momentum deficit and maximizing the net drag reduction.

3. Experimental Set-Up and Procedures

This chapter gives a detailed overview of the experimental set-up and procedures used in each of the papers presented in Part II of the thesis. First, the two used actuators are discussed. Then, the facilities and measurement set-ups are described. Finally, a general description of the used measurement techniques is given.

3.1 Actuators

In this thesis, the same actuator design in used for Papers 1, 3 and 4 and a separate design for Paper 2. Both actuators are driven by Visaton SC 8 N loudspeakers, actuated with a sinusoidal voltage signal. This 8 Ohm loudspeaker has a frequency response of 70–20000 Hz with a resonance frequency around 90 Hz, leading to a peak in the actuation response for low frequencies.

The actuator used in Papers 1, 3 and 4 consists of a single loudspeaker attached to a circular (pancake shaped) cavity of volume 1.85×10^{-5} m^3 (see Figure 3.1). A curved converging nozzle is attached to one edge of the cavity with a neck length of $l_{neck} = 19.5$ mm and a rectangular exit slot of $l = 13$ mm by $d = 1$ mm ($AR = 13$). This combination of cavity and nozzle leads to a fluidic (Helmholtz) resonance frequency of approximately 550 Hz as determined from exit velocity measurements. The cavity is milled out of aluminium and the nozzle is 3D printed. The accuracy of the used 3D printing technique is 0.1 mm, which has an impact on the exact orifice dimensions as well as on the exit radius of the nozzle.

The actuator used in Paper 2 consists of three loudspeakers placed side-by-side, attached to a single cavity of volume 1.2×10^{-4} m^3 (see Figure 3.2). The cavity is connected to a straight converging nozzle of neck length $l_{neck} = 6$ mm and slot exit dimensions of $l = 230$ mm by $d = 0.5$ mm ($AR = 460$). This combination of cavity and nozzle leads to a fluidic (Helmholtz) resonance of approximately 470 Hz. Both the cavity and the nozzle are milled out of aluminium plates.

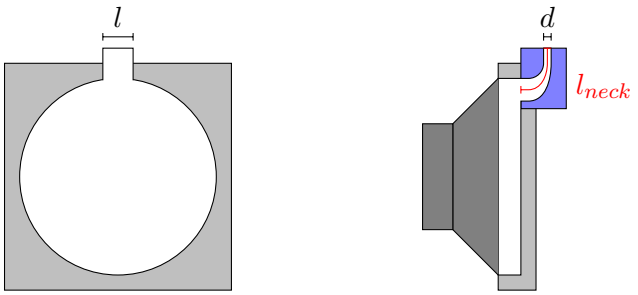

(a) Frontal view (b) Side view

Figure 3.1: Schematic of actuator used in Papers 1, 3 and 4, indicating the cavity (white), aluminium plates (light grey), 3D-printed nozzle (blue) and speaker (dark grey) as well as the slot length l, slot width d and neck length l_{neck} (not to scale).

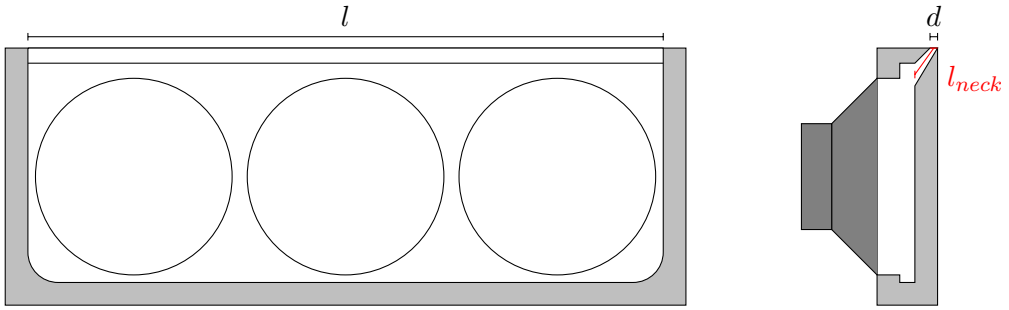

(a) Frontal view (b) Side view

Figure 3.2: Schematic of actuator used in Paper 2, indicating the cavity (white), aluminium plates (light grey) and speaker (dark grey) as well as the slot length l, slot width d and neck length l_{neck} (not to scale).

The synthetic jets are calibrated by measuring their exit velocity as function of input voltage and frequency. This exit velocity is measured using hot-wire anemometry which is discussed below. See Paper 3 for a discussion on how to accurately determine the jet velocity.

3.2 Facilities

A different facility and/or set-up is used for each paper presented in Part II of this thesis. This section lists the used facilities and set-ups.

3.2.1 Table-top set-up

A table-top type set-up is used in Paper 1. A schematic of this set-up is presented in Figure 3.3. In this set-up two synthetic jet actuators are placed next to each other with a variable spacing Δ such that the nozzle exits are parallel to each other and both flush and perpendicular to the surface. A purpose-build cubic perspex box with

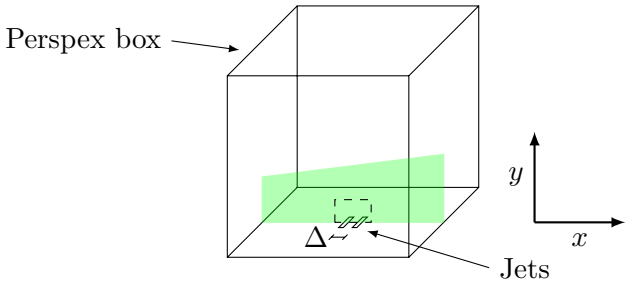

Figure 3.3: Schematic of the table-top set-up used in Paper 1 (not to scale).

sides of 0.4 m is placed over the actuators with the goal of confining tracer particles. It is assumed that this box is large enough not to influence the flow in the near-field of the jets which is studied in this paper. The box is seeded by a Martín Magnum 1200 smoke machine, ejecting particles with a mean diameter of 1 µm. Particles in the centreline plane of the jets are illuminated using a Litron 200 mJ dual-pulse Nd-YAG laser. A LaVision ImagerProLX 16MP camera is positioned perpendicular to the laser sheet to perform planar-PIV measurements (PIV, particle image velocimetry is discussed below). A 105 mm focussing lens is used, giving a field-of-view of approximately 45 mm by 30 mm. Images are captured and processed using LaVision DaVis 8.2.2. Velocity vectors are calculated using an initial window size of 64×64 pixels, followed by two steps of 32×32 pixels with 50% overlap, resulting in a velocity field with a resolution of 0.16 mm per vector. Presented velocity (and vorticity) fields are averaged over 100 instantaneous measurements, converging the uncertainty in the repeatability to the same order of magnitude as the uncertainty in the instantaneous measurements.

3.2.2 $3' \times 2'$ wind tunnel

The $3' \times 2'$ wind-tunnel facility at the University of Southampton is used in Papers 2 and 4. This suction-type open-return wind tunnel has a test-section length of 4.5 m with a span of 0.9 m and a height of 0.6 m (hence the name $3' \times 2'$, referring to the cross-sectional dimensions in imperial units).

Flat plate

One of the configurations that can be installed in this wind tunnel is a flat plate, lifted from the floor by approximately 0.14 m. This 4.2 m long plate, spanning the entire width and almost the entire length of the test-section has a sharp leading edge fitted with a boundary-layer trip and a trailing-edge flap of which the flap angle can be adjusted. This flap angle is used to control the stagnation point at the leading edge, which is set to be at the measurement side of the plate. The boundary layer is tripped close to the leading edge using a zig-zag type boundary-layer trip. This configuration is used to

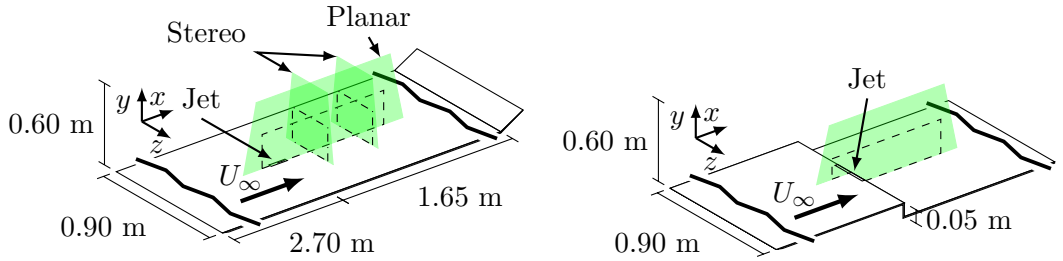

(a) Smooth-wall (b) Backward-facing step

Figure 3.4: Schematics of (a) smooth-wall turbulent boundary layer set-up as used in Paper 4 (taken from Berk and Ganapathisubramani (2017)) and (b) backward-facing step set-up used in Paper 2 (not to scale).

create a turbulent boundary layer at the top of the plate with a well-defined start point at the leading edge.

This set-up is used in Paper 4 in which the actuator is placed 2.7 m downstream of the leading edge where the boundary-layer thickness is approximately $\delta = 45$ mm for a free stream velocity of $U_\infty = 10$ m/s ($Re_\tau = 1220$). A schematic of this set-up is presented in Figure 3.4(a). The jet exit is placed flush and perpendicular to the flat plate at the spanwise centre of the tunnel with the long dimension (13 mm) aligned in streamwise direction and the short dimension (1 mm) in spanwise direction. The actuator is hanging underneath the flat plate, where it creates a blockage to the flow. The effect of this blockage on the stagnation point at the leading edge of the plate is compensated by adjusting the flap angle. The flow is seeded by a Martín Magnum 1200 smoke machine placed outside the wind tunnel. The streamwise and wall-normal velocity components at the centreline of the jet are measured using planar-PIV. This plane is illuminated using two aligned Litron 200 mJ dual-pulse Nd-YAG lasers. Particle images are captured using an array of three LaVision ImagerProLX 16MP cameras placed side-by-side, fitted with 105 mm focussing lenses. This array records a field-of-view of approximately 405 mm (streamwise direction) by 90 mm (wall-normal direction). Images are captured and processed into vector fields using LaVision Davis software. Velocity vectors are calculated with a final window size of 24×24 pixels with 50% overlap, resulting in a resolution of 0.34 mm per vector. In a separate measurement, all three velocity components are measured in spanwise–wall-normal planes located at $x = 0.135$ m and 0.270 m downstream of the actuator using stereoscopic-PIV (stereoscopic-PIV measurement technique is discussed below). This plane is illuminated by a single Litron 200 mJ dual-pulse Nd-YAG laser. Images are captured using two LaVision ImagerProLX 16MP cameras (fitted with 300 mm lenses) placed on opposite sides of the test section, directed at the laser sheet from downstream with an internal angle between the cameras of 60 degrees. The usable field-of-view recorded by the cameras is approximately 90 mm in spanwise direction and 90 mm in wall-normal direction. Velocity vectors are calculated with a resolution of 0.35 mm per vector. Presented velocity fields (and derived quantities) are averaged over

300 instantaneous vector fields per phase for eight phases.

Backward-facing step

Another configuration that can be installed in the $3' \times 2'$ wind tunnel is a backward-facing step as used in Paper 2. A schematic of this set-up is presented in Figure 3.4(b). The step of height $H = 0.05$ m spans the entire width of the wind tunnel. The incoming turbulent boundary layer has a thickness of $\delta = 74$ mm at a free stream velocity of $U_\infty = 12$ m/s ($Re_H = HU_\infty/\nu = 41000$, $Re_\tau = 2600$). The boundary layer separates at the edge of the step and creates a recirculation region downstream of the step with a reattachment length (in absence of actuation) of $x_R = 0.226$ m ($x_R/H = 4.5$). The synthetic jet actuator is placed inside the step with its slotted orifice aligned along the edge of the step (i.e. the long-dimension (230 mm) in spanwise direction). The nozzle is placed at an angle of 45 degrees to both the horizontal and vertical face of the step. The two-component velocity field at the centreline plane of the jet (in streamwise–wall-normal direction) is measured using a set-up equal to the one described above for the flat plate used in Paper 4 (i.e. two aligned lasers, three 16MP cameras). The measured field-of-view is approximately 725 mm in streamwise direction and 100 mm in wall-normal direction. Velocity vectors are calculated using LaVision Davis with a window size of 24×24 pixels with 50% overlap between windows, resulting in a resolution of 0.7 mm per vector. Presented velocity fields (and derived quantities) are averaged over 480 instantaneous vector fields per phase for eight phases of the actuation cycle.

3.2.3 University of Melbourne wind tunnel

The high-Reynolds number boundary layer wind tunnel at the University of Melbourne is used for the measurements presented in Paper 3. This blowing-type open-return wind tunnel has a test-section length of 27 m with a span of 1.9 m and a height of 0.9 m. The unique feature of this world-leading facility is the development and growth of a turbulent boundary layer over the 27 m long test section, leading to a relatively large boundary layer thickness (up to $\delta \approx 0.4$ m). This enables measurements at high Reynolds numbers (Re_τ) while still having measurable (i.e. large enough) inner scales in the boundary layer.

The actuator is placed flush with and perpendicular to the surface, aligned with the long dimension (13 mm) in streamwise direction and the short dimension (1 mm) in spanwise direction. Two measurement locations are used in the tunnel: 8 m and 20 m downstream of the boundary-layer trip. A range of parameters is used with free-stream velocities of $U_\infty = 10$–25 m/s and boundary-layer thicknesses of $\delta = 132$–296 mm ($Re_\tau = 3200$–12800). Time-series of velocity magnitude are measured using hot-wire anemometry (HWA, hot-wire anemometry is discussed below) in the centreline plane of the jet at multiple streamwise and wall-normal locations downstream of the actuator. A

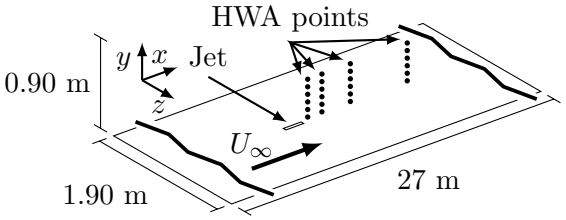

Figure 3.5: Schematic of the smooth-wall turbulent boundary layer set-up used in Paper 3 (taken from Berk et al. (2017a)) (not to scale).

schematic of the set-up and location of measurement points is presented in Figure 3.5. Measurements are performed using a single-wire traversing hot-wire probe of 0.5 mm length and 2.5 µm diameter (length-to-diameter ratio of 200). This wire is operated in constant-temperature mode using an in-house Melbourne University Constant Temperature Anemometer, set to an overheat ratio of 1.7. The frequency response of the wire is approximately 25 kHz and the wire is sampled at 50 kHz (25 kHz filtered).

3.3 Measurement techniques

The measurements presented in this thesis are all taken using either hot-wire anemometry or particle image velocimetry. Both techniques are widely used in experimental fluid mechanics. This section gives a general description of both techniques, focussing on aspects used in Part II of the thesis. Measurements using both techniques can be phase-locked to the actuator signal, which is also briefly discussed.

3.3.1 Hot-wire anemometry

Hot-wire anemometry (HWA) is used to characterize the output of the actuators in all papers, as well as for the main measurements in Paper 3. Hot-wire anemometry as applied in this thesis results in a one-dimensional one-component velocity measurement (i.e. velocity magnitude in a single point). The advantage of HWA is the high spatial and temporal resolution of the measurement compared to other techniques. A brief description of HWA is given here, a more detailed description can be found in Tropea (2007).

The operating principle of HWA is the convection of heat from a small (heated) wire. This wire is of a material that changes resistance with temperature such as tungsten (used throughout this study), enabling indirect measurement of the wire temperature through resistance. The conductive and convective heat transfers of the wire are coupled through the empirical relation known as King's law,

$$\frac{R_w I_w^2}{R_w - R_a} = A + BU^{0.50}, \tag{3.1}$$

where R_w and I_w are the measured resistance of and current through the wire, R_a is the wire resistance at the temperature of the working fluid, U is the velocity of the working fluid and A and B are constants. These constants A and B are known functions of the length, diameter and temperature coefficient of resistance of the wire, as well as the thermal conductivity and kinematic viscosity of the fluid.

In the present work constant-temperature hot-wire anemometry is used in which the temperature (and thus the resistance R_w) of the wire is kept constant during measurement. This resistance is specified through the overheat ratio,

$$a_w = \frac{R_w}{R_a}, \tag{3.2}$$

which determines the sensitivity of the wire. A higher ratio increases sensitivity, but using a too high wire temperature will damage the wire. Typical overheat ratios in air are in the range $a_w = 1.5$–2.0. Using this constant wire temperature, Equation 3.1 can be rewritten as

$$A_w^2 = A' + B' U^{0.50}, \tag{3.3}$$

where $A_w = R_w I_w$ is the voltage over the wire and A' and B' now also depend on the overheat ratio and the electric resistivity of the wire. Using this relation, the fluid velocity can be measured indirectly from the voltage over the wire, i.e. $U = U(A_w)$. During calibration, the voltage is measured for known fluid velocities, from which the constants A' and B' are determined. During the measurement, A_w is measured and U can be calculated from A_w, A' and B'. Both A' and B' depend on the fluid temperature and this temperature should be recorded during measurements to apply a temperature correction to the results.

Leading-order uncertainties in hot-wire measurements are in calibration error (partially addressed through careful calibration), temperature drift (partially accounted for through simultaneous measurement of the temperature) and electrical drift (partially accounted for through interpolation between pre- and post-calibration).

3.3.2 Particle image velocimetry

Papers 1, 2 and 4 use particle image velocimetry (PIV) as the main measurement technique. PIV as applied in this thesis results in two-dimensional two- or three-component velocity fields (i.e. two or three components of the velocity in a plane). The advantages of PIV are the large spatial domain compared to other measurement techniques and the simultaneous measurement of multiple velocity components. A brief description of PIV is provided here, a more detailed description can be found in Adrian and Westerweel (2011).

The operating principle of PIV is the estimation of the displacement of tracer particles between two instantaneous snapshots of the flow over a known time interval. These tracer

particles need to be small enough to accurately follow the flow, large enough to scatter light and neutrally buoyant in the working fluid. Typical tracer particles used in air are smoke particles as emitted by a smoke/fog machine or vegetable oil droplets. Assuming that the tracer particles do not interact with the flow, PIV can be considered to be a non-intrusive measurement technique. Tracer particles are typically illuminated in a plane (or volume in tomographic-PIV, not used in this thesis) using a pulsed laser. An image of the light scattered by these particles is formed on an image sensor (digital camera) using a lens. The location on the image plane (recorded by the camera) is related to the location in the object plane (the actual particle in the laser sheet) through calibration. Images are processed in pairs, where the displacement of the flow between the two images is estimated in specified interrogation windows. Each window contains the images of a number of particles that are assumed to move with the same velocity. The window from the first image is cross-correlated with an equal but displaced window in the second image. Each displacement will give a certain correlation value, leading to a map of correlation values as function of horizontal and vertical displacement. The highest peak in this correlation map is taken to be the true displacement of the interrogation window. The velocity at the centre of the interrogation window is then calculated by dividing this displacement by the known time step between the two images.

Leading order uncertainties in PIV are caused by calibration errors (partially addressed through careful calibration), pixel-locking (bias of measured particle-displacement to integer number of pixels, partially addressed through increasing resolution such that particle images are larger than one pixel) and out-of-plane motions (partially addressed by aligning laser-sheets with the flow where possible or by decreasing the time interval between image pairs).

Planar-PIV

A two-component two-dimensional technique is planar-PIV, in which a camera is positioned perpendicular to the illuminated plane. This means that the object plane and image plane are parallel and deformation between the planes is minimal. A calibration is applied by putting a calibration target at the exact location of the object plane. This target typically consists of a rectangular array of dots with known spacing between the dots. The PIV software relates the image of dots on the image plane to the specified array, compensating for optical deformations (caused by for example the lens but generally negligible in planar-PIV). The relation between pixels and known (physical) spacing between the dots also gives a magnification as pixels per millimetre.

Stereoscopic-PIV

A three-component two-dimensional (i.e. all three velocity components in a two-dimensional plane) technique is stereoscopic-PIV (or stereo-PIV). In stereo-PIV two cameras

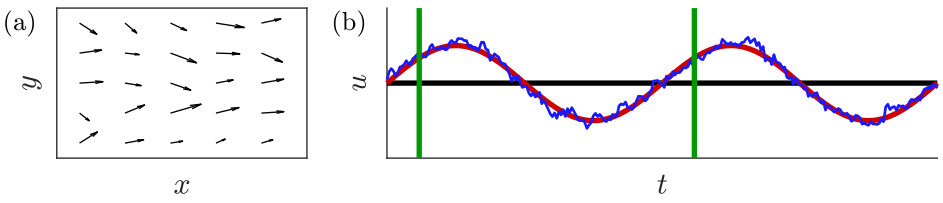

Figure 3.6: Schematic of phase-locking showing an instantaneous vector field (a) and decomposition of velocity signal of a single vector into mean (black), phase-locked (red) and instantaneous (blue) components (b).

are aimed at the illuminated plane on an angle from different locations. Using a non-perpendicular angle means that the object plane and image plane are not parallel and (without compensation) only a small part of the object plane will be in focus (as the focal plane is parallel to the image plane). This is accounted for by placing the lens at an angle compared to both the image plane and the object plane under the so-called Scheimpflug condition, ensuring that the focal plane is tilted such that it is aligned with the object plane. Another effect of the non-perpendicular angles is a perspective deformation of the image which enables measurement of motion in the out-of-plane direction, but also requires adequate calibration because of the non-constant magnification across the image. A calibration target is used that consists of two parallel planes with slightly different distance to the image plane such that the out-of-plane component can be calibrated along with the perspective deformation of the plane. Stereo-PIV software relates the image of the array of dots on each plane to the specified spacing, compensating for both optical and perspective deformation. The difference between the two planes as registered by the two cameras enables calibration of the out-of-plane component.

3.3.3 Phase-locking

Both hot-wire data and PIV data can be phase-locked to the (sinusoidal) actuator signal. The term phase locking here refers to taking a measurement at the same moment (phase) of the actuation cycle multiple times. For hot-wire measurements (where the acquisition rate is typically much higher than the jet frequency) this is done by simultaneously acquiring the hot-wire signal as well as the sinusoidal signal send to the actuator. During post-processing the measured data can then be grouped into bins corresponding to a given phase in the actuation sine wave. For PIV measurements (where the acquisition rate is typically much lower than the jet frequency), phase locking is prescribed by sending a trigger pulse to the measurement equipment at a specific phase of the actuation waveform.

A schematic of phase-locking is presented in Figure 3.6. Figure 3.6a represents an instantaneous two-component two-dimensional vector field as measured by planar-PIV. The actual velocity of the flow at the location of each of these vectors varies in time

as is presented by the blue line (corresponding to a single component of one vector) in Figure 3.6b. This velocity $u(t)$ can be decomposed as

$$u(t) = \langle u(t) \rangle + \langle u(\phi(t)) \rangle + u'(t), \tag{3.4}$$

where $\langle u(t) \rangle$ represents the time-averaged velocity, $\langle u(\phi(t)) \rangle$ represents the phase-averaged velocity at phase $\phi(t)$ and $u'(t)$ represents instantaneous velocity fluctuations. This is represented in Figure 3.6 by the black line, corresponding to $\langle u(t) \rangle$, the red line, corresponding to $\langle u(t) \rangle + \langle u(\phi(t)) \rangle$ and the blue line, corresponding to $\langle u(t) \rangle + \langle u(\phi(t)) \rangle + u'(t)$. The vertical green lines represent either the phase-locked position at which measurements are taken in PIV or the phase-locked bin over which data is averaged in HWA. Phase-averaging results in the instantaneous velocity fluctuations being cancelled out, i.e. leading to the periodic signal indicated by the red line. Subsequently averaging over all phases gives a time average, indicated by the black line.

4. Conclusions and Contributions

Part II of this thesis consists of two published journal papers, one journal paper submitted for review and one manuscript under preparation for submission to a journal. This chapter lists the four papers with their citation, short abstract, main conclusions and the contributions of each author.

Paper 1

Berk, T., Gomit, G., and Ganapathisubramani, B. (2016). Vectoring of parallel synthetic jets: a parametric study. *J. Fluid Mech.*, 804:467–489.

This study investigates the interaction between a pair of parallel synthetic jets. When operated with a phase-difference between their actuation cycles, the resulting direction of the jets can be altered which is called vectoring. This phenomenon can be described using five dimensionless parameters: the aspect ratio, Strouhal number, Reynolds number, spacing and phase difference. This study presents an experimental parametric study of the latter four, while using a fixed aspect ratio that is large enough to assume two-dimensional flow.

The parametric study shows a range of behaviour of the resultant jet. This resultant jet can be bifurcated or merged with differences in the included angles, vectoring angles and momentum fluxes. A physical mechanism – explaining the observed behaviour – is proposed based on vortex trajectories. The results obtained in this study increase the level of control over a pair of synthetic jets.

The actuator used in this study has been designed by G. Gomit. The experiments have mainly been performed by me, T. Berk, with help for some initial cases provided by G. Gomit. Processing of the raw data into vector fields, analysis of the vector fields and writing of the paper has been done by me, T. Berk. Supervision and remarks on the paper have been given by B. Ganapathisubramani.

Paper 2

Berk, T., Medjnoun, T., and Ganapathisubramani, B. (2017). Entrainment effects in periodic forcing of the flow over a backward-facing step. *Phys. Rev. Fluids*, 2:074605.

This study investigates the effect of periodic forcing of the flow over a backward-facing step using synthetic jets. The effect of the Strouhal number on the reattachment length of the separated flow behind the step is studied experimentally for four different Strouhal numbers.

The synthetic jet forms a train of alternating vortices that entrains momentum into the recirculation region. This momentum entrainment is shown to be the driving force for a decrease in reattachment length. Variations of the formation length, size and strength of the vortices with Strouhal number are observed. Based on these findings a physical mechanism is proposed which explains the known relation between reattachment length and Strouhal number. The results obtained in this study increase the physical understanding of the relation between the actuation frequency and reattachment length of a separated flow. This physical understanding increases the level of control over the reattachment length.

The experimental set-up used in this study has been designed by T. Medjnoun. The experiments have been performed by T. Medjnoun. Processing of the raw data into vector fields has been done by T. Medjnoun. Analysis of the vector fields and writing of the paper has been done by me, T. Berk, without involvement of T. Medjnoun. Supervision and remarks on the paper have been given by B. Ganapathisubramani.

Paper 3

Berk, T., Hutchins, N., Marusic, I., and Ganapathisubramani B. Trajectory of a synthetic jet issuing into high Reynolds number turbulent boundary layers.
Under review for publication in the Journal of Fluid Mechanics.

This study investigates the trajectory of a synthetic jet issuing into a high Reynolds number turbulent boundary layer. This problem can be described by the geometry, frequency and velocity of the jet as well as the free stream velocity, boundary-layer thickness, friction velocity and viscosity of the cross flow.

It is shown that the trajectory scales with the velocity ratio (between jet and cross flow), the friction Reynolds number and a non-dimensional jet frequency. The scaling with velocity ratio is equal to the scaling for a steady jet in cross flow. The Reynolds-number scaling indicates a negligible influence of the Reynolds number. The relevant non-dimensional frequency is shown to be the ratio between the separation of subsequent pulses created by the jet and the size of these pulses. It is argued that in the limit where this ratio geometrically represents a steady jet, the scaling for a steady jet is recovered,

showing analogy between the trajectory of a steady jet in cross flow and pulsed or synthetic jets in cross flow. The results obtained in this study indicate the effect of cross-flow and actuation parameters on the trajectory of a synthetic jet in a turbulent boundary layer. These results increase the control over the trajectory of a synthetic jet in a given cross flow.

The same actuator as in Berk et al. (2016) (Paper 1) is used. The experiments have been performed by me, T. Berk. Processing of the raw data, analysis of the data and writing the paper have been done by me, T. Berk. Support in the form of the use of facilities has been provided by N. Hutchins and I. Marusic. Supervision and remarks on the paper have been given by B. Ganapathisubramani, I. Marusic and N. Hutchins.

Paper 4

Berk, T., and Ganapathisubramani, B. Effects of vortex-induced velocity on the wake of a synthetic jet issuing into a turbulent boundary layer.
Manuscript under preparation.

This study investigates the effects of vortex-induced velocity on the wake of a synthetic jet issuing into a turbulent boundary layer. The interaction between a synthetic jet and a turbulent boundary layer leads to the formation of a train of vortical structures. These vortical structures cause a momentum deficit in the cross flow.

It is shown that part of this momentum deficit is caused by the velocity induced by the vortical structures. This induced velocity is reconstructed by measuring the geometry and strength of these structures and applying Biot-Savart law. An inviscid-flow model is developed which predicts the evolution of a train of input structures. The reconstructed velocity field as well as the velocity field predicted by the inviscid model is qualitatively similar to measured velocity fields. This study presents evidence that the velocity induced by the vortical structures created by a synthetic jet play an important role in the evolution of the jet and the velocity field and momentum deficit around the jet. The results obtained in this study increase the physical understanding of the sources of momentum deficit of a synthetic jet in a turbulent boundary layer. This physical understanding can be used to develop strategies to minimize this momentum deficit, potentially increasing the efficiency of flow-control applications.

The same actuator as in Berk et al. (2016) (Paper 1) is used. The experiments have mainly been performed by me, T. Berk, with help for some of the cases provided by a postdoctoral research assistant, Guillaume Gomit (planar-PIV measurements) and for some of the cases by a PhD student, Girish Jankee (stereo-PIV measurements). Processing of the raw data into vector fields and analysis of these vector fields have been done by me, T. Berk. The inviscid-flow model has been developed by me, T. Berk. The paper has been written by me, T. Berk. Supervision and remarks on the paper have been given by B. Ganapathisubramani.

Parts of this work have been published as:

Berk, T., Gomit, G., and Ganapathisubramani, B. (2017). Effects of vortex-induced velocity on the wake of a synthetic jet issuing into a turbulent boundary layer. *10th International Symposium on Turbulence and Shear Flow Phenomena*, Chicago, IL, USA.

Berk, T., Gomit, G., and Ganapathisubramani, B. (2017). Effects of vortex-induced velocity on the streamwise evolution of synthetic jets in cross-flow. *55th AIAA Aerospace Sciences Meeting*, Grapevine, TX, USA. AIAA 2017-0325.

Part II

Papers

Paper 1

Vectoring of parallel synthetic jets: a parametric study

Tim Berk, Guillaume Gomit and Bharathram Ganapathisubramani

Aerodynamics and Flight Mechanics Research Group, University of Southampton, Southampton SO17 1BJ, UK

J. Fluid Mech., **804**:467–489, 2016.

The vectoring of a pair of parallel synthetic jets can be described using five dimensionless parameters: the aspect ratio of the slots, the Strouhal number, the Reynolds number, the phase difference between the jets and the spacing between the slots. In the present study, the influence of the latter four on the vectoring behaviour of the jets is examined experimentally, using particle image velocimetry. Time-averaged velocity maps are used to give a qualitative description of the variations in vectoring for a parametric sweep of each of the four parameters independently. A diverse set of vectoring behaviour is observed in which the resulting jet can be merged or bifurcated and either vectored towards the actuator leading in phase or the actuator lagging in phase. Three performance metrics are defined to give a quantitative description of the vectoring behaviour: the included angle between bifurcated branches, the vectoring angle of the total flow and the normalized momentum flux of the flow. Using these metrics, the influence of changes in the Strouhal number, Reynolds number, phase difference and spacing are quantified. Phase-locked maps of the swirling strength are used to track vortex pairs. Vortex trajectories are used to define three Strouhal number regimes for the vectoring behaviour. In the first regime, vectoring behaviour is dominated by the pinch-off time, which is written as function of Strouhal number only. In the second regime, the pinch-off time is invariant and the vectoring behaviour slightly changes with Strouhal number. In the third regime, given by the formation criterion, no synthetic jet is formed. Vortex positions at a single phase, shortly after creation of the lagging vortex pair, are used to propose a vectoring mechanism. This vectoring mechanism explains the observed qualitative and quantitative variations for all four parameters.

1 Introduction

In the last two decades, synthetic jets have attracted a considerable amount of research (e.g. Smith and Glezer (1998); Glezer and Amitay (2002); Cattafesta and Sheplak (2011); O'Farrell and Dabiri (2014)). Both experimental and numerical studies have focussed on the development of actuators, the formation and evolution of synthetic jets and on flow control applications. A typical synthetic jet actuator (SJA) consists of a cavity bounded by a diaphragm and an orifice. An oscillatory motion of the diaphragm

drives a time-periodic flow through the orifice. Synthetic jets have the unique feature that they consist entirely of the working fluid of the flow system in which they are deployed. This creates a zero-net-mass-flux flow that has non-zero streamwise momentum. A large operational difference between continuous and synthetic jets is that the latter do not need an external fluid supply and therefore can be easily integrated in complex geometries, making them attractive actuators for flow control. Applications of synthetic jets, such as separation control (Dandois et al., 2007), turbulent boundary layer control (Rathnasingham and Breuer, 2003; Canton et al., 2016), virtual aeroshaping (Mittal and Rampunggoon, 2002), thrust vectoring (Smith and Glezer, 2002; Luo and Xia, 2005), heat transfer (Persoons et al., 2009) or propulsion (Athanassiadis and Hart, 2016), include, but are not limited to, applications with a crossflow. For most of these applications, the specific direction of the synthetic jet is important. For example, consider the control of large-scale structures in turbulent wall-bounded flows as introduced by Schoppa and Hussain (1998) and re-analysed by Canton et al. (2016). This control depends on direct interactions between these large-scale structures and controlled vortices. Steering of vortices using vectoring of a synthetic jet enables the precise targeting of these structures. Another example is propulsion using pulsed jets as investigated by Athanassiadis and Hart (2016). Vectoring these jets would vector the resultant thrust and add a steering mechanism to this method of propulsion.

As outlined below, in this study two parallel synthetic jets are placed side-by-side in quiescent air. Previous studies have looked at circular in-line twin synthetic jets issuing in a laminar boundary layer crossflow, see for example Wen et al. (2015). In practical applications, such as turbulent boundary layer control or separation control, it is often desirable to cover a large spanwise length, making rectangular jets more suitable than their circular equivalents. In order to perform detailed measurements of the fundamental vectoring mechanisms – not overshadowed by a crossflow – measurements are performed in quiescent air. This is not only useful for applications in absence of a crossflow (such as thrust vectoring), but will also give valuable insight into the effect of different parameters on the vectoring behaviour, which may be applied in subsequent crossflow studies.

Disregarding the internal flow and dimensions of the actuator, the geometry for rectangular orifice jets is described by the slot length, l (m), and width, d (m). A single synthetic jet is actuated by a sinusoidal signal with frequency f (Hz) and amplitude A (V_{pp}). It is assumed that this leads to a sinusoidal jet centreline velocity, u (m/s), given by

$$u(t) = u_{max} \sin\left(2\pi t f + \theta\right), \tag{1}$$

with u_{max} (m/s) the maximum velocity and θ (deg) the phase of the jet. The start of a velocity cycle is defined as the onset of blowing. Following Smith and Glezer (1998), the mean blowing velocity, $\bar{u}$ (m/s), is used as a representative velocity, defined as

$$\bar{u} = \frac{1}{T}\int_0^{T/2} u(t)\mathrm{d}t = \frac{1}{T}\int_0^{T/2} u_{max}\sin\left(2\pi t/T\right)\mathrm{d}t = \frac{u_{max}}{\pi}, \tag{2}$$

with $T = 1/f$ (s) the period of the signal. It should be noted that other representative velocities are used throughout the literature, most notably the momentum flow velocity, U_0 (m/s), as defined by Cater and Soria (2002), which relates to the mean blowing velocity as $U_0 = \bar{u}\pi/\sqrt{2}$.

The flow of a single synthetic jet can be characterized using three dimensionless parameters (Glezer and Amitay, 2002): the aspect ratio, the Strouhal number and the Reynolds number, defined as

$$AR = \frac{l}{d}, \tag{3}$$

$$St = \frac{fd}{\bar{u}}, \tag{4}$$

$$Re = \frac{\bar{u}d}{\nu}, \tag{5}$$

with ν (m^2/s) the kinematic viscosity.

In the limit of infinite aspect ratio, the flow can be assumed two-dimensional. For finite aspect ratio jets, edge effects and three-dimensional jet development play a role. However, results obtained by Van Buren et al. (2014a) for aspect ratios of $AR = 6$–18, indicate that edge effects do not reach the central plane up to a distance of approximately $y/d < AR/2$. In the present research a near-field up to this distance is defined within which three-dimensional effects on the flow in the central plane are assumed negligible.

Holman et al. (2005) proposed and validated a formation criterion for synthetic jets. They demonstrated that for $St > 1/\pi$ vortices do not travel far enough from the actuator and are ingested back into the orifice during the suction phase. Therefore, to create a synthetic jet, it is important to keep the Strouhal number below $St = 1/\pi$.

When two actuators are placed next to each other at a spacing Δ (m), as presented schematically in Figure 1, vectoring of the jets can be achieved by applying a phase difference θ (deg) between the driving signals (Smith and Glezer, 2005). This expands the number of dimensionless parameters to five, since the phase difference (θ) and dimensionless spacing between the actuators (Δ/d) also become important alongside the above-mentioned three parameters.

A very limited body of literature exists on the influence of these five parameters on the vectoring of parallel synthetic jets. Smith and Glezer (2005) investigated experimentally the vectoring of parallel synthetic jets by varying the phase difference for a single aspect ratio ($AR = 150$), Strouhal number ($St = 0.03$), Reynolds number ($Re = 311$) and

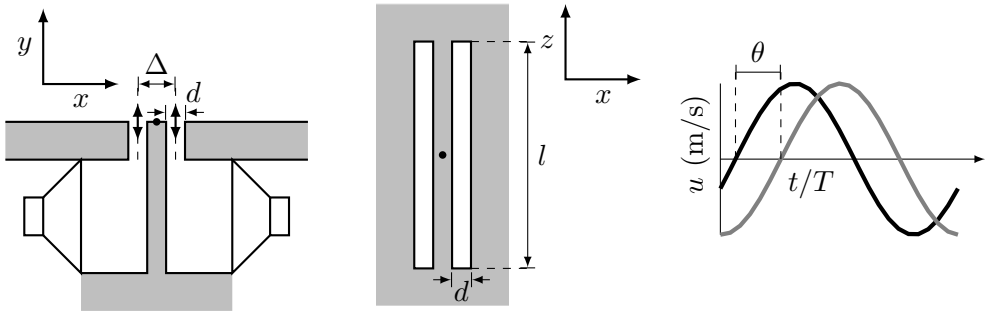

(a) Side view (b) Top view (c) Velocity cycles

Figure 1: Schematic of synthetic jet actuator set-up, orientation and velocity cycle. The dots in (a) and (b) indicate the origin of the coordinate system.

spacing ($\Delta/d = 3.3$). The authors demonstrated that in the absence of a phase difference a merged synthetic jet is formed with the same centreline velocity as a single jet, but more than twice the entrained fluid. When a phase difference is introduced between the driving signals, the combined jet is vectored towards the actuator leading in phase. The vectoring angle increases with the phase difference, until the jet is fully attached to the surface. Vortex trajectories were tracked using phase-averaged vorticity concentrations. The authors demonstrated that the vortex trajectories are influenced by the velocity field in the vicinity of the actuators.

Luo and Xia (2008) carried out similar experiments, varying the phase difference for a single aspect ratio, Strouhal number, Reynolds number and spacing ($\Delta/d = 3.5$, slot length and jet velocity not mentioned). They showed that the merged jet vectors towards the actuator leading in phase, in agreement with the findings of Smith and Glezer (2005). The authors proposed an interaction mechanism, presented in Figure 2, explaining the enhancing and vectoring mechanisms of the interacting synthetic jets, based on vortex trajectories. In absence of a phase difference (see Figure 2a), two closely symmetric vortex pairs L^+L^- and R^+R^- are formed at the orifice exits. The lower pressure accompanying the vortex pairs makes them attract each other which leads to a merged vortex pair, M^+M^-. When the actuator on the right is leading in phase (see Figure 2b), R^+R^- is leading L^+L^-. The trailing vortex pair is attracted by the low pressure in the wake of the leading vortex pair. The leading vortex pair slows down due to friction and entrainment of surrounding fluid, causing the trailing vortex pair to impinge upon the leading vortex pair. This transfers momentum in the direction towards the leading vortex pair, resulting in a merged jet in the direction of the actuator leading in phase.

The present research will expand the analyses by Smith and Glezer (2005) and Luo and Xia (2008) by investigating experimentally the influence of the Strouhal number, Reynolds number, phase difference and spacing on the vectoring of parallel synthetic jets. This increases the number of investigated parameters from one (phase difference) to four, only leaving the aspect ratio out of consideration. The fixed aspect ratio will

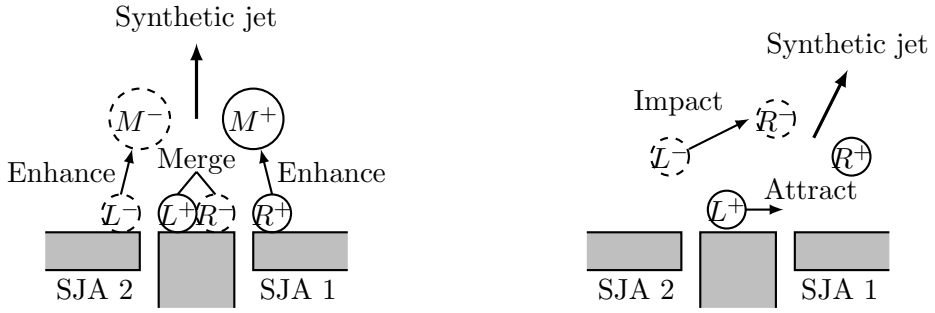

(a) Enhancing mechanism (b) Vectoring mechanism

Figure 2: Interaction between synthetic jets, redrawn from Luo and Xia (2008). Synthetic jets in absence of a phase difference, leading to an enhanced merged jet (a) and synthetic jets with a phase difference, leading to a vectored jet (b).

be chosen large enough to enable the assumption that three-dimensional effects on the vectoring behaviour are negligible.

Results from both qualitative and quantitative analyses are presented. The qualitative analysis will first show the variation of time-averaged flow fields with Strouhal number for a fixed Reynolds number, phase difference and spacing. This is followed by a discussion on the influence of Strouhal number, identifying the exact mechanisms – using vortex tracking – that cause two distinct regimes of vectoring behaviour in Strouhal number space. Next, time-averaged flow fields for varying Reynolds number with a fixed phase difference and spacing are presented to show the (lack of) influence of the Reynolds number on the vectoring of parallel synthetic jets. The parametric variation is completed by varying the phase difference and spacing for a fixed Strouhal number and Reynolds number. For the quantitative analysis, parameters related to the direction and strength of the jet are defined. A quantitative analysis is performed on the same variations as the qualitative analysis (i.e. covering parametric variations of the Strouhal number, Reynolds number, phase difference and spacing). Using these results a new vectoring mechanism is proposed, explaining the vectoring behaviour for the full parameter space.

2 Experimental set-up and procedures

2.1 Description of the synthetic jet actuator

A Visaton SC 8 N speaker is used to actuate the synthetic jet actuator. This speaker has an impedance of 8 Ω with a rated power of 30 W (corresponding to $A = 15.5$ V_{pp}) and a frequency response between 70–20000 Hz. Therefore, the synthetic jet actuator is operated with an amplitude limit of $A = 15$ V_{pp} and a lower frequency limit of $f = 100$ Hz. The average blowing velocity of the synthetic jet actuator is measured for multiple amplitudes and frequencies. All achievable values are represented by the shaded area in the graph of the Reynolds number versus the Strouhal number in Figure 3. The

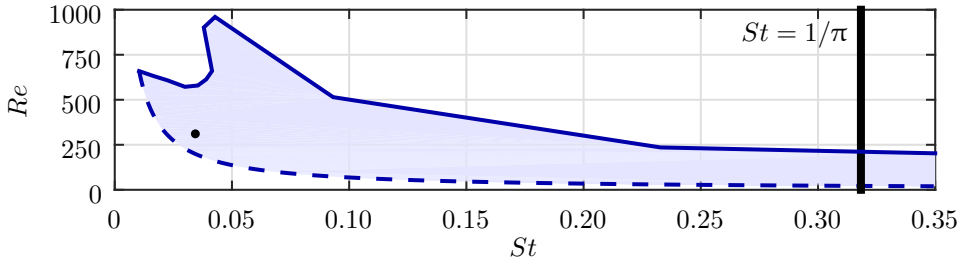

Figure 3: Actuator response in terms of Strouhal and Reynolds numbers for the actuator used in the present research. The shaded area shows the achievable values for the actuator, limited by the maximum amplitude of $A = 15$ V_{pp} and the minimum frequency of $f = 100$ Hz, indicated by the solid and dashed lines respectively. The formation criterion is indicated by the thick solid line. The black dot indicates the operating conditions in Smith and Glezer (2005).

upper amplitude limit of $A = 15$ V_{pp} shows a clear peak, corresponding to the Helmholtz resonance frequency of the actuator around $f = 600$ Hz.

The Strouhal number corresponding to the formation criterion is indicated by the thick solid line. The operating conditions for Smith and Glezer (2005) ($Re = 311$, $St = 0.03$) are indicated by the black dot.

Two identical synthetic jet actuators are placed side by side, parallel along the length of their orifices, as presented in Figure 1. The slot width is $d = 1$ mm and the slot length is $l = 13$ mm, resulting in an aspect ratio of $AR = 13$. The spacing can be varied between $\Delta = 2.0$–3.0 mm, measured from the centres, resulting in dimensionless spacings of $\Delta/d = 2.0$–3.0. The actuators are milled from aluminium plates with 3D printed nozzles. The accuracy of the 3D printing technique is 0.1 mm, leading to an estimated uncertainty in the spacing of $\epsilon_{\Delta/d} = 0.1$. The actuators are flush mounted in a horizontal plate, with the slot exits perpendicular to the plate. The actuators have a volume of 1.85×10^{-5} m^3 and a neck length of 19.5 mm.

2.2 Measurement procedures

Measurements are performed using two-dimensional, two-component particle image velocimetry (PIV). Figure 4 presents a schematic of the experimental set-up. The PIV system consists of a Litron 200 mJ dual-pulse Nd-YAG laser and a LaVision Imager Pro LX 16MP camera that are phase-locked to the driving signal using a National Instruments NI-DAQ. The laser sheet is positioned along the small symmetry axis of the slots, at $z/d = 0$ as defined in Figure 1b. Seeding is provided by a Martín Magnum 1200 smoke machine, ejecting smoke particles with a mean diameter of 1 µm into a purpose-build perspex box of length $400d$ on each side. Images are captured and processed using LaVision DaVis 8.2.2. Vectors are determined using a first step with a window size of 64×64 pixels, followed by two steps of 32×32 pixels with 50% overlap, resulting in a resolution

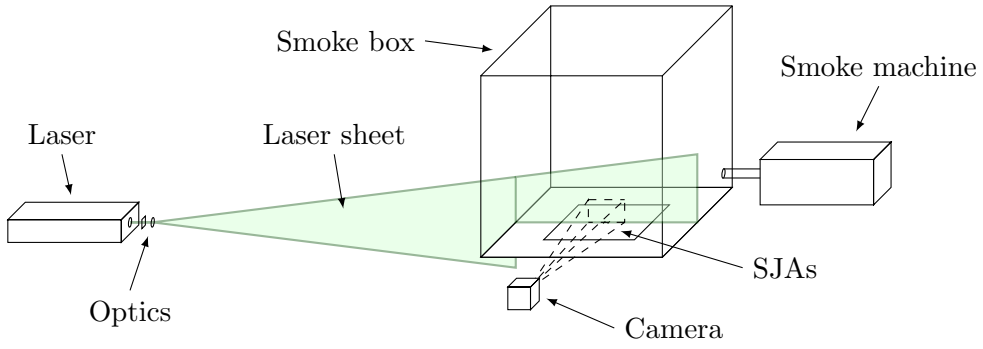

Figure 4: Schematic of experimental set-up. Synthetic jet actuators are located underneath the bottom plate of the smoke box.

of one vector per 0.16 mm. The uncertainty in PIV is on the order of 0.05 pixels (Sciacchitano et al., 2015), which corresponds to an uncertainty in the instantaneous velocity fields of $\epsilon_{u_i} = 0.1$ m/s for the current work. For the phase-averaged, as well as for the time-averaged data, 100 image pairs are acquired, resulting in averages over 100 vector fields. This ensemble of 100 vector fields leads to an uncertainty in the repeatability of the same order as the uncertainty in the instantaneous velocity fields, showing adequate convergence for the analyses performed in the present research.

Phase-averaged flow fields are post-processed into swirling strength concentrations using MATLAB. Swirling strength is used to identify vortices and is defined as the imaginary part of the complex conjugate eigenvalues of the two-dimensional velocity gradient tensor as in Adrian et al. (2000). Vortices are identified as regions where the swirling strength exceeds a manually selected threshold. The advantage of using swirling strength over vorticity is that the former only identifies vortices, while the latter also depicts shear layers.

The synthetic jet velocity is determined using hot-wire anemometry. The estimated uncertainty in Strouhal number scales with $St/\bar{u}$ and ranges from $\epsilon_{St} = 4 \times 10^{-4}$–$18 \times 10^{-4}$. A repeatability study on the hot-wire data showed that the phase difference can be determined with an estimated uncertainty of $\epsilon_\theta = 2$ deg.

3 Results and discussion

The results and discussion are divided into two sections that contain qualitative and a quantitative analyses, respectively. Both analyses start with a variation of Strouhal number for a fixed Reynolds number, phase difference and spacing. This is followed by a variation of Reynolds number for a fixed phase difference and spacing. The analyses are completed with the variation of phase difference and spacing for a fixed Strouhal number and Reynolds number. Both the qualitative and quantitative results are used to propose a new vectoring mechanism, amending and expanding the mechanism by

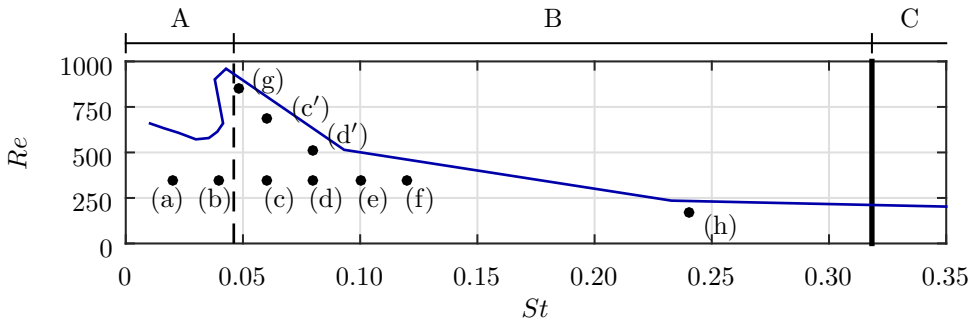

Figure 5: Parameters for each case with the actuator response for $A = 15$ V_{pp} shown as a reference. For each case $\Delta/d = 2.0$ and $\theta = 150°$ with the actuator on the right leading in phase.

Luo and Xia (2005), explaining vectoring of parallel synthetic jets for the full four-dimensional parameter space.

3.1 Qualitative analysis

Parametric variations are performed as described above. For the qualitative analysis, normalized time-averaged velocity maps of the local velocity magnitude ($|u|/\bar{u}$) in the central plane ($z/d = 0$) are presented. Vector fields, indicating the local direction of the velocity are overlaid on these velocity magnitude maps. For clarity, only one in twenty vectors is displayed. The vectoring direction and direction of individual branches as defined in Section 3.2 are indicated in the velocity maps by the solid and dashed blue lines respectively. Throughout the paper, phase differences are defined with the jet on the right leading in phase.

3.1.1 Dependency of vectoring behaviour on Strouhal number

The Strouhal number is varied for a fixed Reynolds number ($Re = 342$), phase difference ($\theta = 150$ deg, jet on the right leading in phase) and spacing ($\Delta/d = 2.0$). Normalized time-averaged velocity maps showing the vectoring behaviour for this variation are presented in Figure 6. The cases, (a)–(f), corresponding to Figure 6a–f, are indicated in the St–Re parameter space presented in Figure 5. The annotations in this parameter space will be explained below.

In cases (a) and (b), presented in Figures 6a and 6b, a bifurcated synthetic jet is produced with one branch in the vertical direction and one branch in the direction towards the actuator that is lagging is phase. For higher Strouhal numbers, presented in Figures 6c–f, the jet is bifurcated into a strong branch in the vertical direction and a weaker branch in the direction towards the actuator leading in phase. For these cases (c)–(f), the included angle between the two branches of the jet visually decreases for increasing

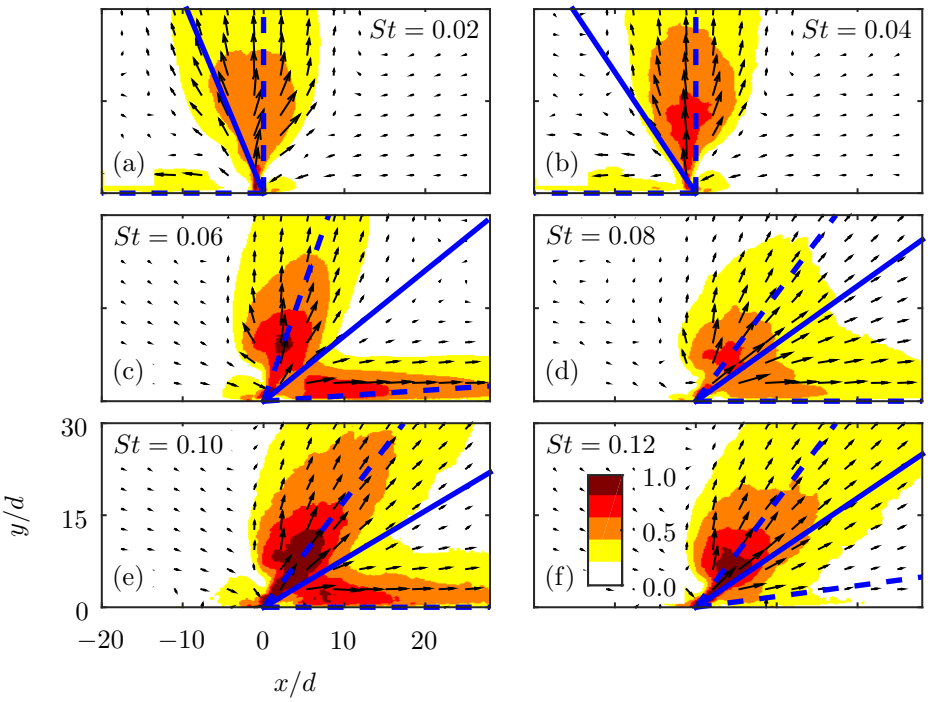

Figure 6: Normalized time-averaged velocity maps, $|u|/\bar{u}$, showing vectoring behaviour for different Strouhal numbers. For each case, $Re = 342$, $\Delta/d = 2.0$ and $\theta = 150°$ with the actuator on the right leading in phase. The solid and dashed blue lines indicate the vectoring direction and directions of the individual branches as defined in Section 3.2. For clarity, only one in twenty vectors is displayed. Cases are indicated in the graph in Figure 5.

Strouhal number. This variation of included angle with Strouhal number is quantified in Section 3.2.1.

Following the vectoring mechanism based on vortices as proposed by Luo and Xia (2005), vortices for cases (a) and (c) are tracked to identify the mechanism causing the difference in vectoring direction of the horizontal branch. Vortices are tracked using phase-locked maps of the swirling strength. Instantaneous flow fields are captured phase-locked to the driving signal at 12 equally spaced time-intervals. Some vortices can be tracked over more than a single cycle, leading to vortex trajectories consisting of more than 12 points. Others break up within a single cycle, leading to trajectories consisting of less than 12 points. The resulting vortex trajectories are presented in Figure 7. Vortex trajectories are numbered 1–4, according to the vortex starting positions from left to right in Figure 7, i.e. the anticlockwise and clockwise vortices originating from the lagging actuator are labelled 1 and 2 respectively and the anticlockwise and clockwise vortices originating from the leading actuator 3 and 4.

Figure 7 shows that the main difference between the $St = 0.02$ and the $St = 0.06$ cases is that different vortices are ingested into the neighbouring actuators. For the $St = 0.02$ case, the anticlockwise vortex originating from the leading actuator, numbered 3, is

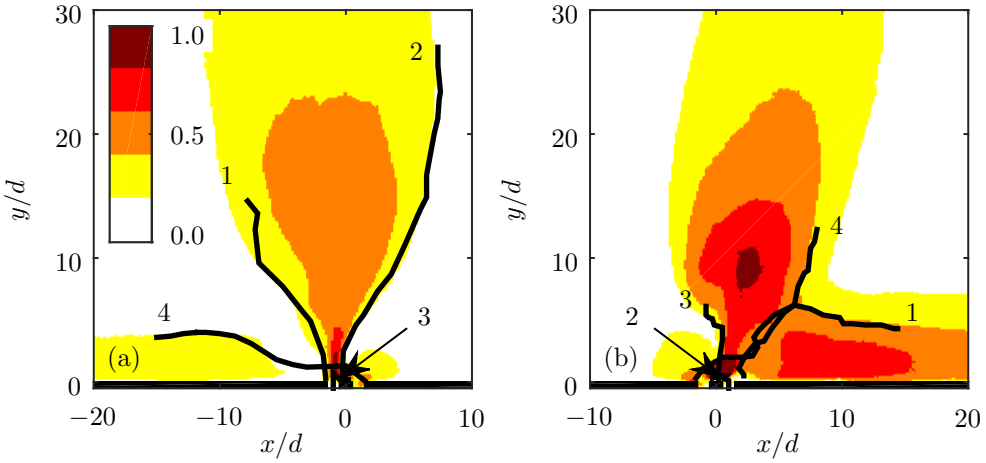

Figure 7: Normalized time-averaged velocity maps, $|u|/\bar{u}$, showing vortex trajectories for the $St = 0.02$ (a) and $St = 0.06$ (b) cases as shown in Figure 6a and c. Trajectories are numbered 1–4 for vortices originating from left to right, i.e. the anticlockwise (1) and clockwise (2) vortices originating from the lagging actuator and the anticlockwise (3) and clockwise (4) vortices from the leading actuator.

ingested into the lagging actuator, while for the $St = 0.06$ case the clockwise vortex originating from the lagging actuator, numbered 2, is ingested into the leading actuator. Upon ingestion of one of the vortices, the remaining vortex pair propagates in the vertical direction driven by its induced velocity, while the single vortex propagates along the surface driven by its own induced velocity reflected on the surface.

The relative position of the vortex trajectories on the velocity magnitude maps clearly indicates that the direction of both branches is governed by the vortex trajectories, as suggested in the literature by both Smith and Glezer (2005) and Luo and Xia (2008). It should be noted that both Figures 7a and 7b show that the direction of the vortex trajectories is determined within roughly $r/d = 5$, with r (m) being the absolute distance of the vortex from the origin. This is within the near-field range of $r/d < AR/2$ as determined by Van Buren et al. (2014a) where the behaviour of the jet can be considered to be two-dimensional (at least in the central plane).

The only difference between these two cases is the Strouhal number and, therefore, they have the exact same (normalized) velocity cycles, as presented in Figure 8. This implies that the only difference in velocity induced on newly created vortices by the suction of the neighbouring actuator is caused by the moment in the velocity cycle at which the vortex pairs are formed, which is defined as the pinch-off moment, t^*/T.

Gharib et al. (1998) proposed a constant formation number at which pinch-off occurs, $L/D \approx 4$, where L (m) is the stroke length and D (m) is the diameter of the circular orifice. They assumed the physical process causing this constant formation number to be a maximum in total circulation attainable in the vortex ring. A numerical study

by Rosenfeld et al. (1998) demonstrates the invariance of this formation number to differences in the velocity programme and Reynolds number.

A study by O'Farrell and Dabiri (2014) demonstrates that for non-axisymmetric orifices the formation number still holds when expressed as L/D_{eq}, where D_{eq} (m) is the equivalent diameter of the orifice; the diameter of an axisymmetric orifice with the same cross-sectional area. For a rectangular orifice, the equivalent diameter is given by

$$D_{eq} = 2\sqrt{ld/\pi} = 2d\sqrt{AR/\pi}. \tag{6}$$

The instantaneous stroke length, $L(t)$ (m), is given by

$$L(t) = \int_0^t u(t)\mathrm{d}t = \int_0^t u_{max}\sin\left(2\pi t/T\right)\mathrm{d}t = \frac{\bar{u}}{2f}\left(1-\cos\left(2\pi t/T\right)\right). \tag{7}$$

Dividing the instantaneous stroke length by the equivalent diameter leads to

$$L(t)/D_{eq} = \frac{\bar{u}}{fd}\frac{1-\cos\left(2\pi t/T\right)}{4\sqrt{AR/\pi}} = \frac{1}{St}\frac{1-\cos\left(2\pi t/T\right)}{4\sqrt{AR/\pi}}. \tag{8}$$

For distinction between instantaneous values and limiting parameters, in the remainder of this paper the formation number (L/D_{eq}) and pinch-off time (t^*/T) are denoted as L' and t' respectively. According to Equation 8, the pinch-off time, t', at which the constant formation number, L', is reached, is given by

$$t' = \cos^{-1}\left(1-4L'St\sqrt{AR/\pi}\right)/(2\pi). \tag{9}$$

Equation 9 shows that, for a given geometry and constant formation number, the pinch-off time is a function of the Strouhal number only. This, for the first time, shows the direct link between pinch-off and Strouhal number/aspect ratio.

In addition to the formation number, Aydemir et al. (2012) proposed a limiting time-scale at which pinch-off occurs. Using sinusoidal forcing of a steady round jet, they found a limiting time of $t' = 1/3$ at which the vortex rings pinch off if the formation number is not reached before then. The authors attributed this limiting time to the change in sign of the jet acceleration, occurring at $t/T = 0.25$ for a sinusoidal excitation.

It is assumed that the conditions in the present study are sufficiently similar to the literature and pinch-off happens at either $L' = 4$ or $t' = 1/3$, whichever occurs first. The boundary between these two regimes can be calculated from Equation 9 as the Strouhal number for which the right-hand side equals $t' = 1/3$. This Strouhal number is given by

$$St = \frac{1-\cos\left(2\pi/3\right)}{4L'\sqrt{AR/\pi}} = \frac{3}{32}\sqrt{\frac{\pi}{AR}}. \tag{10}$$

Accordingly, the pinch-off time is given by

$$t' = \cos^{-1}\left(1 - 16St\sqrt{AR/\pi}\right)/(2\pi) \qquad \text{for} \quad St < \frac{3}{32}\sqrt{\frac{\pi}{AR}}, \tag{11}$$

$$t' = 1/3 \qquad \text{for} \quad St > \frac{3}{32}\sqrt{\frac{\pi}{AR}}. \tag{12}$$

It should be noted that pinch-off is not qualitatively visible in the velocity field, nor in the vorticity field. As described by Gharib et al. (1998), the pinch-off time is found by relating the circulation in a given vortex to the time at which this total circulation was produced by the jet.

Pinch-off times for both cases presented in Figure 7 are calculated based on the above equations. For the $St = 0.02$ and $St = 0.06$ cases, pinch-off times are $t' = 0.19$ and $t' = 0.33$ respectively. The velocity cycles of both jets, with indicated pinch-off moments, are presented in Figure 8. Figure 8a demonstrates that for $St = 0.02$, corresponding to the case in Figure 7a, the vortex pair originating from the actuator leading in phase pinches off while the actuator lagging in phase is near the peak of its suction cycle. This causes the leading vortex pair to be partly ingested into the lagging actuator and the resulting branch of the synthetic jet to be vectored in the direction towards the actuator lagging in phase as in Figure 7a. In contrast, Figure 8b shows that for $St = 0.06$, corresponding to the case in Figure 7b, the vortex pair produced by the actuator lagging in phase pinches off while the actuator leading in phase is near the peak of its suction cycle. This causes the lagging vortex pair to be partially ingested into the leading actuator, forming a horizontal branch in the direction towards the actuator leading in phase, as in Figure 7b.

Equations 11 and 12 show that there is a limit for the Strouhal number, only depending on the aspect ratio, above which the pinch-off time is invariant. This limit, for the setup in the present study, is indicated by the dashed line in Figure 5. The range of Strouhal numbers below this limit, denoted as regime A, leads to a vectoring behaviour as presented in Figure 6a,b, for which a strong vertical branch and weak horizontal branch in the direction of the actuator lagging in phase are formed. The range of Strouhal numbers from this limit up to the formation criterion, denoted as regime B, leads to the vectoring behaviour presented in Figure 6c–f, for which a roughly vertical branch and a horizontal branch in the direction of the actuator leading in phase are formed. Above the formation criterion, in regime C, no synthetic jet is created. For the remainder of this paper, parameter variations within regime B only are considered.

It should be noted that the operating condition for Smith and Glezer (2005) lies between cases (a) and (b) in Figure 5. However, for their geometry the formation number, separating regimes A and B, occurs at $St = 0.01$. This implies that if their operating condition was to be met in the present research, it would lie in regime A, while for their

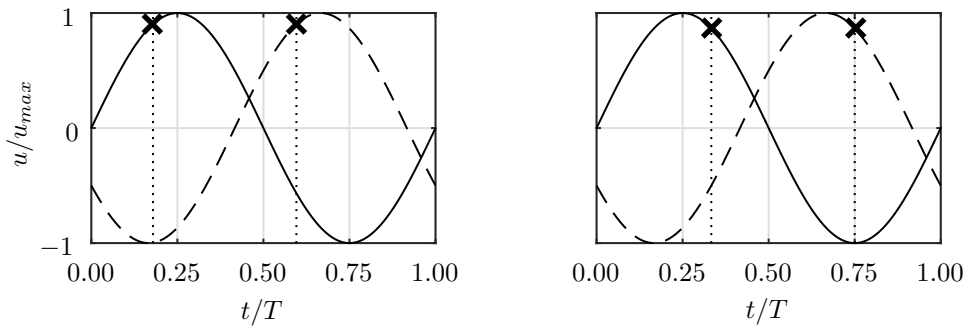

(a) $St = 0.02$, $\theta = 150°$, $t' = 0.18$

(b) $St = 0.06$, $\theta = 150°$, $t' = 0.33$

Figure 8: Velocity cycles with vortex pinch-off moments for equal phase differences but different Strouhal numbers. The continuous line represents the velocity as function of time for the leading actuator, the dashed line for the lagging actuator. Crosses indicate pinch-off time.

research it was in regime B, meaning that the exact conditions cannot be reproduced in the present research.

3.1.2 Dependency of vectoring behaviour on Reynolds number

The Reynolds number is varied for a fixed phase difference ($\theta = 150$ deg, jet on the right is leading in phase) and spacing ($\Delta/d = 2.0$). Note that these are the same phase difference and spacing as for the Strouhal variation discussed above. Cases are named (g), (h), (c′) and (d′) in order to build upon the six cases for the Strouhal variation and to stress that (c′) and (d′) have the same Strouhal numbers as (c) and (d) respectively. The location of the cases in the *St*–*Re* parameter space is indicated in Figure 5. These cases are not taken at a fixed Strouhal number, but at a fixed frequency in an attempt to illustrate the relative importance of Strouhal number compared to Reynolds number.

Normalized time-averaged velocity maps showing the vectoring behaviour for this variation are presented in Figure 9. Variation of Reynolds number only, for a fixed Strouhal number, is present between cases (c) and (c′), as well as between cases (d) and (d′). Both combinations show very little influence of the Reynolds number on the vectoring behaviour, especially when considering the directions of the individual branches as well as the total vectoring direction. However, it can be seen that as the Reynolds number increases for a given Strouhal number, the momentum flux in each branch of the vectored jets also increases. This is made clearer in the quantitative analysis section.

Case (h) represents a scenario that is not only at a different Reynolds number, but also at a different Strouhal number than the other cases. This Strouhal number, $St = 0.24$, approaches the formation criterion, as is visible in the parameter space in Figure 5. This causes a large part of the ejected fluid to be ingested back into the actuator during the

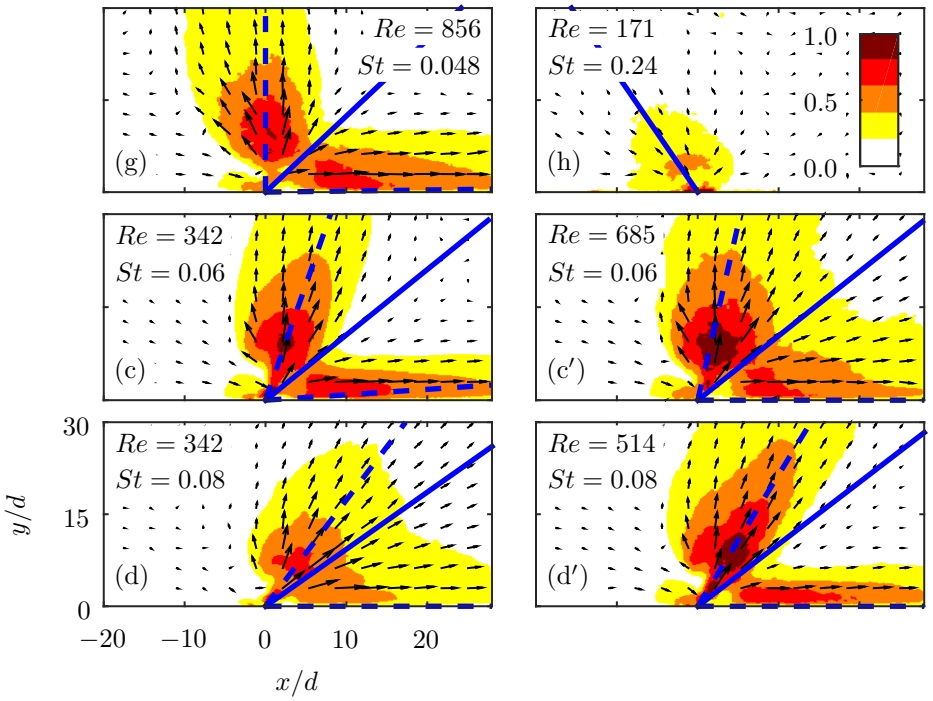

Figure 9: Normalized time-averaged velocity maps, $|u|/\bar{u}$, showing vectoring behaviour for different Reynolds and Strouhal numbers. For each case $\Delta/d = 2.0$ and $\theta = 150°$ with the actuator on the right leading in phase. The solid and dashed blue lines indicate the vectoring direction and directions of the individual branches as defined in Section 3.2. For clarity, only one in twenty vectors is displayed. Cases are indicated in the graph in Figure 5.

suction part of the cycle. This is observed in Figure 9h by the formation of a much weaker jet compared to the other cases.

3.1.3 Dependency of vectoring behaviour on phase difference and spacing

The phase difference and spacing are varied for a fixed Strouhal number ($St = 0.06$) and Reynolds number ($Re = 342$). These Strouhal and Reynolds numbers correspond to case (c) as presented in Figures 6 and 9. This case is adequately far away from both the formation criterion and the formation number, suggesting that a strong synthetic jet is formed that vectors towards the actuator leading in phase. Vortex trajectories for the baseline case with $\Delta/d = 2.0$ and $\theta = 150$ deg are presented in Figure 7b. Five phase differences, ranging from $\theta = 100$ deg to $\theta = 150$ deg and six spacings, ranging from $\Delta/d = 2.0$ to $\Delta/d = 3.0$ are tested, yielding a parameter space of 30 points. A selection of the time-averaged velocity maps, showing the full range of observed vectoring behaviour, is presented in Figure 10. Vectoring directions, defined by Equation 14, are indicated by the thick blue lines.

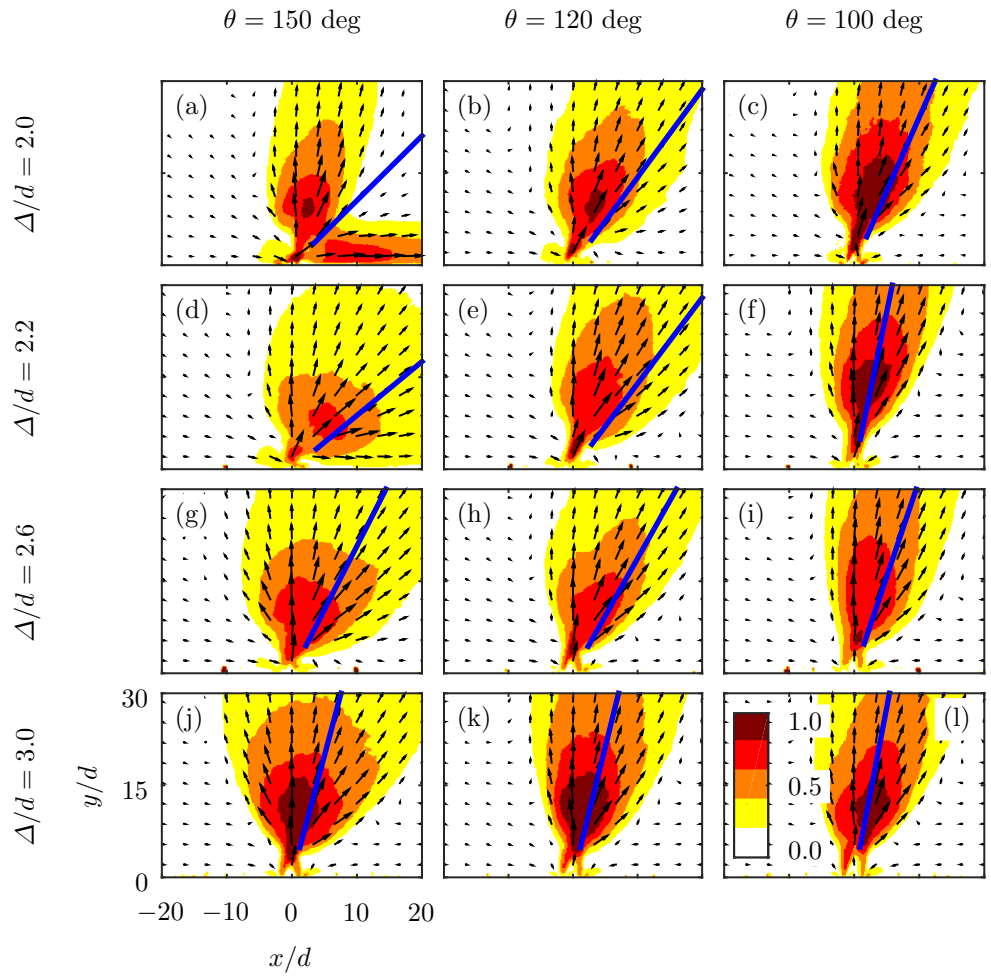

Figure 10: Normalized time-averaged velocity maps, $|u|/\bar{u}$, showing vectoring behaviour for different phase differences and spacings. Vectoring directions as defined by Equation 14 are indicated by the blue lines. For each case, $St = 0.06$, $Re = 342$ and the actuator on the right is leading in phase. For clarity, only one in twenty vectors is displayed.

Case (a), for $\Delta/d = 2.0$ and $\theta = 150$ deg, is the baseline case mentioned above. Interestingly, this is the only case that shows bifurcation. A mechanism describing bifurcation or merging of the two jets is presented in Section 3.3.

The vectoring angle decreases for both a decreasing phase difference (left-to-right) and for an increasing spacing (top-to-bottom). Although these variations have a similar effect on the vectoring angle, they produce qualitatively different flow fields. Decreasing the phase difference, i.e. bringing the leading and lagging vortex pairs closer together, results in a more compact merged jet. On the other hand, increasing the spacing, i.e. increasing the horizontal distance between the leading and lagging vortex pairs, leads to a wider merged jet. The variation of vectoring angle with phase difference and spacing is quantified and further analysed below.

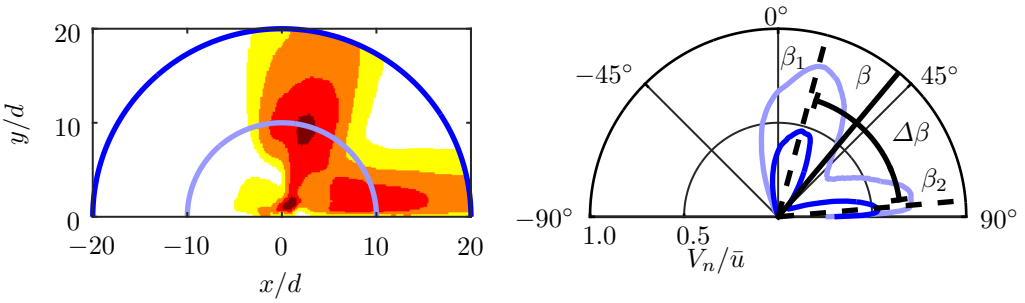

(a) Time-averaged velocity map (b) Normal velocity at circles in (a)

Figure 11: Time-averaged velocity map for the case shown in Figure 6c with circles at $r/d = 10$ and $r/d = 20$ (a) and the normalized normal velocities at these circles as function of the angle with respect to the vertical axis (b). The directions of both individual branches, β_1 and β_2, are indicated in (b), along with the vectoring angle, β and the included angle, $\Delta\beta$.

3.2 Quantitative analysis

To quantify the vectoring behaviour described above, the direction of individual branches, β_1 (deg) and β_2 (deg), the included angle between these branches, $\Delta\beta$ (deg), the total vectoring angle of the flow, β (deg) and the normalized momentum flux, $J'r/J_0$, are determined. The definition of these metrics is given using the example presented in Figure 11. Figure 11a shows the velocity field corresponding to the case in Figure 6c with two circles around the origin ($r/d = 10$ and $r/d = 20$). The normalized normal velocity at these circles, $V_n/\bar{u}$, as function of the angle with respect to the vertical axis is presented in Figure 11b. Note that in Figure 11a only the velocity magnitude for $r/d < 20$ is plotted, which is the part of the velocity used in the calculation of the vectoring angle.

The two bifurcated branches of the jet are clearly visible in the normal velocity as presented in Figure 11b. The direction of the individual branches is calculated from the angle at which the peaks are located. These peaks are detected with an estimated accuracy of one degree for 20 distances ranging from $r/d = 10$ to $r/d = 20$. The means of these peaks give the vectoring angles of the individual branches, β_1 (deg) and β_2 (deg). A typical rms variation of less than one degree is associated with this mean. The uncertainty in the peak detection and rms variation of the peaks adds up to approximately $\epsilon_{\beta_{1,2}} = 1.5$ deg, which leads to an uncertainty of approximately $\epsilon_{\Delta\beta} = 3$ deg for the included angle, $\Delta\beta$ (deg), which is defined as the angle between the two branches as indicated in Figure 11b, i.e.

$$\Delta\beta = |\beta_2 - \beta_1| \,. \tag{13}$$

The vectoring angle is defined as the total direction of the flow, taking into account the

flow within the circle $r/d = 20$ only, which is the largest (half-)circle that fits in the velocity fields as can seen from Figure 11a. This circle is used to remove a bias towards the horizontal or vertical side that would be present if the field of view extended further in either direction. This defines the vectoring angle as

$$\beta = \text{atan}\left(\sum V_x / \sum V_y\right), \tag{14}$$

for summations over the area within the circle $r/d = 20$.

The uncertainty propagation of the velocity into the calculation of the vectoring angle leads to an uncertainty of less than 0.1 degree. The typical rms variation associated with determining the vectoring angle for different distances from the origin is approximately two degrees. Combining the uncertainty propagation of the velocity and the rms variation leads to an uncertainty estimation of approximately $\epsilon_\beta = 2$ deg.

The time-averaged momentum flux per unit depth, J' (kg/s^2), is calculated from the time-averaged velocity maps by integrating the normal velocity component over (half-) circles around the origin, i.e.

$$J'(r) = \int_{-90}^{90} \rho V_n^2(r, \alpha) r \mathrm{d}\alpha, \tag{15}$$

with ρ (kg/m^3) the density of air, $V_n(r, \alpha)$ (m/s) the normal velocity with respect to the line of integration, r (m) the distance from the origin and α (deg) the angle with respect to the vertical line $x = 0$. This momentum flux per unit depth is normalized by the momentum flux added to the flow, J_0 (kg m/s^2), based on $A = ld$ and the momentum flow velocity, U_0 (m/s), as defined above. The normalized momentum flux per unit depth for the case with $St = 0.06$, $Re = 342$, $\Delta/d = 2.0$ and $\theta = 150$ deg is presented as function of r/d in Figure 13a. Representative for all cases, the momentum flux per unit depth decreases with approximately r^{-1} for values of roughly $r/d > l/d$ (note that $l/d = AR = 13$), indicating a three-dimensional jet development in the far-field. It was established in Section 3.1.1 that the vortex trajectories and therefore the vectoring behaviour is governed by the near-field and therefore assumed to be uninfluenced by this three-dimensional effect. Since only one plane is measured, the exact out-of-plane development of the jet is unknown. To account for the three-dimensional development, the momentum flux per unit depth is multiplied by the distance from the orifice, r. This leads to a constant momentum flux, $J'r$ (kg m/s^2), related (but not equal) to the total momentum flux.

The uncertainty propagation of the velocity into the normalized quantity $J'r/J_0$ scales with $1/\bar{u}$ and ranges from $\epsilon_{J'r/J_0} = 0.05$–$0.16$.

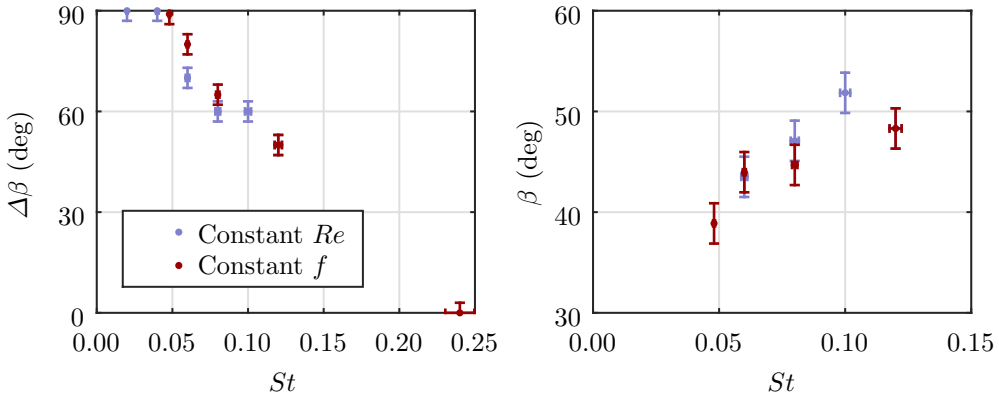

(a) included angle

(b) vectoring angle

Figure 12: Included angle, $\Delta\beta$ (deg), (a) and vectoring angle, β (deg), (b) as function of the Strouhal number for $\Delta/d = 2.0$ and $\theta = 150°$. For clarity, outlier cases with negative vectoring angles as shown in Figure 6 are omitted in (b).

3.2.1 Dependency of vectoring behaviour on Strouhal number

The included angle, $\Delta\beta$ (deg), is presented as function of the Strouhal number in Figure 12a. Note that for this quantitative analysis the Strouhal number and Reynolds number variations are lumped together. The included angle is $\Delta\beta = 90°$ up to approximately the formation number at $St \approx 0.05$, after which it decreases. The included angle decreases relatively linearly with Strouhal number for all points that have a constant pinch-off time (i.e. all points in regime B as defined in Figure 5).

The variation of vectoring angle with Strouhal number is plotted in Figure 12b. For clarity, the negative vectoring angles, corresponding to the cases in Figures 6a,b and 9h, are omitted. The vectoring angle shows an increasing trend with Strouhal number for the presented cases.

The normalized momentum flux, $J'r/J_0$, is presented as function of the Strouhal number in Figure 13b. Up to $St = 0.10$, the normalized momentum flux increases with Strouhal number. This indicates that less of the momentum added by the actuators is ingested back into the actuators during the suction phase. For higher Strouhal numbers, the normalized momentum flux rapidly decreases, caused by the approach of the formation criterion.

3.2.2 Dependency of vectoring behaviour on phase difference and spacing

The variation of vectoring angle with phase difference and spacing is plotted in Figure 14. The vectoring angle increases with phase difference up to a limit given by the spacing. The same pattern is observed for decreasing spacing, where the vectoring angle increases up to a limit given by the phase difference. This behaviour causes the variations to

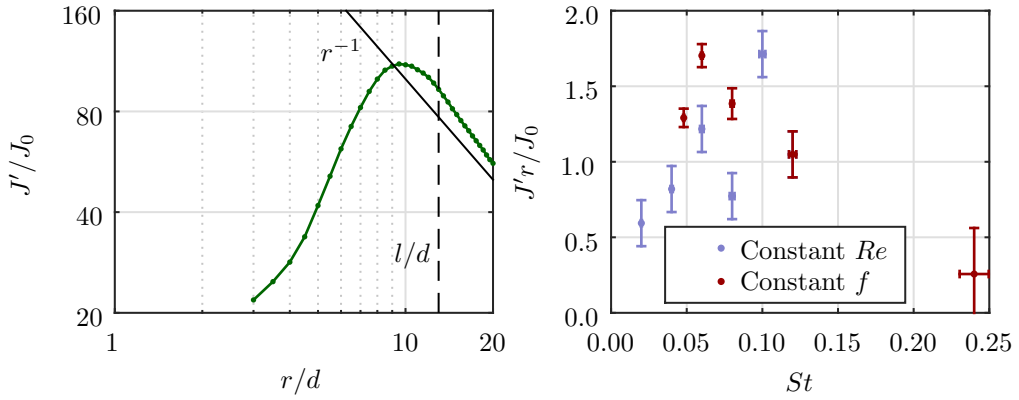

(a) example of J'/J_0 as function of r (b) $J'r/J_0$ as function of St

Figure 13: Example of the variation of normalized momentum flux per unit depth, J'/J_0, with distance from the slot, r/d, for $St = 0.06$, $Re = 342$, $\Delta/d = 2.0$ and $\theta = 150$ deg (a). Normalized momentum flux, $J'r/J_0$, as function of the Strouhal number for $\Delta/d = 2.0$ and $\theta = 150°$ (b).

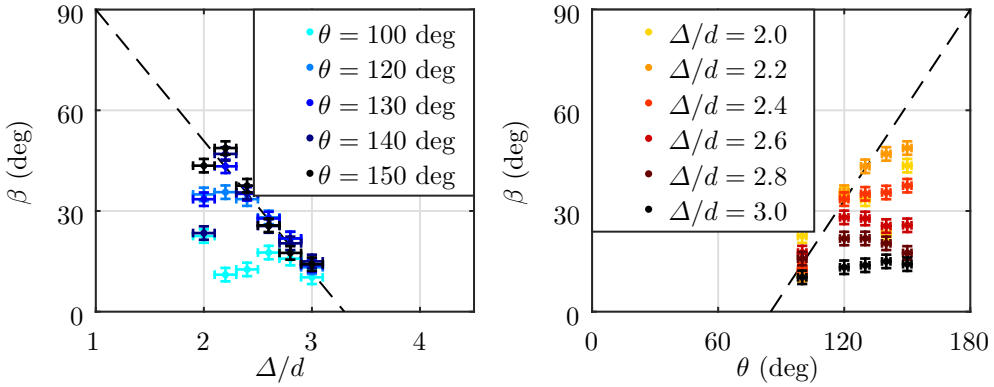

(a) (b)

Figure 14: Vectoring angle, β (deg), as function of the spacing, Δ/d, (a) and phase difference, θ (deg), (b) for $St = 0.06$ and $Re = 342$.

collapse onto two lines that suggest limiting behaviour. This collapse is indicated by the dashed lines in Figure 14.

The collapse of the vectoring angle onto these lines, and extrapolating those lines suggest that the maximum vectoring angle of 90 degrees (parallel to the plate) is reached at a phase difference of 180 degrees, which is the maximum possible phase difference and at a spacing of $\Delta/d = 1.0$, which is the minimum possible spacing without overlapping the slots. This limiting behaviour is an interesting point of further study, where it must be noted that decreasing the spacing towards $\Delta/d = 1.0$ becomes increasingly hard since no material is present between the slots for this limit.

The lower limits of the vectoring angle indicate that vectoring does not occur at low

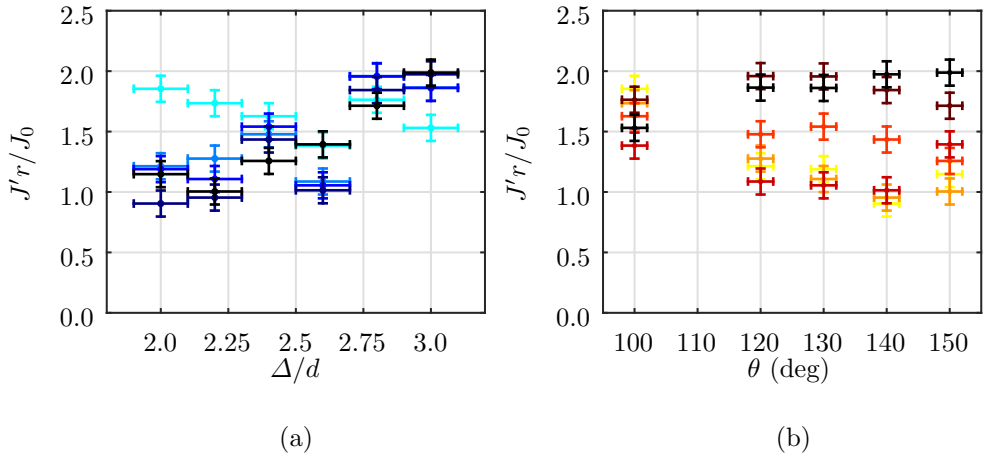

Figure 15: Normalized momentum flux $J'r/J_0$ as function of the spacing, Δ/d, (a) and phase difference, θ (deg), (b) for $St = 0.06$ and $Re = 342$. See Figure 14 for legend.

phase differences, which is in agreement with the findings by Smith and Glezer (2005) and neither at large spacings. It should be noted that Smith and Glezer (2005) observed vectoring for a phase difference as small as 60 degrees and a spacing of $3.3d$, which is beyond both limits shown in Figure 14.

The variation of normalized momentum flux with phase difference and spacing is plotted in Figure 15. The normalized momentum flux increases with spacing for all phase differences except $\theta = 100$ deg, for which it stays relatively constant. This increase is caused by less of the momentum of either jet being ingested into the neighbouring actuator. For $\theta = 100$ deg the influence of suction is less than for higher phase differences, as witnessed by the lower vectoring angles, causing ingestion of momentum to be absent and therefore invariant with spacing.

In a similar way, for small spacings the normalized momentum flux decreases for increasing phase difference, caused by more momentum being ingested into the neighbouring actuator. For larger spacings, ingestion of momentum is less prominent, causing less variation in the normalized momentum flux.

3.3 Physical mechanism describing vectoring behaviour

A physical mechanism that explains the variation in vectoring behaviour with the key parameters can be proposed based on the observations of the vortex trajectories obtained from phase-locked PIV data. This mechanism is valid for regime B as defined in Figure 5 only where the vortex pinch-off is at a fixed time (i.e. $t' \approx 1/3$). These vortex trajectories depend on the trade-off between the suction velocity of the actuator that is leading in phase, the induced velocity of the leading vortex pair and the distance between the vortex pairs from the lagging actuator and the leading actuator. Phase-locked vorticity maps for two cases with different Strouhal number are presented to demonstrate how

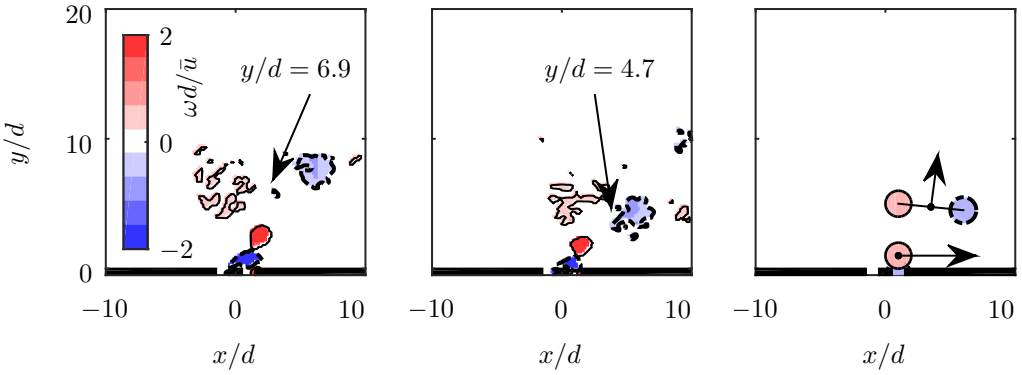

(a) $St = 0.06$ (b) $St = 0.10$ (c) Schematic of (b)

Figure 16: Phase-locked vorticity maps, showing vortex locations for $St = 0.06$ (a) and $St = 0.10$ (b), both for $Re = 342$, $\Delta/d = 2.0$ and $\theta = 150$ deg. The arrows in the schematic (c) indicate self-induced velocities of the vortex pair and the anticlockwise vortex. Red background with solid contour lines indicates positive vorticity, blue background with thick dashed contours indicates negative vorticity.

the time-averaged vectoring behaviour can be reconciled based on the vortex trajectories that depend on the trade-off between the three contributions. This mechanism is then extended to include variations in Reynolds number, spacing and phase difference.

Phase-locked vorticity maps for $St = 0.06$ and $St = 0.10$, with $Re = 342$, $\Delta/d = 2.0$ and $\theta = 150$ deg are shown in Figure 16a and 16b. Vortex positions are identified using the swirling strength and the vorticity outside these positions is set to zero. Both cases are phase-locked at the phase for which the clockwise rotating vortex produced by the actuator lagging in phase is about to be ingested into the leading actuator. In both cases, the vortex pair originating from the actuator leading in phase (actuator on the right) has propagated in the vertical direction. A schematic, representing the vortex positions in Figure 16b, is presented in Figure 16c for clarity. The vortex pair has a self-induced velocity perpendicular to its axis, whereas the single anticlockwise vortex has a strong self-induced velocity towards the right, caused by the presence of its image vortex due to its vicinity to the surface. These self-induced velocities are indicated by the arrows in this schematic. The strong self-induced velocity of the single vortex prevents the branches from merging and creates a bifurcated jet. The Strouhal number ($St = 0.10$) corresponds to the case in Figure 6e and indeed the arrows point in the direction of the bifurcated branches for this case.

The locations of the vortex pair centres in Figure 16a and 16b are indicated by the arrow tips. The vertical positions (y/d) of the leading vortex pairs are annotated in the graphs. The vortex pair originating from the actuator lagging in phase is influenced by the suction velocity of the actuator leading in phase, causing the vortex pair to rotate clockwise and move towards the right. The influence of the Strouhal number on the vertical location of the leading vortex pair can be considered using potential flow theory.

During the formation of the vortices, the circulation, Γ (m^2/s), grows as $\mathrm{d}\Gamma/\mathrm{d}t \approx u^2(t)/2$ (Shariff and Leonard, 1992). Assuming a jet velocity as given by Equation 1 and a fixed pinch-off time (which is the case for regime B considered here), the circulation scales with $\Gamma \propto \bar{u}^2/f$ (note that $\Gamma \propto Re/St$).

If the distance between the vortices within a vortex pair scales with the slot width (this is a reasonable assumption since the vortices are created at the edges of the slot), the self-induced velocity of the vortex pair scales as $u_\Gamma \propto \Gamma/d \propto \bar{u}^2/(fd)$. The vertical position of the leading vortex pair, y (m) will depend on the time since its creation (that varies as θ/f) and its self-induced velocity. Therefore, the vertical position will vary as $y/d \propto \theta/St^2$. This inverse relation with the Strouhal number is evident in Figure 16, where the vertical position of the centre of the leading vortex pair decreases from the $St = 0.06$ to the $St = 0.10$ case.

The closer proximity for the higher Strouhal number causes more interaction between the two vortex pairs. This leads to a decrease in the included angle between the two jets as presented in Figure 12a. The reduced vertical position (y/d) of the leading vortex pair increases the induced velocity on the lagging vortex pair in the direction opposite to the suction velocity. This causes less of the lagging jet to be ingested into the leading actuator and thereby increases the normalized momentum flux as shown in Figure 13b. This increase in momentum flux mainly contributes to the horizontal momentum flux and thereby also increases the vectoring angle as shown in Figure 12b. The changes to the schematic in Figure 16c for this variation with Strouhal number are presented in the schematics in Figure 17a–c, corresponding to the cases in Figure 6c,e,f.

For the $St = 0.12$ case, the distances from the single vortex to the leading vortex pair becomes close enough for the single vortex to be lifted away from the surface due to the velocity induced by the leading vortex pair as well as the low pressure region in the wake of this pair. This causes the horizontal branch of the jet to become detached from the surface and shortly after its creation merge with the branch formed by the leading vortex pair, as is visible in the time-averaged flow field in Figure 6f.

A variation of Reynolds number can also be considered, starting from the same vortex positions as in Figure 17a. As discussed above, the vertical position of the leading vortex pair scales with θ/St^2, meaning that Reynolds number has no effect on the position of the vortices. However, the strength of the vortices, given by the circulation which scales as Re/St, will be different. This change in vortex strength will be proportional for all the vortices, meaning that the interactions remain constant and therefore will not affect the vectoring behaviour. This is reflected in Figure 9, where a change in Reynolds number does not lead to a significant change in the vectoring behaviour exhibited by the time-averaged flow field.

The above discussed physical mechanism based on vertical location of the vortex pair can also capture the influence of spacing. The vertical position of the leading vortex pair (scaling with θ/St^2) is invariant for changes in the spacing. However, increasing

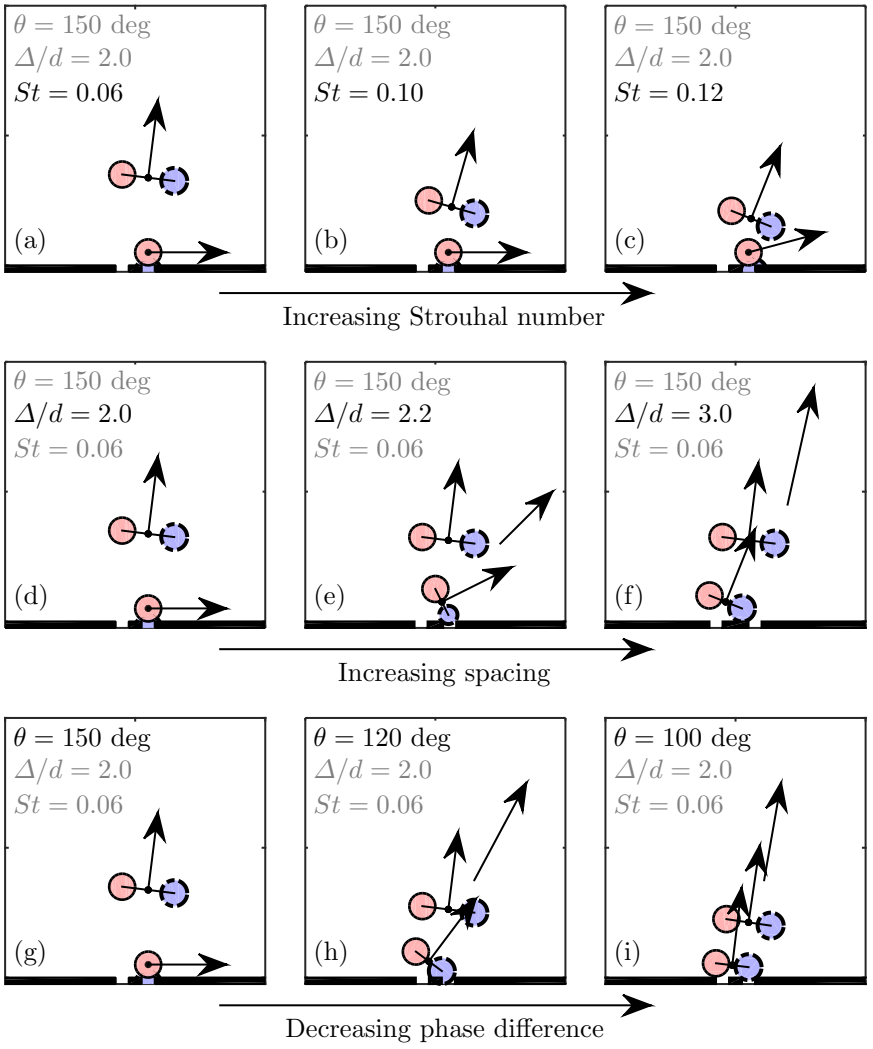

Figure 17: Schematic representations of phase-locked vorticity maps, explaining the vectoring behaviour for the different parametric variations discussed in this study.

the spacing will cause the effect of the suction velocity on the lagging vortex pair to decrease. This is reflected in Figure 17d–f, corresponding to the cases in Figure 10a,d,j. Increasing the spacing to $\Delta/d = 2.2$ leads to the clockwise vortex of the lagging vortex pair not being completely ingested in the leading actuator. This means that there is no distinct horizontal branch originating from a single vortex above the surface and the branches will merge as is visible in Figure 10d. The large difference in orientation of the vortex pairs as indicated in Figure 17e leads to a wide merged jet as in Figure 10d. Further increase in the spacing leads to less of the clockwise vortex being ingested into the leading actuator and a smaller rotation of the lagging vortex pair. For the $\Delta/d = 3.0$ case as presented in Figure 17f, no part of the clockwise vortex is ingested into the leading actuator and the lagging vortex pair is only slightly rotated. The lagging vortex pair is attracted by the low pressure wake of the leading vortex pair, inducing a velocity on the lagging vortex pair towards the right. This will cause a wide merged jet, as visible

in Figure 10j, but lowering the vectoring angle for increasing spacing as observed in Figure 14a.

Finally, the same physical description can be used to explain the behaviour with varying phase difference where both the vertical position of the leading vortex pair and the effect of suction are altered. Starting from the same baseline case ($St = 0.06$, $Re = 342$, $\Delta/d = 2.0$ and $\theta = 150$ deg), a decrease in phase difference is considered as presented in Figure 17g–i, corresponding to the cases in Figure 10a–c. Decreasing the phase difference to $\theta = 120$ deg decreases the vertical position of the leading vortex pair (scaling with θ/St^2) as presented in Figure 17h. In addition, the effect of suction on the lagging vortex pair decreases, leading to the clockwise vortex not being ingested into the leading actuator. Each vortex pairs is subjected to an induced velocity normal to its axis, while the lagging vortex pair is also attracted by the low pressure wake of the leading vortex pair, leading to a merged jet vectored towards the leading actuator. Further decreasing the phase difference to $\theta = 100$ deg as presented in Figure 17i diminishes the effect of suction on the lagging vortex pair. This implies that the vortex pairs are aligned and very close together. The lagging vortex pair is attracted by the low pressure wake of the leading vortex pair, causing it to move slightly towards the leading actuator and merging with the leading vortex pair. This causes a compact merged jet, vectored towards the actuator leading in phase as observed in Figure 10c.

Although beyond the scope of the experiments in the present study, the influence of the aspect ratio on the presented two-dimensional mechanisms can be considered. A decrease in aspect ratio will increase three-dimensional effects not considered here. Ignoring these three-dimensional effects, the aspect ratio has another influence, as presented in Equation 10. For increasing aspect ratio, the Strouhal number corresponding to the formation number (i.e. the dashed line in Figure 5) will decrease. This means that regime B increases and more cases will pinch-off at $t' = 1/3$, but this will not change anything for the cases already in regime B as considered in the presented mechanism. For a decreasing aspect ratio this limiting Strouhal number will increase. This implies that cases in regime B might shift to regime A, thus pinching off sooner and therefore producing vortex pairs with less circulation. A decrease in circulation means that the effect of suction increases relative to the effect of self-induced velocity. Therefore, for a smaller aspect ratio, cases will bifurcate more easily and the cases in for example Figure 17e and 17h might still lead to a bifurcated jet instead of a merged jet.

4 Conclusions

The vectoring of parallel synthetic jets can be described using five dimensionless parameters: the aspect ratio, Strouhal number, Reynolds number, spacing and phase difference. This study presents an experimental parametric study of the latter four, while using a fixed aspect ratio that we show to be large enough for the vectoring behaviour in the

central plane of measurement to be dominated by a two-dimensional flow. Three regimes for the Strouhal number are defined. In the first regime the vectoring behaviour is dominated by the vortex pinch-off time. This study shows that – for a given actuator – the pinch-off time is a function of Strouhal number only. In the second Strouhal number regime the pinch-off time is invariant. A parametric study of all four parameters is performed inside this regime. In the third regime, no synthetic jet is formed due to the formation criterion.

For a small spacing ($\Delta/d = 2.0$) and high phase difference ($\theta = 150$ deg) a bifurcated jet is formed with one vertical branch and one branch attached to the surface in the direction of the actuator leading in phase. It is shown that this bifurcation is the result of one of the vortices being ingested during the suction phase of the neighbouring actuator. For increasing Strouhal number the included angle between these branches decreases, while the total vectoring angle and the normalized momentum flux increase.

The variation of Reynolds number shows that (for multiple Strouhal numbers) a change in Reynolds number has negligible effect on both the included angle and the vectoring angle.

Increasing the spacing decreases the effect of suction on the neighbouring vortex pair. It is shown that for spacings larger than $\Delta/d = 2.0$ vortices are no longer ingested during the suction phase, cancelling bifurcation and leading to a wide merged jet. For increasing spacing, the vectoring angle becomes smaller, while the normalized momentum flux generally becomes larger.

Decreasing the phase difference also decreases the effect of suction on the neighbouring vortex pair. For phase differences lower than $\theta = 150$ deg vortices are no longer ingested during the suction phase, cancelling bifurcation and leading to a compact merged jet. For a decreasing phase difference, the vectoring angle decreases and the normalized momentum flux either decreases (for small spacings) or is invariant (for larger spacings).

A physical mechanism – based on vortex locations at a single phase shortly after creation of the lagging vortex pair – is proposed that explains the vectoring behaviour for the full parameter space. This mechanism describes how some cases lead to ingestion of one of the vortices and bifurcation of the jet, while others do not. The relative location of the lagging vortex pair compared to the leading pair is used in the mechanism to describe the vectoring angle.

The results obtained in this research are relevant to flow control applications such as thrust vectoring and lay a groundwork for applications in which a crossflow is present. The quantification of the variation of included angle, vectoring angle and momentum flux increases the level of control over the synthetic jets. The insights obtained in the present study can be used both in the design phase of a control system (e.g. jets with a specific spacing) as well as in the operational phase (e.g. actuating the jets with a specific Strouhal number, Reynolds number and phase difference).

Paper 2

Entrainment effects in periodic forcing of the flow over a backward-facing step

Tim Berk, Takfarinas Medjnoun and Bharathram Ganapathisubramani

Aerodynamics and Flight Mechanics Research Group, University of Southampton, Southampton SO17 1BJ, UK

Phys. Rev. Fluids, **2**:074605, 2017.

The effect of the Strouhal number on periodic forcing of the flow over a backward-facing step (height, H) is investigated experimentally. Forcing is applied by a synthetic jet at the edge of the step at Strouhal numbers ranging from $0.21 < St_H < 1.98$ ($St_H = fH/U_\infty$) at a Reynolds number of $Re_H = HU_\infty/\nu = 41000$. In previous studies, the effect of Strouhal number on the reattachment length is often divided into low- and high frequency actuation, in relation to the frequencies present in the unforced flow. In the present study, variations with Strouhal number are explained based on a continuous variation of entrainment of momentum into the recirculation region rather than on specific frequencies. The reattachment length is shown to decrease linearly with entrainment of momentum. Vertical momentum flux is driven by vortices generated by the forcing and locally vertical momentum flux is shown to be qualitatively similar to circulation for all cases considered. Total circulation (and therewith entrainment of momentum and the effect on the reattachment length) is shown to decrease with Strouhal number whereas this is not predicted by models based on specific low- and high frequencies. An empirical model for the (decay of) circulation is derived by tracking vortices in phase-locked data. This model is used to decipher relevant scaling parameters that explain the variations in circulation, entrainment of momentum and reattachment length. Three regimes of Strouhal number are identified. A low-Strouhal-number regime is observed for which vortices are formed at a late stage relative to the recirculation region, causing a decrease in effectiveness. For high Strouhal numbers vortices are being re-ingested into the actuator or are packed so close together that they cancel each other, both decreasing the effectiveness of forcing. In the intermediate regime a vortex train is formed of which the decay of circulation increases for increasing Strouhal number. The scaling of this decay fully explains the observed variation in reattachment length. The observations on entrainment of momentum made in this study are expected to also hold for periodic forcing of other bluff-body flows.

1 Introduction

The flow over a backward-facing step separates from the edge of the step and reattaches further downstream. Aerodynamic drag as caused by separation can account for more than 50% of fuel consumption in transport (Hucho and Sovran, 1993). Most drag reduction strategies focus either on increasing the pressure recovery or on streamlining the body using elongation of the wake (Barros et al., 2016b). The present paper focusses on the latter by studying the effect of forcing on the length of the wake.

The size of the wake is quantified by defining a recirculation region where the local (mean) velocity is in the direction opposite to the mean flow ($\widetilde{U}_x < 0$). The reattachment point is defined as the point on the wall where the time-averaged horizontal flow switches back from negative to positive (i.e. $\widetilde{U}_x = 0$). The length of the recirculation region (or reattachment length) is the distance from the base of the step to the reattachment point.

This length can be manipulated using local forcing of the flow. Examples of forcing methods applied in the literature are an oscillating flap (Nagib et al., 1985), steady blowing (Littlewood and Passmore, 2012), steady suction (Sano et al., 2009), pulsed jets (Barros et al., 2016b,a), pulsed plasma actuators (Roupassov et al., 2009) or synthetic jets (Chun and Sung, 1996; Dandois et al., 2007; Henning and King, 2007; Dahan et al., 2012; Oxlade et al., 2015). Apart from the steady suction and blowing, these are all periodic forcing methods. Particularly for high forcing frequencies (Dandois et al., 2007; Vukasinovic et al., 2010), this periodic forcing has the ability to dampen the flow unsteadiness and stabilise the shear layer, which is assumed to lower the entrainment of momentum into the recirculation region, which causes an elongation of this recirculation region. However, periodic forcing typically generates a train of vortices, leading to an increase in entrainment of momentum and shortening the recirculation region. The balance between these two effects determines whether a net increase or decrease in reattachment length is achieved.

In recent years, feedback and feed-forward control strategies have been developed to selectively control disturbances (Hervé et al., 2012; Gautier and Aider, 2014). It has been shown numerically that the turbulent kinetic energy of the incoming flow can be reduced by more than 90% using feed-forward control (Hervé et al., 2012). A reduction of the amplitude of incoming perturbations has been shown to lead to a decrease in entrainment, which increases the reattachment length. Machine learning control was used experimentally by Gautier et al. (2015) to optimize the feedback control law for the flow over a backward-facing step. This optimized control performs similar to periodic forcing at design conditions and outperforms periodic forcing for off-design conditions. Their experiments show the technical feasibility of real-time control at a Reynolds number of $Re_H = 1350$. The present research focusses on harmonic forcing at higher Reynolds numbers which are closer to Reynolds numbers associated with practical applications.

Periodic forcing of the flow over a backward-facing step using a spoiler-like flap was

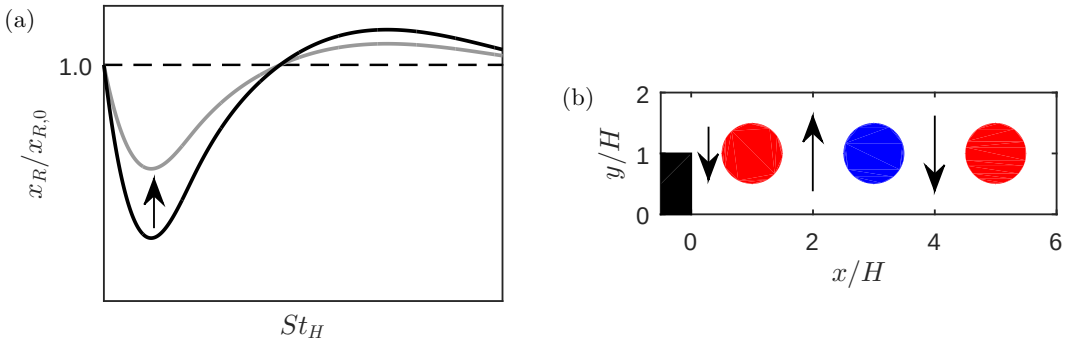

Figure 1: (a) Schematic of the effect of Strouhal number on reattachment length. The dashed line indicates the unforced reattachment length. The arrow indicates a decrease in either the forcing amplitude or a decrease in free-stream Reynolds number for constant forcing amplitude. (b) Schematic of alternating positive and negative vortices with corresponding induced velocities between them as leading mechanism for entrainment.

investigated by Nagib et al. (1985). The reattachment length showed to scale with the Strouhal number, defined as

$$St_H = \frac{fH}{U_\infty}, \tag{1}$$

where f is the forcing frequency, H is the step height and U_∞ is the free-stream velocity. The same scaling is used by Kiya et al. (1993), who investigated forcing of the leading-edge separation of a blunt axisymmetric body using synthetic jets. They found that (for a constant Strouhal number) an increase in free-stream Reynolds number or in forcing amplitude increases the effect of forcing.

Similar results are obtained by Chun and Sung (1996) for forcing of the flow over a backward-facing step using synthetic jets. For a range of free-stream Reynolds numbers the reattachment length, x_R, decreases sharply for low Strouhal numbers, reaching a minimum around $St_H = 0.2$–0.3 where the reattachment length is decreased to as little as $x_R/x_{R,0} = 0.65$, where $x_{R,0}$ represents the unforced length. Beyond this minimum, for increasing Strouhal numbers, the reattachment length recovers, reaching the initial value around $St_H = 0.8$–1.0 and overshooting slightly to as much as $x_R/x_{R,0} = 1.05$. This is presented schematically in Figure 1a, where the black curve shows the trend for a baseline case and the grey line represents a decrease in either the forcing amplitude (defined as $A_j = u/U_\infty$, the ratio between the jet velocity and the crossflow velocity) or a decrease in free-stream Reynolds number for a constant forcing amplitude.

In more recent years, development of both computational (DNS, LES) and experimental (PIV) techniques have made it easier to quantify velocity fields, aiding in the investigation of the exact mechanisms causing the changes in reattachment length discussed above. Dandois et al. (2007) used DNS and LES to investigate the frequency effect of a synthetic jet on the separation of a rounded ramp. They distinguish two cases, labelled

a low frequency ($St_H = 0.14$) and a high frequency ($St_H = 1.15$) case. Their data shows that for the low frequency case large spanwise vortices are formed with the flow between each vortex being reattached. In the time-averaged sense, this leads to a reduction of the reattachment length to $x_R/x_{R,0} = 0.46$, attributed to an increase in entrainment of high-momentum fluid into the recirculation region caused by the created vortices. In contrast, the high-frequency case does not produce clear vortices and the synthetic jet actuator is said to operate in acoustic dominated mode, decreasing the amplitude of incoming perturbations in the flow. The reduction of perturbations stabilizes the shear layer between the cross-flow and the recirculation region and reduces the entrainment of momentum into this region, leading to an increase in reattachment length to $x_R/x_{R,0} = 1.43$.

Dahan et al. (2012) explored numerically open- and closed-loop control of a backward-facing step using synthetic jets. The open-loop actuation shows very similar results to the experimental study by Chun and Sung (1996), decreasing the reattachment length for $St_H < 0.8$ and slightly increasing it for $0.8 < St_H < 2$.

Forcing of the wake behind a bluff axisymmetric body is studied experimentally by Oxlade et al. (2015). The range of Strouhal numbers tested is approximately $1.0 < St_H < 6.0$ (St_H is based on radius of the body). As expected from the above mentioned literature, no significant reduction of the recirculation region is expected for this range of Strouhal numbers. The shortest reattachment length reported is $x_R/x_{R,0} = 0.97$, showing analogy between this three-dimensional wake and a two-dimensional step.

The trend of the reattachment length as a function of the Strouhal number as presented schematically in Figure 1a reappears in all cases discussed above, regardless of the type of body causing the separation or the forcing method. As discussed above, the reattachment length decreases sharply for low Strouhal numbers. In the literature, this is attributed to a high rate of entrainment caused by large vortices (Chun and Sung, 1996; Dandois et al., 2007). For increasing Strouhal numbers – after reaching a minimum – the reattachment length starts recovering towards the initial value. This decrease in effectiveness is attributed to the size of vortices decreasing, leading to lower entrainment, for an increasing Strouhal number. At some point ($St_H = 0.8$–1.0, (Chun and Sung, 1996)) the reattachment region reaches its unforced length and even overshoots slightly. This increase in reattachment length compared to the unforced case is generally attributed to a stabilisation of the shear layer, reducing entrainment (Dandois et al., 2007; Oxlade et al., 2015).

The entrainment caused by vortices is represented schematically in Figure 1b. Alternating clockwise and counterclockwise vortices induce alternating positive and negative velocity components in the wall-normal direction. A negative (downwards) velocity component entrains high-momentum fluid into the recirculation region, whereas a positive (upward) component extracts low-momentum fluid from the recirculation region, leading to an increase in average momentum in the recirculation region.

In the literature it is generally assumed that the creation of larger vortices (lower forcing frequency) leads to a higher rate of entrainment. Theoretically, the circulation Γ_j ($\mathrm{m^2 s^{-1}}$) created by a synthetic jet per unit time is given by

$$\frac{\mathrm{d}\Gamma_j}{\mathrm{d}t} = \frac{1}{2}u_j^2(t), \tag{2}$$

where $u_j(t)$ (m/s) is the jet velocity (Shariff and Leonard, 1992). This jet velocity is assumed to be constant over the slot and harmonic in time, i.e.

$$u_j(t) = u \sin\left(2\pi t f\right), \tag{3}$$

where u (m/s) is the maximum jet velocity and f (Hz) is the actuation frequency. Integrating Equation 2 over a single blowing period leads to a circulation per velocity cycle of

$$\Gamma_j = \int_0^T \frac{1}{2}u_j^2(t)\mathrm{d}t = \frac{u^2}{4f}, \tag{4}$$

where $T = 1/f$ (s) is the period of the velocity cycle. Since each velocity cycle creates a vortex pair (Smith and Glezer, 1998), the number of vortices created per unit time is given by $N = 2f$. This means that the total circulation created per unit time scales as $\Gamma_j N \propto u^2$, which shows that although the circulation per vortex scales with the actuation frequency, the total circulation per unit time is independent of the actuation frequency. Therefore, the assumption often made in the literature that entrainment decreases for an increasing frequency (smaller vortices) is not necessarily true.

It should be noted that there are multiple macroscopic length scales present in the flow. Assuming that the step height is kept constant, this can be replaced by (for example) the constant boundary-layer thickness (δ), momentum thickness (θ) or displacement thickness (δ^*) of the incoming flow without loss of generality. Following the bulk of the literature, the present paper uses the step height as macroscopic length scale for non-dimensionalization.

The purpose of the present paper is to reassess the influence of Strouhal number on the reattachment length and identify the driving physical mechanisms of variations with Strouhal number. This is studied experimentally by forcing the flow over a backward-facing step using synthetic jets, actuated at four different Strouhal numbers. Across the four cases, the flow conditions for the incoming flow as well as the geometry of the step are kept constant. The changes in local momentum thickness as a result of actuation are small compared to the changes in actuation length scales.

First, time-averaged velocity fields showing the reattachment region are presented and the variation of reattachment length with Strouhal number is discussed globally. This is followed by phase-locked velocity and vorticity fields, showing a train of alternating

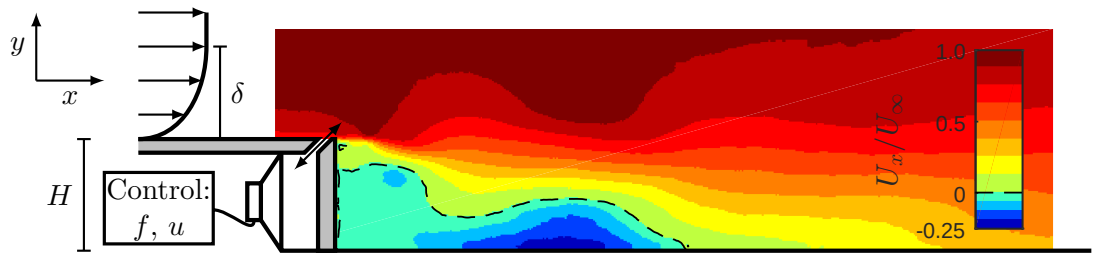

Figure 2: Schematic of the actuator and an example of the phase-locked horizontal velocity field (U_x/U_∞) for $St_H = 0.21$.

vortices as driving mechanism for entrainment. The formation and evolution of this train of alternating vortices is studied using phase-locked vorticity maps. Next, the time-averaged momentum flux and circulation as a result of this vortex train are presented and compared between the different cases. Observed variations in entrainment of momentum are explained using tracked trajectories and circulation of the vortices. Scaling factors for the development of the vortex location and circulation in time and space are derived and the trajectories and circulation are fitted against analytical and empirical formulae. Finally, a reconsideration of Strouhal-number regimes that highlights the effects on entrainment of momentum is discussed.

2 Experimental set-up and procedures

2.1 Description of the step and separating flow

The separating flow over a two-dimensional backward-facing step of height $H = 0.05$ m, spanning the entire width of the test section ($H/z = 0.056$), is considered. The incoming flow consists of a fully-developed turbulent boundary layer with a free-stream velocity of $U_\infty = 12$ m/s ($Re_H = HU_\infty/\nu = 41000$), a boundary layer thickness of $\delta_{99} = 0.074$ m, a friction Reynolds number of $Re_\tau \approx 2600$ and a momentum thickness of $\theta = 0.0054$ m ($Re_\theta = 4400$). In absence of actuation, the flow separates from the top of the step and reattaches at a downstream location of $x_{R,0} = 0.226$ m ($x_{R,0}/H = 4.52$), measured from the base of the step.

2.2 Description of the synthetic jet actuator

The separating flow is forced using a synthetic jet at the edge of the step. The synthetic jet is actuated using a series of in-phase Visaton SC 8 N speakers placed side-by-side. The speakers are attached to a single cavity that has a neck with a length of 6 mm and placed at an angle of 45 degrees to both the horizontal and vertical face of the step. The jet is issued from a slit that has a width $d = 0.5$ mm. Four forcing cases (using sinusoidal actuation as in Equation 3) are considered with actuation frequencies $f = 50$, 116, 204 and 476 Hz, corresponding to Strouhal numbers $St_H = 0.21$, 0.48, 0.85 and 1.98 (see

Table 1 for Strouhal numbers based on θ). The jet velocity is measured in absence of a crossflow and has a peak blowing velocity of $u = 20$ m/s for each case. A schematic of the cross-section of the step and actuator is presented in Figure 2.

2.3 Measurement procedures

Measurements are performed in the University of Southampton's suction wind tunnel. The test section of this tunnel measures 4.5 m in streamwise direction, 0.9 m in spanwise direction and 0.6 m in wall-normal direction. Velocity fields are determined using two-dimensional, two-component particle image velocimetry (PIV). The PIV system consists of two aligned Litron 200 mJ dual-pulse Nd-YAG lasers and three LaVision Imager Pro LX 16MP cameras, fitted with 105 mm focal-length lenses. The width of the laser sheet is approximately 1 mm. Seeding is provided by a Martin Magnum 1200 smoke machine, producing particles with a mean diameter of 1 μm. For each case, 480 image pairs per phase are recorded for eight equidistant phases, phase-locked to the actuation signal. Vectors are determined using a first pass with a window size of 64 $\times$ 64 pixels, followed by a second pass of 24 $\times$ 24 pixels with 50% overlap, resulting in a resolution of one vector per 0.7 mm. Velocity fields are corrected for pixel-locking as described by Hearst and Ganapathisubramani (2015).

The field of view extends between $-0.5 < x/H < 14$ in streamwise direction and $0 < y/H < 2$ in wall-normal direction, both measured with the origin located at the base of the step. Since (with exception of the $St_H = 0.21$ case) vortices can only be tracked up to $x/H < 6$ and all recirculation regions end before this value, all flow fields will be presented with streamwise extent $-0.5 < x/H < 6$. The measurement plane is located at the spanwise centre of the wind tunnel and synthetic jet. It is assumed that the flow in the measurement plane is largely two-dimensional. The analysis is based on the measurement of the reattachment length and spanwise vortices, both of which are defined for in-plane components only and would not be influenced by unexpected out-of-plane motions.

3 Results and discussion

Time-averaged and phase-locked velocity and vorticity fields are presented for selected cases in Sections 3.1 and 3.2 respectively. The formation of the observed vortical structures is exemplified using phase-locked images in Section 3.3. Section 3.4 discusses the effect of these structures on the time-averaged momentum flux and circulation. Variations are explained by tracking vortex trajectories and magnitudes in Section 3.5. Relevant scaling parameters and equations are derived based on these observations and applied in Section 3.6. The discussion is concluded with the identification of different regimes of Strouhal number in Section 3.7.

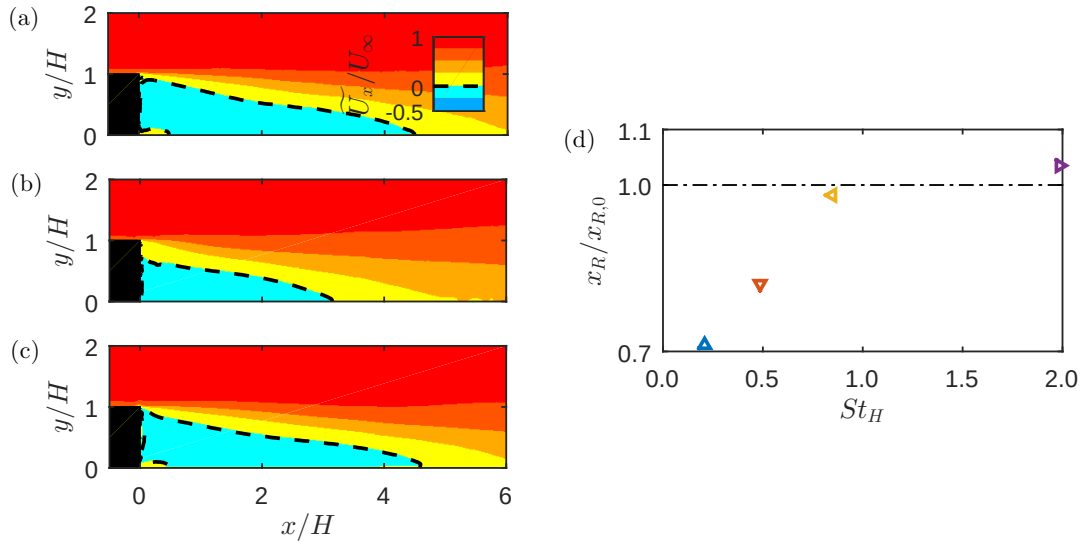

Figure 3: Time-averaged horizontal velocity component ($\widetilde{U_x}/U_\infty$), indicating the recirculation regions in absence of actuation (a), for $St_H = 0.21$ (b) and $St_H = 1.98$ (c). The dashed line indicates the contour for $\widetilde{U_x} = 0$. Reattachment lengths are compared in (d) where the dash-dotted line indicates the reattachment length in absence of actuation.

Table 1: Reattachment length for all cases

St_H	0	0.21	0.48	0.85	1.98
St_θ	0	0.02	0.05	0.09	0.21
f (Hz)	0	50	116	204	476
x_R/H	4.52	3.22	3.71	4.44	4.68

3.1 Time-averaged velocity and reattachment length

Normalized time-averaged velocity fields showing the streamwise velocity component, $\widetilde{U}_x$, are presented in Figure 3 for the baseline case without actuation (a) as well as for the $St_H = 0.21$ (b) and $St_H = 1.98$ (c) cases. All cases show a clear recirculation region – defined as the part of the flow where $\widetilde{U}_x < 0$ – bounded by the dashed lines in Figure 3. The reattachment length, x_R, is defined as the streamwise extent of the recirculation region for $y = 0$, i.e. the location at which the dashed line reaches the x-axis. Reattachment lengths are quantified for all four Strouhal numbers as presented in Figure 3d. For low Strouhal numbers, the reattachment length is significantly shorter than in absence of actuation, indicated by the dash-dotted line. The reattachment length increases with Strouhal number and grows beyond the unperturbed length for high Strouhal numbers. Values of the normalized reattachment length, x_R/H, are tabulated for the unforced case and the four forcing cases in Table 1.

As discussed in Section 1, the observed variations in reattachment length imply that there is a balance between increasing and decreasing effects of the forcing on this length. Depending on the Strouhal number, this balance will lead to an elongated or a shortened reattachment length. Following the literature, it is assumed that the main effect

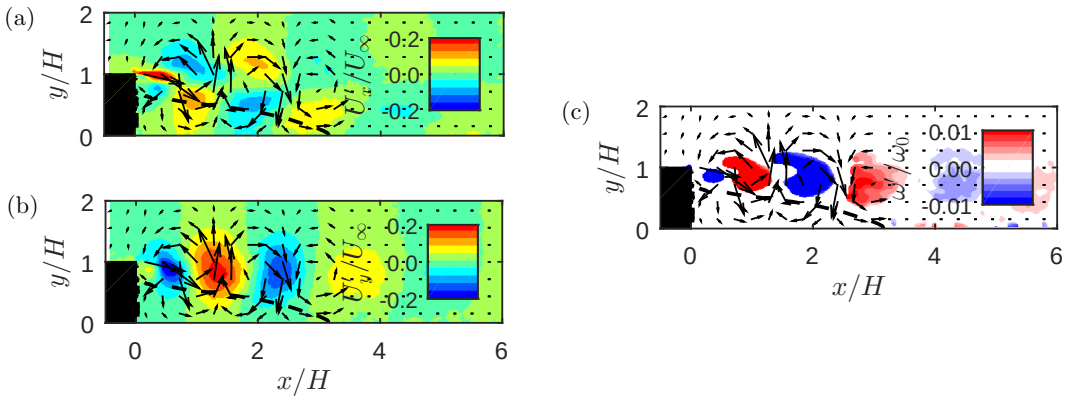

Figure 4: Normalized phase-locked horizontal- (U'_x/U_∞, a) and vertical- (U'_y/U_∞, b) velocity fluctuations for the $St_H = 0.21$ case. The vorticity (ω'/ω_0, c) is plotted at regions identified as vortices using swirling strength.

increasing the reattachment length is a stabilization of the shear layer by a reduction of disturbances in the incoming flow. The main effect shortening the reattachment length is assumed to be entrainment of momentum into the recirculation region.

The alternating nature of the flow in the wall-normal direction as presented schematically in Figure 1b is not present in the time-averaged velocity fields. Phase-locked data is used to study these alternating components of the flow.

3.2 Phase-locked velocity components and vorticity

Normalized phase-locked velocity and vorticity fields for a single phase of the $St_H = 0.21$ case are presented in Figure 4. Observed structures are qualitatively similar for all forcing cases. The flow fields are represented as fluctuations (normalised by U_∞), which are obtained by subtracting the time-averaged velocity from the phase-averaged velocity ($U' = U_{phase} - \widetilde{U}$, where the tilde denotes a time-averaged quantity). Velocity vectors are overlaid on the velocity and vorticity maps. Note that for clarity only one in 20 vectors is displayed. The normalized horizontal- and vertical velocity fluctuations, phase-locked near the end of the blowing phase, are presented in (a) and (b) respectively.

The horizontal velocity component shows a small jet at the top of the step, which is created by the blowing phase of the synthetic jet. The direction of this jet shows that although the synthetic jet is injected into the flow at an angle of 45 degrees, the relatively high momentum of the cross-flow immediately deflects the jet into the horizontal direction. Further downstream of the step an oscillating pattern of increased and decreased streamwise velocity components is visible.

The vertical velocity component (b) also shows an oscillating motion of positive and negative wall-normal velocities. Positive wall-normal velocity transports low-momentum (or momentum of opposite direction) fluid out of the recirculation region, while negative

wall-normal velocity injects high-momentum fluid into the recirculation region. Both effects lead to an increase (or entrainment) of momentum in the recirculation region.

The normalized vorticity field corresponding to these velocity fields is presented in (c). In this vorticity field the vorticity outside vortices is set to zero. Vortices are identified using swirling strength, which is defined as the imaginary part of the complex conjugate eigenvalues of the two-dimensional velocity gradient tensor (see Adrian et al. (2000)). The vorticity is calculated from the phase-averaged velocity fluctuations ($\omega' = \mathrm{d}U'_y/\mathrm{d}x - \mathrm{d}U'_x/\mathrm{d}y$) and normalized by $\omega_0 = \Gamma_j/A$, where Γ_j is the circulation as given by Equation 4 and A (m^2) is the volume of fluid exerted per velocity cycle, given by

$$A = Ld = \int_0^T u_j(t)\mathrm{d}t\, d = \frac{ud}{\pi f}, \tag{5}$$

where $u_j(t)$ (s) is defined by Equation 3, $L = u/(\pi f)$ (m) is the length of the theoretical slug of fluid ejected by the actuator each cycle and d (m) is the slot width. The vorticity field indicates that the alternating nature of the flow is caused by alternating clockwise and counterclockwise vortices. Given that a synthetic jet creates pairs of counterrotating vortices (see for example Smith and Glezer (1998)), the pattern of single alternating vortices is surprising. The formation of vortices is investigated by looking at the full vorticity field for multiple phases.

3.3 Vortex formation and creation of train of vortices

To identify the mechanisms leading to the train of alternating vortices as observed in Figure 4c, phase-locked vorticity fields for the peak of the blowing cycle (a) and the peak of the suction cycle (b) are presented in Figure 5. An annotated video showing all eight measured phases is available in the Supplementary Material. Note that the vorticity fields in Figure 5 show the full vorticity field including shear layers and vortices, in contrast to Figure 4c where the swirling strength is applied such that only vortices are displayed. As shown in Figure 4a and discussed above, the jet is formed from the edge of the step directed in positive x-direction. During the blowing phase (Figure 5a) this jet leads to a counterclockwise (red coloured) shear layer above it and a clockwise (blue coloured) shear layer beneath it. In absence of a cross-flow, these shear layers would roll up into vortices, creating a vortex pair that convects away from the orifice and forms a train of vortex pairs (Smith and Glezer, 1998). However, during the suction phase (Figure 5b) two shear layers of opposite direction as during the blowing phase are formed due to interaction with the cross-flow. Driven by the cross-flow, these shear layers convect in streamwise (positive-x) direction. As can be seen from Figure 5, the positive shear layer created during the blowing phase connects to and merges with the positive shear layer created during the previous suction phase to form a single counterclockwise vortex. In contrast, the negative shear layer created during the blowing

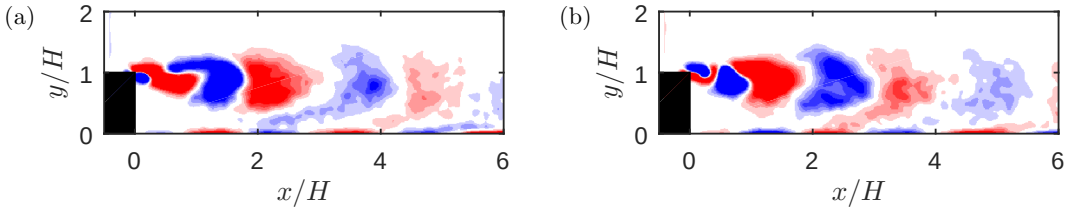

Figure 5: Normalized phase-locked vorticity fields (ω'/ω_0) at the peak of the blowing cycle (a, $t/T = 0.25$) and the peak of the suction cycle (b, $t/T = 0.75$). See Figure 4c for colour scale.

phase merges with the negative shear layer created by the next suction phase, creating a single clockwise vortex. The alternating forward and backward merging of the opposite vortices leads to the train of alternating vortices observed in Figure 4c and consequently to the alternating nature of the velocity fields as in Figures 4a and b.

3.4 Time-averaged entrainment of momentum

The described alternating train of vortices and corresponding alternating wall-normal velocity component as presented in Figure 4b leads to net entrainment of momentum into the recirculation region. The downward motion injects high-momentum fluid into the recirculation region while the upward motion removes low-momentum fluid from the recirculation region. The entrainment of momentum into the recirculation region is given by the momentum flux through the boundary of this region. The momentum flux through the boundary of the recirculation region is approximated by the vertical momentum flux through the line $y/H = 1$. It should be noted that presented results are insensitive to changes in the exact height of this line. Total momentum (per unit length in streamwise, wall-normal and spanwise directions) is calculated from phase locked velocity fields, i.e. $P_{phase} = \rho U_x + \rho U_y$. Note that the contribution of the wall-normal velocity to the total momentum is relatively small and the same conclusions are reached when considering streamwise momentum only. The phase-locked vertical momentum flux (per unit length in streamwise and spanwise directions) is given by

$$\dot{P}_{y,phase}(x,y,t) = (\rho U_x(x,y,t) + \rho U_y(x,y,t))(-U'_y(x,y,t)|_{U'_y<0}), \tag{6}$$

where $-U'_y|_{U'_y<0}$ represents the negative (downward) vertical component only. The time-averaged vertical momentum flux (per unit length in streamwise and spanwise directions), $\dot{P}_y(x,y)$, is calculated by averaging over the eight phases, i.e.

$$\dot{P}_y(x,y) = \frac{1}{T}\int_0^T \dot{P}_{y,phase}(x,y,t)\mathrm{d}t. \tag{7}$$

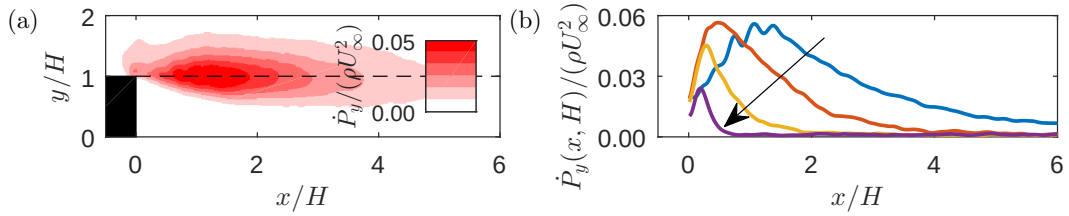

Figure 6: Time-averaged vertical momentum flux, $\dot{P}_y(x, y)$, for the $St_H = 0.21$ case (a). Time-averaged vertical momentum flux through the line $y/H = 1$, $\dot{P}_y(x, H)$, for all cases (b). $St_H = 0.21$ (—), $St_H = 0.48$ (—), $St_H = 0.85$ (—) and $St_H = 1.98$ (—) (colour online), the arrow indicates increasing Strouhal number.

Entrainment of momentum into the recirculation region, approximated by total vertical momentum flux through the line $y/H = 1$ (per unit length in spanwise direction) is given by

$$\int \dot{P}_y(x, y/H = 1)\mathrm{d}x. \tag{8}$$

The time-averaged vertical momentum flux for the $St_H = 0.21$ case is presented in Figure 6a. The time-averaged vertical momentum flux through the line $y/H = 1$ as a function of x/H is presented in Figure 6b. The arrow indicates increasing Strouhal number. The peak in vertical momentum flux travels upstream for an increase in Strouhal number. For the three lowest Strouhal number cases the peak is of similar magnitude but decreases more rapidly for the higher Strouhal numbers. Maximum momentum flux for the highest Strouhal number case is significantly lower.

The entrainment of momentum into the recirculation region (as approximated by Equation 8) is presented as function of the Strouhal number in Figure 7a. The entrainment of momentum decreases for increasing Strouhal number. The relation between the reattachment length and entrainment of momentum into the recirculation region is presented in Figure 7b. The reattachment length decreases linearly with entrainment of momentum. Comparing Figure 7b with Figure 3d indicates that entrainment of momentum is a better predictor of reattachment length than the Strouhal number is, suggesting that entrainment of momentum is the driving force for changes in reattachment length.

As discussed above, it is assumed that entrainment of momentum is primarily caused by vortices. The time-averaged vorticity for the $St_H = 0.21$ case is presented in Figure 8a. This time-average is conditioned to positive vorticity, $\widetilde{\omega'_+} = \widetilde{\omega'}|_{\omega'>0}$, with swirling strength applied, leading to the contribution of the counterclockwise vortices only. Note that the contribution of clockwise vortices is equal but opposite as will be discussed below. The vorticity distribution has roughly the same shape as the vertical momentum flux distribution presented in Figure 6a. To compare the different cases, the vorticity is integrated over the wall-normal extent shown in Figure 8a. This integral of vorticity can be seen as circulation per unit length in the streamwise direction and is given by

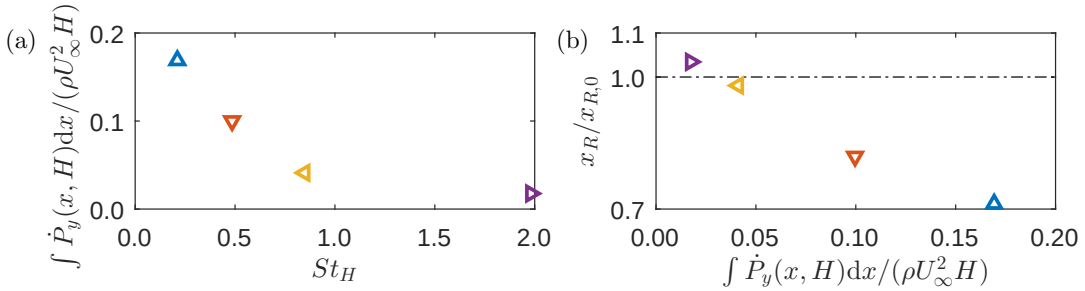

Figure 7: Entrainment of momentum into the recirculation region as function of Strouhal number (a) and reattachment length as a function of entrainment of momentum (b) for $St_H = 0.21$ (▵), $St_H = 0.48$ (▿), $St_H = 0.85$ (◁) and $St_H = 1.98$ (▷).

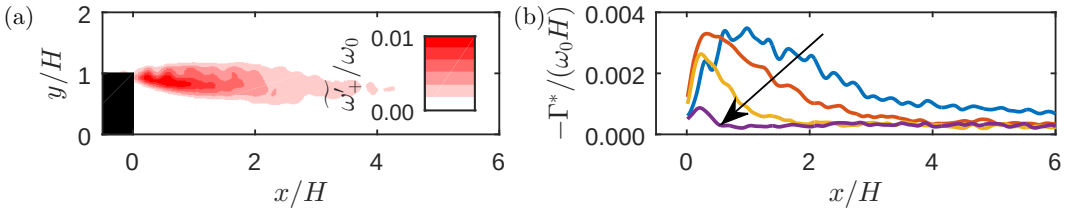

Figure 8: Time-averaged positive vorticity ($\widetilde{\omega'_+}/\omega_0$) with swirling strength applied for the $St_H = 0.21$ case (a). Time-averaged circulation per unit length (Γ^*) as a function of x/H for all cases (b). $St_H = 0.21$ (—), $St_H = 0.48$ (—), $St_H = 0.85$ (—) and $St_H = 1.98$ (—) (colour online), the arrow in (b) indicates increasing Strouhal number.

$$\Gamma^*(x) = -\int_0^{2H} \widetilde{\omega'_+}(x,y)\mathrm{d}y. \tag{9}$$

This circulation is presented for all four cases in Figure 8b. The arrow indicates increasing Strouhal number. For the three lowest Strouhal numbers the initial circulation reaches the same maximum, which is due to the strength and number of vortices balancing each other as discussed in the introduction. The shape of the circulation distribution is qualitatively similar to the vertical momentum flux distribution presented in Figure 6b for all cases and the entire range, indicating a strong link between circulation and vertical momentum flux. This is exemplified in Figure 9, where the vertical momentum flux through the line $y/H = 1$ is presented as a function of the circulation. For clarity, a distinction is made for data up to the peak in circulation (lighter shade) and downstream of this peak (darker shade). There is a relatively constant ratio between the two (indicated by the black line), which is most evident beyond the peaks in circulation. The link between circulation and vertical momentum flux suggests that the decrease in entrainment of momentum for higher Strouhal numbers (and therewith the increase in reattachment length) can be attributed to the faster decay of circulation with streamwise distance for these Strouhal numbers.

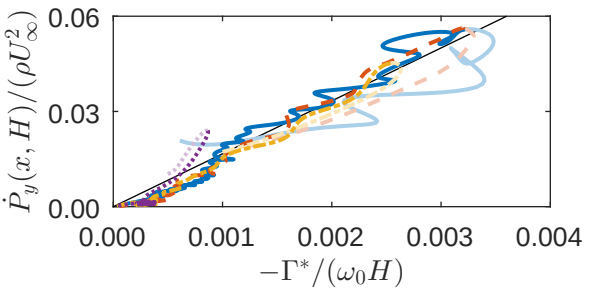

Figure 9: Time-averaged vertical momentum flux through the line $y/H = 1$ ($\dot{P}_y(x,H)$) as a function of time-averaged circulation per unit length (Γ^*) for all cases. $St_H = 0.21$ (▬), $St_H = 0.48$ (▬), $St_H = 0.85$ (▬) and $St_H = 1.98$ (▬) (colour online). Lighter shades correspond to the part where circulation (and entrainment) is increasing with streamwise location.

To determine the mechanism behind this change in decay of circulation for higher Strouhal numbers, individual vortices are tracked, measuring their circulation and location as functions of time.

3.5 Vortex tracking

Vortices, as presented in Figure 4c for a single phase, can be tracked through time. The tracking method is illustrated in Figure 10. Rectangles are manually drawn around the approximate region of a vortex. Inside this region, vorticity of the appropriate sign is integrated to determine the circulation of the vortex, i.e.

$$\Gamma_{\mathrm{CCW}} = -\sum_{x_0}^{x_1}\sum_{y_0}^{y_1} \omega'(x,y)|_{\omega'>0}\Delta x\Delta y, \tag{10}$$

where CCW depicts that we are looking at a counterclockwise (positive vorticity) vortex and x_0, x_1, y_0 and y_1 indicate the lower and upper bounds in horizontal and vertical direction respectively. A similar equation is used for the clockwise vortices with the only difference being the condition that the vorticity is negative ($\omega'|_{\omega'<0}$). The location of the vortex is defined as the weighted centre of vorticity, calculated as

$$x_\Gamma = \frac{1}{\Gamma}\sum_{x_0}^{x_1}\sum_{y_0}^{y_1} x\,\omega'(x,y)\Delta x\Delta y, \tag{11}$$

$$y_\Gamma = \frac{1}{\Gamma}\sum_{x_0}^{x_1}\sum_{y_0}^{y_1} y\,\omega'(x,y)\Delta x\Delta y. \tag{12}$$

For the vortex identified in Figure 10, this leads to a circulation of $\Gamma = -0.11$ m^{2}s^{-1} and

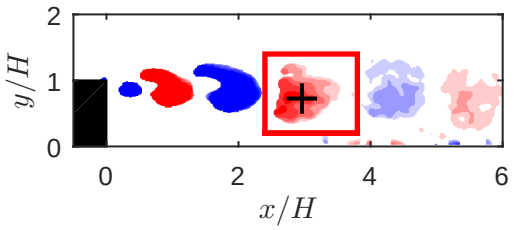

Figure 10: Example of the vortex tracking method. Vorticity is plotted at regions identified as vortices using swirling strength for the $St_H = 0.21$ case. See Figure 4c for colour bar. A vortex is identified inside the manually drawn rectangle. The calculated location of the vortex is identified by the black cross.

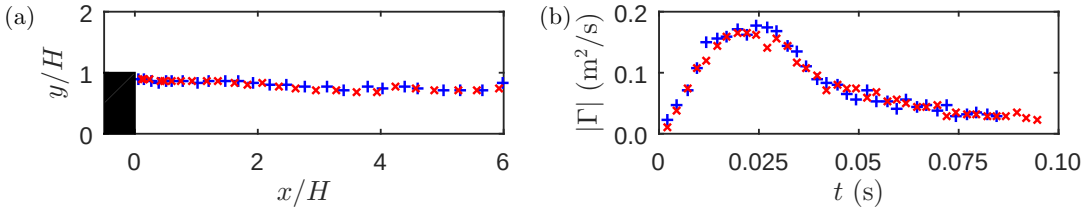

Figure 11: Comparison of tracked location (a) and absolute circulation (b) between positive (+) and negative (×) vortex for the $St_H = 0.21$ case.

a location of $x/H = 2.96$, $y/H = 0.73$. The circulation and location are tracked throughout the field of view for all eight phases for the four cases. Due to a decay in circulation of the vortices, at some point they can no longer be identified as coherent structures and tracking becomes impossible. The limit for this tracking typically corresponds to the point where the circulation has decayed to about 10% of the maximum circulation for each vortex. This means that the faster decaying vortices at higher Strouhal numbers can be tracked for a shorter period of time.

The tracked location (a) and circulation (b) for the positive and negative vortex independently for the $St_H = 0.21$ case are presented in Figure 11. Both the trajectories and the absolute values of circulation as a function of time show a remarkable similarity between the positive (clockwise) and negative (counterclockwise) vortex. The collapse of characteristics for the positive and negative vortex is observed for all four cases. Because of this collapse the positive and negative vortices are treated as one in the subsequent analysis, effectively doubling the number of tracked points.

3.5.1 Vortex trajectories

Vortex trajectories are tracked as presented for the $St_H = 0.21$ case in Figure 11a. For all cases, the vertical location is relatively constant and equal to the location of the jet. The horizontal location as a function of time is presented for all four cases in Figure 12a. The vortices all start at the same location, $x = 0$, with initial velocity $\mathrm{d}x/\mathrm{d}t = 0$. Due to momentum transfer from the cross-flow to the vortices, they show an acceleration until

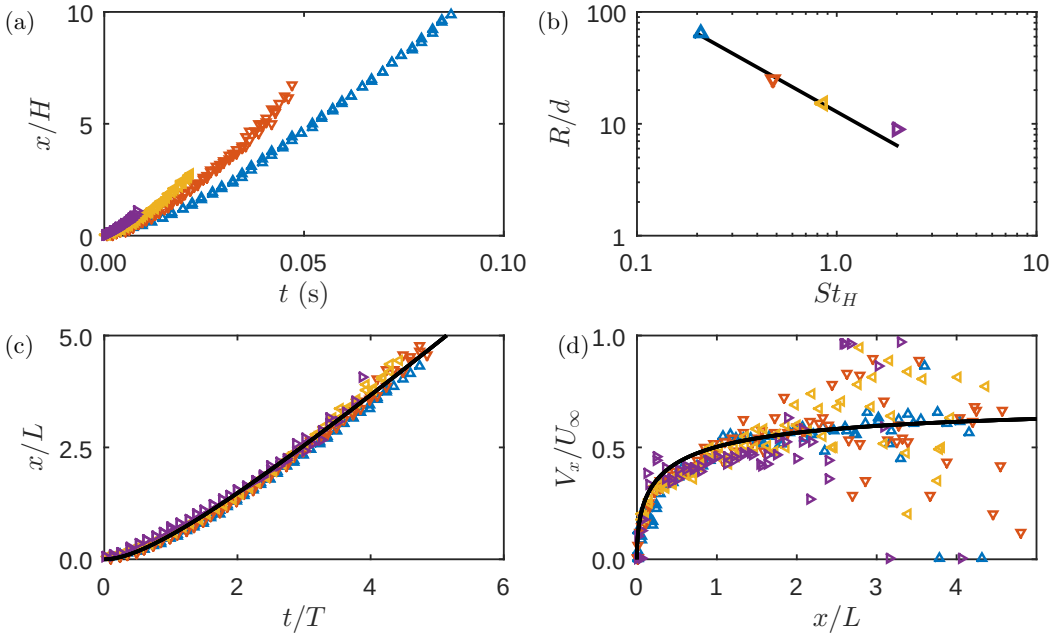

Figure 12: Tracked vortex trajectories and size for $St_H = 0.21$ (△), $St_H = 0.48$ (▽), $St_H = 0.85$ (◁) and $St_H = 1.98$ (▷). Horizontal vortex location as a function of time (a). Vortex radius as used for scaling (b) the black line indicates a decrease with 1/f. Scaled vortex location and time (c) the black line indicates the trajectory given by Equation 16. Normalized horizontal convection velocity of the vortices as a function of scaled horizontal location (d) the black line indicates the convection velocity given by Equation 15.

they reach a relatively constant velocity. Because of their smaller size, the acceleration is higher for the vortices corresponding to the high frequency case, which is manifested by the horizontal location increasing more rapidly with time in Figure 12a.

An analytical model for the horizontal propagation of vortices is derived with the goal of obtaining (the physics behind) proper scaling laws. This model is based on the assumption that the (horizontal) acceleration of the vortices is driven by the local cross-flow velocity, U_x^*, impacting on half of the frontal area of the vortices, R (with the other half being shielded by the step, see for example the first vortex in Figure 1b). The radii of the vortices for each case are presented in Figure 12b, where the black trend-line indicates a decrease of the radius as $R \propto 1/f$. This relation is unexpected given that the theoretical radius based on the (two-dimensional) volume A given by Equation 5 equals $R = \sqrt{A/\pi} = \sqrt{ud/(\pi^2 f)}$, scaling with $1/\sqrt{f}$. The fact that the measured radius scales with $1/f$ can be explained by the vortices entraining fluid until a full train is formed, as is visible in Figures 4 and 5 where the alternating vortices are packed closely together. Since the distance between vortices per definition scales with $1/f$, their radius must then scale in the same way.

Using this radius, the momentum transferred to each vortex by the local flow velocity can be described as

$$\frac{\mathrm{d}P}{\mathrm{d}t} = \rho R(U_x^* - V_x)^2, \tag{13}$$

where U_x^* is the local flow velocity and V_x is the convection velocity of the vortex. This momentum flux equals a force that will accelerate the vortex ($\mathrm{d}P/\mathrm{d}t = m\,\mathrm{d}V_x/\mathrm{d}t = \rho\pi R^2\,\mathrm{d}V_x/\mathrm{d}t$), where the acceleration is then given by

$$\frac{\mathrm{d}V_x}{\mathrm{d}t} = \frac{(U_x^* - V_x)^2}{\pi R}. \tag{14}$$

Assuming that U_x^* is a constant (which is a reasonable assumption given that the wall-normal location of the vortices is constant as observed in Figure 11) this can be integrated with respect to t to give the convection velocity,

$$\frac{V_x}{U_x^*} = \frac{U_x^*\, t/(\pi R)}{1 + U_x^*\, t/(\pi R)}, \tag{15}$$

where the initial condition $V_x(0) = 0$ is used.

Using the definition that $V_x = \mathrm{d}x/\mathrm{d}t$, this can be integrated with respect to t again to give the trajectory,

$$\frac{x}{\pi R} = U_x^* \frac{t}{\pi R} - \ln\left(1 + U_x^* \frac{t}{\pi R}\right), \tag{16}$$

where the initial condition $x(0) = 0$ is used.

An important finding from Equations 15 and 16 is that both x and t scale with $1/R$. As discussed above, $R \propto 1/f$, implying that the period $T = 1/f$ or the slug length $L = u/(\pi f)$ can also be used for scaling. The trajectories are replotted in Figure 12c, now with the location scaled as x/L and the time scaled as t/T. The normalized convection velocity of the vortices, with the location scaled as x/L, is presented in Figure 12d. With the axes scaled in this way, the trajectories and convection velocities show a remarkable similarity across the four cases. The value of U_x^* is determined from the data as the convection velocity asymptotes to approximately $U_x^* = 0.7U_\infty$. The trajectory and velocity predicted by Equations 15 and 16 is represented by the black lines in Figures 12c and d. The model predicts the velocities and trajectories reasonably well for the complete data set.

3.5.2 Vortex circulation

The absolute value of the circulation per vortex as a function of time is presented in Figure 13a for all four cases, all showing the same general trend. Up to some point in time

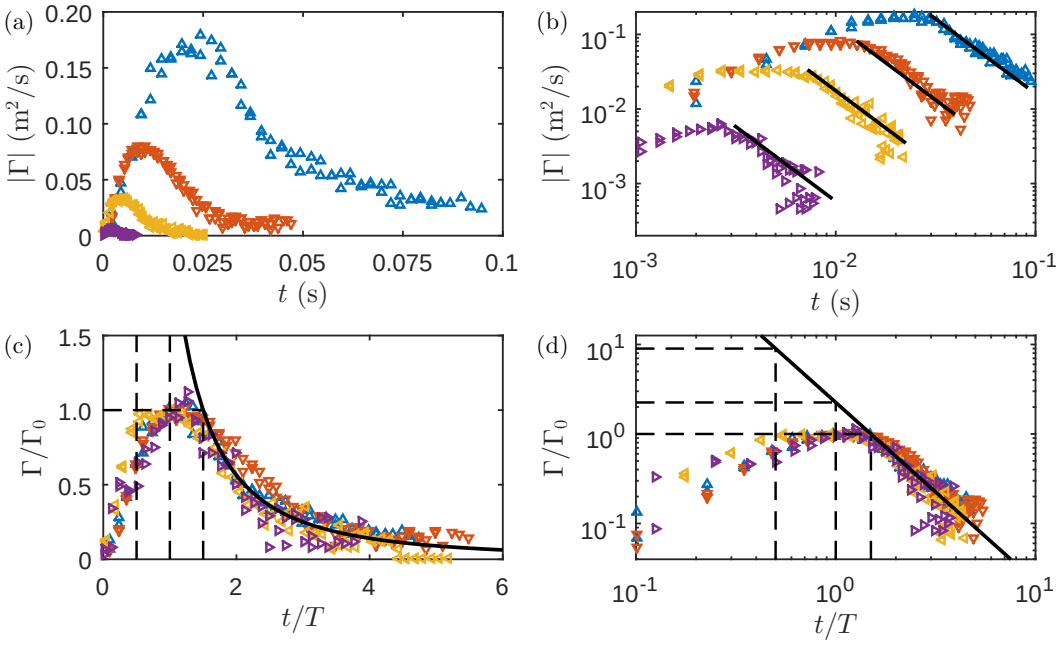

Figure 13: (Absolute) circulation tracked as a function of time for $St_H = 0.21$ (▵), $St_H = 0.48$ (▿), $St_H = 0.85$ (◁) and $St_H = 1.98$ (▷). The data is presented on (a) linear and (b) log-log axes. The black trend-lines in (b) show a decay of t^{-2}. Normalized circulation as a function of scaled time on linear (c) and log-log axes (d). The black lines indicate the decay of circulation as given by Equation 18. Dashed lines indicate the values at $t/T = 0.5$, 1.0 and 1.5.

the circulation grows due to formation of the vortex. As expected from Equation 4, the magnitude of the peak circulation roughly scales with the inverse of frequency. After this peak the circulation starts decaying. The vortices can be tracked up to approximately 10% of the peak circulation, which is longer in time for lower frequencies.

When presented on log-log axes as in Figure 13b, all four cases show the same decay rate. The black lines overlaid on the data indicate a decay with t^{-2}, which corresponds well to the data. This decay rate can be used to analyse the scaling between the cases. An initial value of circulation (Γ_0) is reached at the start of the constant decay (t_0), i.e. $\Gamma(t_0) = \Gamma_0$. This time t_0 is associated with the end of the formation of the vortex. If we let $\Gamma(t) = C/t^2$ during the decay period, this constant C can be determined using the initial condition, $C/t_0^2 = \Gamma_0$, leading to

$$\frac{\Gamma(t)}{\Gamma_0} = \left(\frac{t_0}{t}\right)^2, \tag{17}$$

valid for the decay part only. It can be determined empirically that the constant decay starts at $t_0 = 3/2\,T$ for all four cases, leading to

Table 2: Ratio of measured versus theoretically produced circulation

St_H	0.21	0.48	0.85	1.98
f (Hz)	50	116	204	476
Γ_0/Γ_j	0.10	0.10	0.08	0.03
$\Gamma(T/2)/\Gamma_j$	0.90	0.90	0.72	0.27

$$\frac{\Gamma(t)}{\Gamma_0} = \frac{9}{4}\left(\frac{T}{t}\right)^2 = \frac{9}{4}\left(tf\right)^{-2}. \tag{18}$$

This relation indicates that for adequate comparison between cases, time should be scaled with the actuation frequency. The normalized circulation, $\Gamma(t)/\Gamma_0$, is presented as a function of the scaled time, t/T, in Figure 13c and d. As expected the data now collapses for the four cases. This collapse is not only present during the decay period on which the scaling is based, but also during vortex formation. The empirical model given by Equation 18 is represented by the solid black lines in Figures 13c and d. Both on the linear and on the logarithmic axes, the data corresponds very well to this empirical model.

The reference circulation, Γ_0 (m^2/s), can be compared to the circulation theoretically produced by the synthetic jet, Γ_j, as given by Equation 4. The ratio Γ_0/Γ_j for all four cases is presented in Table 2. This ratio is approximately $\Gamma_0/\Gamma_j = 0.1$ for the three lowest Strouhal numbers, meaning that the measured circulation is significantly lower than the theoretically produced circulation. This low ratio can be explained by assuming that as vortices are being formed, circulation is already decaying. The empirical model for the decay is extrapolated in Figure 13d to illustrate the influence of decay during the formation period. Assuming a mean formation time for the circulation of $t = T/2$, i.e. half of the actuation cycle, Equation 18 indicates a circulation of $\Gamma(T/2)/\Gamma_0 = 9$. Using this new reference circulation, the ratio of measured versus expected circulation ($\Gamma(T/2)/\Gamma_j$) as presented in Table 2 is much closer to one (for the lower three Strouhal numbers).

For an increase in Strouhal number, most notably the highest Strouhal number of $St_H = 1.98$, Table 2 shows a strong decrease in the ratio of expected versus theoretically produced circulation. This decrease is likely caused by circulation cancellation due to close proximity of vortices to each other or ingestion of circulation due to close proximity of the vortices to the actuator when the suction phase starts. The latter is analogue to the formation criterion as defined by Holman et al. (2005), where for Strouhal numbers above the formation criterion no synthetic jet is formed due to ingestion of ejected fluid.

3.6 Scaling parameters

With the time-evolution of both the vortex circulation and location known, the decay of circulation as presented in Figure 8b can be properly scaled. Since both Γ/Γ_0 (see

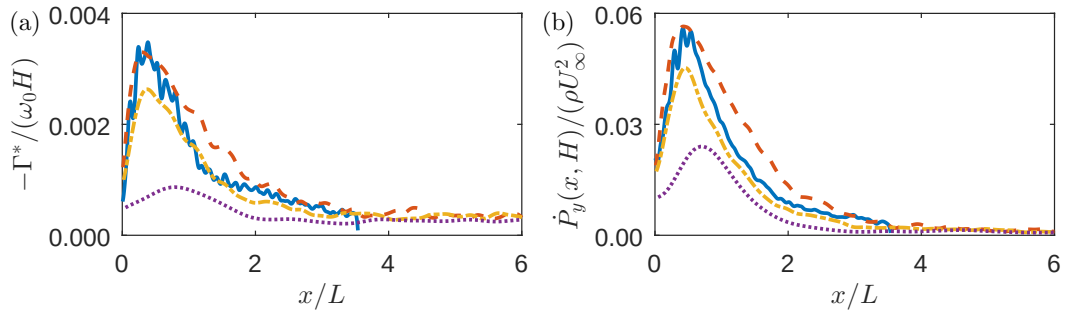

Figure 14: Time-averaged circulation per unit length in streamwise direction (a) and vertical momentum flux through the line $y/H = 1$ (b) as functions of x/L. $St_H = 0.21$ (—), $St_H = 0.48$ (– –), $St_H = 0.85$ (–··–) and $St_H = 1.98$ (···) (colour online).

Figure 13c) and x/L (see Figure 12c) are functions of t/T only, they can be rewritten to be functions of each other, i.e. $\Gamma/\Gamma_0 = f(x/L)$. Given the similarity between circulation and vertical momentum flux as presented in Figure 9, it may be assumed that vertical momentum flux is a function of x/L as well. The time-averaged circulation per unit length in streamwise direction and the momentum flux through the line $y/H = 1$ as presented in Figures 6b and 8b are replotted with the horizontal axis normalized as x/L in Figure 14. These graphs show that (apart from the highest frequency which has lower circulation as discussed above) the cases collapse well when the horizontal location is normalized as x/L. It is the decay of the (normalized) circulation with frequency in Equation 18 that causes the scaling of circulation with x/L. Given the connection between circulation and vertical momentum flux as presented in Figure 9 it can be assumed this decay of circulation with frequency also causes the scaling of vertical momentum flux with x/L and therefore the decrease in entrainment of momentum for increasing frequencies. The scaling does not only hold for the decay part on which it is based, but also for the formation part of the vortices. This indicates that for lower Strouhal numbers the formation will be completed at a location further downstream, meaning that the created shear layers take a longer streamwise distance to roll up into vortices. This implies that there is a lower limit on the Strouhal number, below which vortices will be formed at the end of (or beyond) the recirculation region and entrainment of momentum into the recirculation region will be minimal. This leads to the effect of forcing on the reattachment length diminishing for low Strouhal numbers as is observed in the literature (Kiya et al., 1993; Chun and Sung, 1996).

3.7 Reconsideration of forcing regimes

In the literature, frequency (Strouhal number) regimes of forcing are usually discussed in terms of low or high, where the low-frequency regime corresponds to shear-layer amplification whereas high-frequency corresponds to shear-layer stabilization. Using

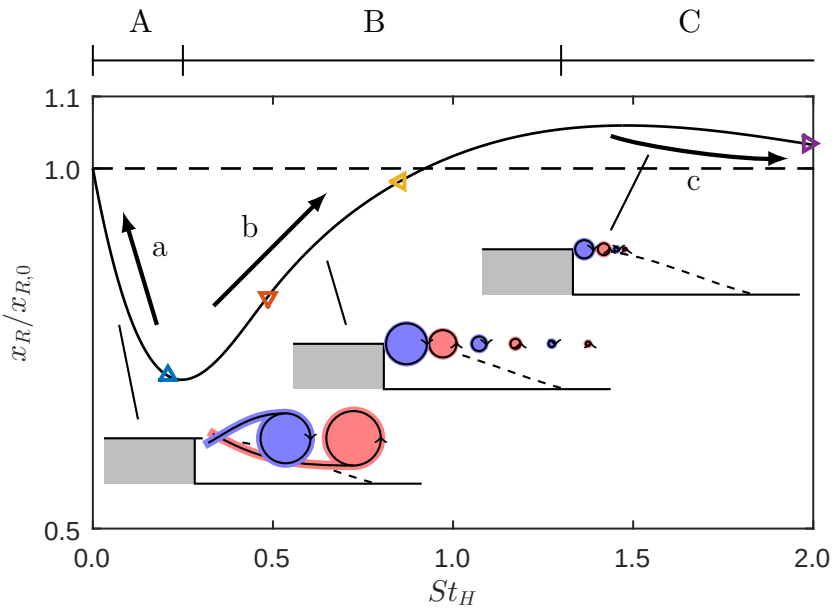

Figure 15: Reattachment length as a function of Strouhal number. The black line indicates the trend found in literature. Symbols represent cases from the present study (note that the trend-line is adapted to these cases). Regimes A, B and C are defined in the text.

combined insights from literature and the present study, the influence of the forcing frequency on the reattachment length could be explained differently.

The reattachment length is presented as a function of Strouhal number in Figure 15. The symbols correspond to the cases in the present study and are overlaid on the trend-line from literature discussed in Section 1. Note that this trend is adapted to fit the data. Using the results from literature and the present study, three regimes can be defined in this graph. Schematic representations of vortical structures are embedded for regimes A, B and C.

In regime A, corresponding to low Strouhal numbers, the effect on the reattachment length decreases for decreasing Strouhal numbers. In this regime the roll-up of vortices, scaling with $1/f$ takes a relatively long time and is completed at a point far downstream compared to the recirculation region. As discussed above, this will lead to less entrainment of momentum into the recirculation region. This is visible in Figure 15 by the effect on the recirculation region decreasing for a decreasing Strouhal number in regime A (in the direction of arrow a).

In regime B, for moderate Strouhal numbers, a train of vortices is formed. The circulation, entrainment of momentum and reattachment length are dominated by the decay of circulation with $\Gamma(t) \propto (tf)^{-2}$ as given by Equation 18 and discussed above. This results in the circulation decaying more rapidly for higher frequencies, resulting in

lower entrainment of momentum and an increase in reattachment length with Strouhal number as visible in regime B in Figure 15 (in the direction of arrow b). The increasing reattachment length has the ability to overshoot the unforced length. It is shown by Dandois et al. (2007) that this is caused by the synthetic jet decreasing the amplitude of incoming perturbations, thereby lowering entrainment of momentum and increasing the reattachment length.

In regime C, corresponding to high Strouhal numbers, the created vortices are very close to each other and close to the actuator during the suction phase. This leads to vorticity cancellation and re-ingestion into the actuator, meaning that the vortices contain relatively less circulation. This implies that the strength of the synthetic jet decreases with Strouhal number in this regime, analogue to the formation criterion (Holman et al., 2005). The decrease in strength leads to a decrease in the effect on the reattachment length as is visible for increasing Strouhal numbers in regime C in Figure 15 (in the direction of arrow c). Following the literature, it is assumed that the reattachment length stabilises at the unforced length ($x_R = x_{R,0}$) for high Strouhal numbers (Kiya et al., 1993).

4 Conclusions

The flow over a backward facing step is forced using a synthetic jet at the edge of the step. The effect of the forcing Strouhal number on the reattachment length behind the step is studied experimentally. Across all four studied cases, the reattachment length decreases linearly for increasing entrainment of momentum into the recirculation region. It is shown that entrainment is driven by vortices created by the forcing. The formation and evolution of these vortices depends on the Strouhal number. Three Strouhal number regimes have been identified. For low Strouhal numbers, associated with large time and length scales, the formation of vortices occurs at a relatively far downstream location in the flow. This minimizes the interaction between formed vortices and the recirculation region. For high Strouhal numbers, associated with small length scales, vortices of opposite orientation are spaced closely together, leading to cancellation of vorticity. Furthermore, in this regime, vortices created by the synthetic jet have not travelled far enough downstream by the time the suction period of the jet starts, leading to ingestion of vorticity. Both effects lead to a reduction of circulation and therewith a reduced effect of the forcing. In the regime associated with intermediate Strouhal numbers a train of alternating vortices is formed that entrains momentum into the recirculation region. The location and circulation of vortices is tracked using phase-locked PIV data. The convection velocity of the vortices can be described using an analytical model based on the impulse of the cross-flow accelerating the vortices. The decay of vortex circulation in time is described by an empirical model showing a decay of circulation with $(tf)^{-2}$. These models reveal the proper scaling factors (x/L and t/T) for the trajectories and circulation. Using these scaling factors, the data for all four cases collapses. The derived

scaling explains why the total circulation decreases for an increasing Strouhal number, leading to a decrease in entrainment of momentum and an increase in reattachment length. Because of a decrease in entrainment of momentum for high Strouhal numbers, combined with an amplitude reduction of incoming perturbations, forcing has the ability to increase the reattachment length compared to the unforced case.

Paper 3

Trajectory of a synthetic jet issuing into high Reynolds number turbulent boundary layers

Tim Berk[1], Nicholas Hutchins[2], Ivan Marusic[2] and Bharathram Ganapathisubramani[1]

[1]Aerodynamics and Flight Mechanics Research Group, University of Southampton, Southampton SO17 1BJ, UK

[2]Department of Mechanical Engineering, The University of Melbourne, Victoria 3010, Australia

Submitted for review to the Journal of Fluid Mechanics at 13/11/2017

Synthetic jets are zero-net-mass-flux actuators that can be used in a range of flow control applications. For many cross-flow applications the variation of the jet trajectory with the incoming boundary layer plays a crucial role. This trajectory provides an indication of the penetration depth of the synthetic jet into the boundary layer. In this paper we experimentally study trajectories of a synthetic jet in turbulent boundary layers for a range of actuation parameters in both low- and high Reynolds numbers (up to $Re_\tau = 12\,800$). The important parameters influencing the trajectory are determined from these measurements. The critical parameters are found to be the Strouhal number of the jet based on jet dimensions as well as the velocity ratio of the jet (defined as a ratio between the mean jet blowing velocity and the free-stream velocity). The Reynolds number of the boundary layer is shown to only have a small effect on the trajectory. An expression for the trajectory of the synthetic jet is derived from the data, which (in the limit) is consistent with known expressions for the trajectory of a steady jet in a cross-flow.

1 Introduction

Synthetic jets have attracted a considerable amount of interest over the past two decades (e.g. Smith and Glezer (1998); Glezer and Amitay (2002); Cattafesta and Sheplak (2011); O'Farrell and Dabiri (2014)). Experimental, numerical and theoretical studies have focused on the development of synthetic jet actuators, on the formation and evolution of synthetic jets and on flow control applications. A typical synthetic jet actuator is driven by a diaphragm such as a piezoelectric disc or a loudspeaker. An oscillatory motion of the diaphragm causes pressure fluctuations in the attached cavity. These pressure fluctuations create an oscillatory flow through an orifice. The distinctive feature of synthetic jets is that this flow is formed completely from the working fluid, meaning that no fluid supply is required. This creates a flow with zero-net-mass-flux, which has non-zero streamwise momentum. The lack of external fluid supply enables integration of synthetic jet actuators into complex geometries, making them attractive actuators

for flow control. Applications of synthetic jets, such as separation control (Dandois et al., 2007), turbulent boundary layer control (Rathnasingham and Breuer, 2003; Canton et al., 2016) and virtual aeroshaping (Mittal and Rampunggoon, 2002) often involve a synthetic jet issuing into a cross flow. For some of these applications the trajectory of the jet is important.

The trajectory of continuous jets has been widely studied in the literature as reviewed by Mahesh (2013). The trajectory of a jet in cross flow is usually described using a power-law of the form

$$\frac{y/D}{r^c} = B\left(\frac{x/D}{r^c}\right)^n, \tag{1}$$

where y is the wall-normal location, x is the streamwise location, r is the velocity ratio, given by the ratio of the jet velocity to the free-stream velocity $\bar{u}/U_\infty$, D is the relevant orifice dimension (usually the diameter for circular jets) and B, n and c are constants. A comparison by Mahesh (2013), considering different studies, shows that trajectories do not fully collapse when normalized by rD, indicating that B, n and c are not constant. In fact, a range is reported of $1.2 < B < 2.6$, $0.28 < n < 0.34$ and $0 < c < 2$ (Mahesh, 2013).

The trajectory of a synthetic jet in cross flow may also be described using a power law (Smith, 2002). However, Equation 1 depends on variations in jet velocity only, whereas a synthetic jet is described by a velocity and a frequency (Glezer and Amitay, 2002).

M'Closkey et al. (2002) investigated sinusoidal forcing of a continuous jet in cross flow. The forcing amplitude is smaller than the mean jet velocity, meaning that the jet velocity remains positive throughout the cycle. From smoke visualisations presented in their work the jet trajectory can be qualitatively identified. While keeping the blowing ratio fixed at $r = 2.6$, a forcing frequency of $f = 74$ Hz causes the jet to penetrate deeper into the cross flow compared to a steady jet.

The effect of frequency is further evidenced by Shuster et al. (2005). Instantaneous contour maps of spanwise vorticity qualitatively show the trajectory of the jet. The frequency of their jet is doubled while keeping the velocity ratio fixed at $r = 1.1$. This increase in frequency leads to a significant reduction of the penetration depth.

These studies, in which the trajectory of the jet changed with frequency for a fixed blowing ratio, show that Equation 1 does not hold for synthetic jets. Assuming that a universal power-law with constant coefficients B and n exists for jet trajectories, the denominator must be dependent on the frequency.

Jabbal and Zhong (2010) showed that the trajectory of synthetic jets in a cross flow depends on the type of vortical structures created by the jet (e.g. hairpin vortices or vortex rings). Earlier work (Jabbal and Zhong, 2008) had shown that this structure type depends on both the velocity ratio and the non-dimensional frequency of the jet. However, a classification map by Sau and Mahesh (2008) shows that for $r < 2$ the interaction between a jet and a cross flow creates hairpin vortices. Note that these

studies consider the interaction of a synthetic jet with a laminar boundary layer which may be different from the interaction with a turbulent boundary layer.

In addition to changes in velocity ratio and frequency, Van Buren et al. (2016b) showed that both the geometry of the jet and its orientation with the flow also influences the trajectory. A synthetic jet actuator with a rectangular orifice of aspect ratio $AR = 18$ was placed in a cross flow with the long dimension of the slot either aligned in spanwise- or in streamwise direction. They show that this has a significant effect on both the type of structures created by the jet and on the trajectory. This indicates that the relevant orifice dimension D in Equation 1 – which usually represents the diameter of a circular orifice – for a rectangular orifice depends on the orientation of the orifice compared to the flow. The equivalent diameter of a non-circular orifice (the diameter of a circular orifice of identical cross-sectional area) has been shown to be the relevant dimension for the formation of vortex rings in quiescent flow (O'Farrell and Dabiri, 2014). However, the dependency on orientation as mentioned above rules out a relevant dimension D based only on this equivalent diameter (which does not change with orientation).

Another candidate for the relevant dimension could be the length of the slot in streamwise direction. However, this dimension is independent of the aspect ratio of the slot, which has been shown to be an important parameter for vortex formation (Van Buren et al., 2014a). Moreover, the streamwise length l of a slot is the same as the streamwise length of a circular orifice with diameter l, while these have been shown to have a very different influence on the flow field (Kim et al., 2012). Regardless of the configuration, it is clear that there should be a relevant orifice dimension D for a given configuration. This dimension could depend on the slot width d, slot length l and orientation of the orifice compared to the cross flow. The nature of D is outside the scope of this current study and as we use only a single configuration. An arbitrary value of $D = 1$ m is used in this study where quantification is required.

The present study investigates the trajectory of a rectangular synthetic jet issuing into turbulent boundary layers. The turbulent boundary layers are characterized using the free-stream velocity U_∞, the boundary-layer thickness δ, the kinematic viscosity ν and the skin-friction velocity U_τ. It should be noted that the friction velocity is directly related to the free-stream velocity through the skin-friction coefficient $c_f = 2U_\tau^2/U_\infty^2$, which is a function of $\log(Re_x)$. Therefore, it is not varied independently in the present study. The governing non-dimensional parameter for the boundary layer is assumed to be the friction Reynolds number,

$$Re_\tau = U_\tau \delta / \nu. \tag{2}$$

The synthetic jet is characterized by the width d and length l of the orifice as well as the frequency f, mean blowing velocity $\bar{u}$ and kinematic viscosity ν. The geometry of the rectangular orifice is kept constant in the present study and can be described by the

aspect ratio,

$$AR = l/d. \tag{3}$$

Analogous to a steady jet in cross flow as discussed above, it is hypothesised that the trajectory of a synthetic jet can also be described by a power law of the form

$$\frac{y/D}{g(\dots)} = A\left(\frac{x/D}{g(\dots)}\right)^n, \tag{4}$$

where $g(\dots)$ represents a non-dimensional scaling factor depending on jet and cross-flow parameters.

For steady jets (Equation 1) $g(\dots)$ equals the velocity ratio to the power c,

$$g(\dots) = r^c = (\bar{u}/U_\infty)^c. \tag{5}$$

It is hypothesized that issuing a jet into a turbulent boundary layer (as opposed to a laminar cross flow in most studies) will add an influence of Re_τ on $g(\dots)$. As discussed above, issuing a synthetic jet instead of a steady jet into a cross flow will also add an influence of the frequency. The correct non-dimensional form for this frequency is unknown. Three scalings are hypothesized for this frequency. These are the outer- and inner units of the boundary layer or a passing frequency of the cross flow over the jet, i.e.

$$f_1^* = f\delta/U_\infty, \tag{6}$$

$$f_2^* = f\nu/U_\tau^2, \tag{7}$$

$$f_3^* = fD/U_\infty. \tag{8}$$

The purpose of the present study is to identify the scaling of the trajectory as in Equation 4, including the suitable non-dimensional jet frequency.

2 Experimental set-up and procedures

2.1 Description of the actuator

The actuator is driven by a Visaton SC 8 N loudspeaker, actuated with a sinusoidal velocity signal. This speaker has a frequency response of 70–20 000 Hz with a resonance frequency around 90 Hz. This speaker is attached to a circular (pancake shaped) cavity of volume 1.85×10^{-5} m^3 and a nozzle with a neck length of 19.5 mm. The slot length and width are kept constant throughout the experiments, $l = 13$ mm and $d = 1$ mm ($AR = 13$). In absence of a cross flow, this combination of cavity and nozzle leads to a fluidic (Helmholtz) resonance frequency of 550 Hz as determined from exit velocity

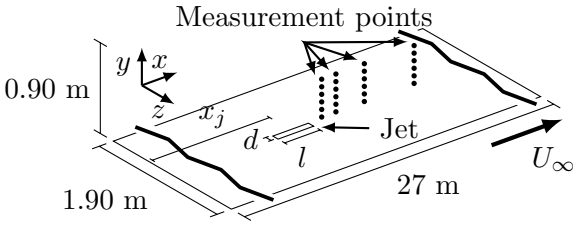

Figure 1: Schematic of set-up, indicating slot position and orientation as well as measurement locations and relevant parameters (not to scale).

measurements. The long-dimension of the slot (l) is aligned with the flow as presented schematically in Figure 1. Details on the jet calibration are given in §2.3.

2.2 Description of the facility

Experiments are performed in the high-Reynold-number boundary-layer wind tunnel (HRNBLWT) at the University of Melbourne. This open-return blower wind tunnel has a 27 m long test section, enabling Reynolds numbers up to $Re_\tau = 25\,000$. The test section has a spanwise width of 1.9 m and wall-normal height of 0.9 m, meaning that the influence of the side-walls and ceiling on the trajectory of the jet can be neglected. See Figure 1 for a schematic of the set-up. The local boundary-layer thickness is a function of both the free-stream velocity and the downstream distance from the boundary-layer trip at the test-section inlet. By varying the downstream location of the actuator (x_j), the boundary-layer thickness can be varied independently from the free-stream velocity. The friction velocity U_τ cannot be controlled independently and is a function of mainly the free-stream velocity (U_∞) and streamwise location (x_j). Experimental parameters were intentionally varied from case to case and are listed in §3. Further details on the facility can be found in Nickels et al. (2005).

Velocity measurements are performed using a single-wire traversing hot-wire probe, operated in constant-temperature mode with an overheat ratio of 1.7. The physical length of the wire was kept constant at 0.5 mm, with a length-to-diameter ratio of 200. This implies that the viscous scaled length of the wire l^+ varied throughout the different cases. For all cases $l^+ < 25$, causing at worst a limited attenuation of the energy spectra for the small scales (Hutchins et al., 2009) which does not influence the results in the present paper. Wall-normal traverses are taken at multiple streamwise distances directly behind the jet by traversing from the wall upwards. The initial wall-normal position is determined using a digital microscope. The estimated uncertainty in this wall-normal position is $\epsilon_{y_0} < 0.1$ mm. The probe is traversed using an encoder with a precision of an order of magnitude higher, implying that the uncertainty in wall-normal position is fully determined by the uncertainty of the initial position (i.e. $\epsilon_y < 0.1$ mm).

The boundary-layer thickness δ and skin-friction velocity U_τ are determined from the unperturbed flow using the composite velocity profile fit of Chauhan et al. (2009). This

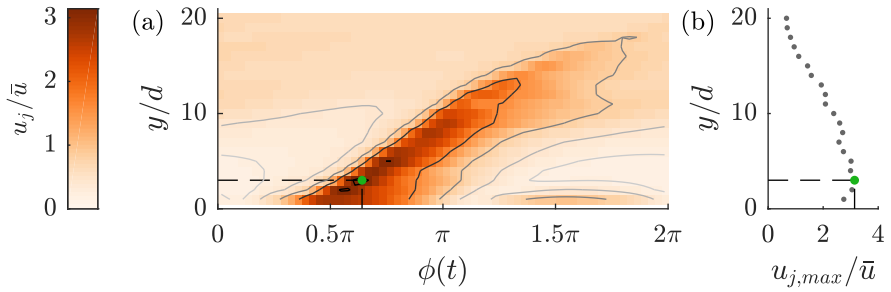

Figure 2: (a) Phase-locked jet-centreline velocity over 64 phases as function of wall-normal distance for case 1 as defined in Table 1 (in absence of cross flow). (b) Variation of the maximum centreline velocity with wall-normal height. The wall-normal location and phase at which $u_{j,max}$ occurs are indicated by the green dot.

fit is also used to obtain an accurate value for the offset in wall-normal position.

2.3 Determining the jet velocity

The mean blowing velocity in absence of the cross flow is used as the relevant jet velocity. For a sinusoidal signal the mean blowing velocity is given by $\bar{u} = u_{j,max}/\pi$. The phase-averaged centreline velocity of the jet for a single case is presented for different distances to the jet in Figure 2. It can be seen that the maximum velocity occurs a small distance away from the orifice exit plane ($y = 3$ mm for this specific case), which can be attributed to the formation of the vortex ring created by the jet (Smith and Glezer, 1998). This true maximum velocity rather than the value at the orifice exit is used to calculate the mean blowing velocity.

2.4 Determining the jet location

Multiple definitions can be used to identify the location of a jet, including positions of local maxima in the velocity deficit, local vorticity maxima or the time-averaged streamline originating from the orifice (Mahesh, 2013). Neither vorticity or streamlines can be determined from only the velocity magnitude. Identification of local maxima in the velocity deficit requires comparison of a perturbed to an unperturbed case, thereby increasing the uncertainty. Here we consider the location of the jet based on a single data set by decomposing the velocity signal as,

$$u(y,t) = \tilde{U}(y) + \tilde{u}(y,\phi(t)) + u'(y,t), \tag{9}$$

where $\tilde{U}(y)$ is the time-averaged local velocity, $\tilde{u}(y,\phi(t))$ is the phase-averaged local velocity at phase $\phi(t)$ and $u'(y,t)$ are the local (turbulent) velocity fluctuations (similar to Hussain and Reynolds (1970)). A contour map of the phase-averaged component $\tilde{u}$ as function of phase $\phi(t)$ and wall-normal location y^+ is presented in Figure 3a. A clear maximum of variations in phase can be identified at a wall-normal position indicated

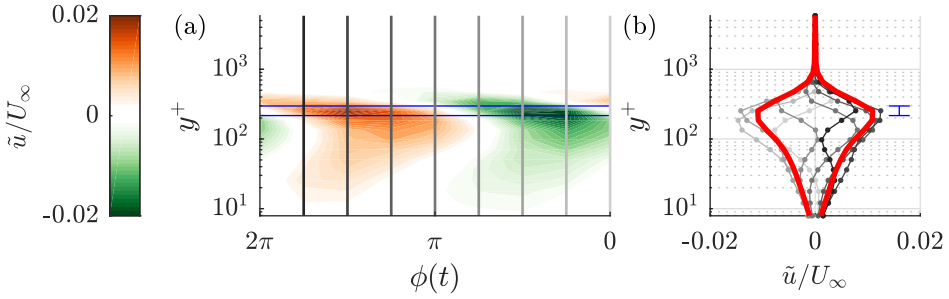

Figure 3: (a) Contour map of the phase-averaged local velocity $\tilde{u}$ with wall-normal distance and phase. (b) Line plot of $\tilde{u}$ where the line colour corresponds to colours of vertical lines in (a). The red lines indicate the root-mean-square over the eight phases, the blue lines indicate the location of the maximum.

by the horizontal blue lines. The velocity at the phases indicated by the vertical lines is presented in Figure 3b, where the root-mean-square value is indicated by the thick red lines. The location of the jet is defined as the location where this rms-value reaches its maximum. This location can be determined with an accuracy of one measurement point as indicated by the blue error bar.

3 Results

As discussed above, it is assumed that the trajectory of a synthetic jet issuing into a turbulent boundary layer scales with the Reynolds number (Re_τ), velocity ratio (r) and some measure of frequency. The relevant non-dimensional group containing the jet frequency is unknown and could be any of the three groupings listed in Equations 6–8. In an exploratory study these parameters are varied systematically to determine both the relevant normalisation of the frequency as well as the scaling of the trajectory as a function of this determined frequency, Re_τ and r. Using these results a validation study is performed in which the most important non-dimensional groups are varied systematically.

3.1 Exploratory study

Jet- and cross-flow parameters are varied systematically as listed in Table 1. The first group of cases (1–4) considers a variation in Re_τ while keeping the velocity ratio constant and (roughly) matching the outer-scaled frequency ($f\delta/U_\infty$) between cases. For the second group (5–8) the Reynolds number is varied for a constant blowing ratio while (roughly) matching the inner-scaled frequency ($f\nu/U_\tau^2$). The third group (9–12) considers variations in blowing ratio while matching either inner- or outer-scaled frequencies or matching the blowing ratio and Reynolds number for a variation in frequency (cases 10 and 12). The passing frequency of the jet (fD/U_∞) is not matched systematically but varied/matched as a result of the others.

Table 1: Summary of case parameters for the exploratory study. Symbols indicate symbols used in Figure 4. The arbitrary value $D = 1$ m is used to quantify fD/U_∞.

	#	x_j (m)	U_∞ (m/s)	δ (m)	$\bar{u}$ (m/s)	f (1/s)	Re_τ	r	$f\delta/U_\infty$	$f\nu/U_\tau^2$	fD/U_∞	
Fix. r, f_1^* Var. Re_τ	1	8	10	0.139	3.0	130	3200	0.3	1.8	0.016	13.0	▲
	2	8	22	0.132	6.6	300	6350	0.3	1.8	0.008	13.6	▷
	3	20	10	0.296	3.0	62	6350	0.3	1.8	0.009	6.2	◁
	4	20	25	0.254	7.5	169	12800	0.3	2.3	0.004	6.8	▼
Fix. r, f_2^* Var. Re_τ	5	8	10	0.139	3.0	69	3200	0.3	1.0	0.009	6.9	□
	6	8	22	0.132	6.6	300	6350	0.3	1.8	0.008	13.6	▷
	7	20	10	0.296	3.0	62	6350	0.3	1.8	0.009	6.2	◁
	8	20	25	0.254	7.5	404	12800	0.3	4.1	0.010	16.2	○
Var. r, f	9	8	10	0.139	6.0	130	3200	0.6	1.8	0.016	13.0	×
	10	8	10	0.139	9.0	130	3200	0.9	1.8	0.016	13.0	×
	11	8	22	0.132	9.9	300	6350	0.45	1.8	0.008	13.6	+
	12	8	10	0.139	9.0	390	3200	0.9	5.4	0.049	39.0	△

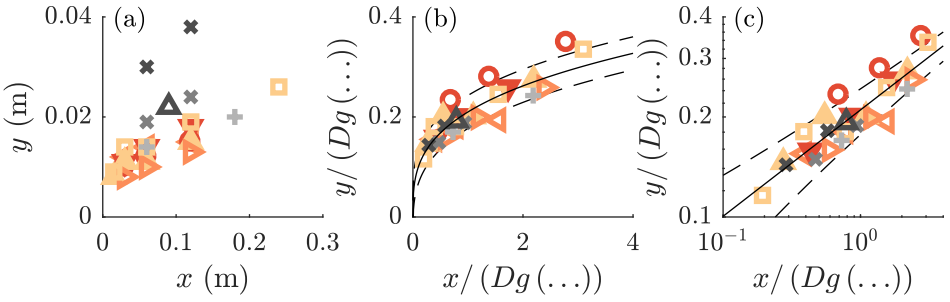

Figure 4: (a) Trajectories for all cases listed in Table 1. (b) Trajectories optimally scaled using the scaling factors in Table 2. (c) Equal to (b) but with logarithmic axes. Solid lines indicate the fitted trajectory, dashed lines indicate the fit ± the rms of the residuals..

For each case the wall-normal location of the jet is determined at multiple positions downstream of the slot. The measured jet locations are presented in Figure 4a with symbols corresponding to symbols in Table 1. As expected the trajectories show some wall-normal variation with especially the cases of higher velocity ratio (×, × and △) standing out.

The influence of the non-dimensional groups (r, Re_τ and f^*) on the trajectory given by Equation 4 is quantified by assuming $g(\dots) = r^{c_1} Re_\tau^{c_2} f^{*c_3}$ (for f_1^*, f_2^* and f_3^* independently). The coefficients A, n and c_{1-3} are fitted using nonlinear regression. The accuracy of each fit is measured as the root-mean-square of the residuals, i.e.

$$\epsilon = \mathrm{rms}\left(y - Ax^n g(\dots)^{1-n}\right). \tag{10}$$

Fitting parameters and accuracy are listed in Table 2. Fits are compared to an un-scaled

Table 2: Fitted coefficients and residuals for $y/\left(Dg(\dots)\right) = A\left(x/\left(Dg(\dots)\right)\right)^n$

$g(r^{c_1}Re_\tau^{c_2}f^{*c_3})$	A	n	c_1	c_2	c_3	ϵ (mm)
1	0.04	0.38	0	0	0	5.4
r^c	0.07	0.34	0.95	0	0	2.8
$r^{c_1}Re_\tau^{c_2}f_1^{*c_3}$	0.04	0.30	1.15	-0.53	0.13	1.9
$r^{c_1}Re_\tau^{c_2}f_2^{*c_3}$	0.30	0.32	0.91	-0.20	-0.37	2.4
$r^{c_1}Re_\tau^{c_2}f_3^{*c_3}$	0.26	0.32	1.26	-0.04	-0.56	1.6

power law ($g\left(\dots\right) = 1$) and to scaling based on the velocity ratio only as in Equation 1 ($g\left(\dots\right) = r^c$).

Based on the residuals, proper normalisation of the frequency is as fD/U_∞ ($\epsilon = 1.6$ mm). The root-mean-square of the residuals using this scaling is almost twice as small as for the velocity-ratio scaling ($\epsilon = 2.8$ mm) and almost four times as small as for the unscaled case ($\epsilon = 5.4$ mm). It should be noted that the residuals using the outer-scaled frequency are only slightly higher (20%) than when using the passing frequency. The difference between these normalisations is caused in this case (where D is constant) by δ which is only varied by a factor two for the current experiments, explaining the small difference between the residuals.

The fit using the passing frequency shows a scaling of

$$g\left(\dots\right) = r^{1.26}Re_\tau^{-0.04}\left(fD/U_\infty\right)^{-0.56}. \tag{11}$$

Measured trajectories are scaled using this expression in Figures 4b and c, showing a reasonable collapse for all cases.

This result suggests that (I) the trajectory scales with $r^{1.26}$ which is equal to the scaling for a steady jet, (II) even over the large range of Reynolds numbers tested here ($3200 < Re_\tau < 12\,800$) Re_τ only has a small effect on the trajectory and (III) scaling of the frequency of the jet is with the passing frequency of the flow over the orifice, fD/U_∞.

3.2 Validation study

A second experiment is designed as validation of the leading terms (r and fD/U_∞) in Equation 11. In this experiment Re_τ is kept constant while r and fD/U_∞ are varied systematically as listed in Table 3.

Measured wall-normal locations of the jet for the validation study are presented in Figure 5a. Fitted values for the power law are $A = 0.27$ and $n = 0.26$, which are slightly different from the values for the initial experiment ($A = 0.26$, $n = 0.32$). Nevertheless, the normalized data in Figures 5b and c collapses onto a single power law (indicated by the black line), validating the scaling as listed in Equation 11.

Table 3: Summary of case parameters for the validation study. Symbols indicate symbols used in Figure 5. The arbitrary value $D = 1$ m is used to quantify fD/U_∞.

#	x_j	U_∞	δ	$\bar{u}$	f	Re_τ	r	fD/U_∞	
13	20	10	0.296	4.5	62	6350	0.45	0.16	◁
14	20	10	0.296	3.0	140	6350	0.3	0.07	○
15	20	10	0.296	4.5	140	6350	0.45	0.07	○
16	20	10	0.296	6.75	140	6350	0.675	0.07	○
17	20	10	0.296	4.5	314	6350	0.45	0.03	□
18	20	10	0.296	6.75	314	6350	0.675	0.03	□

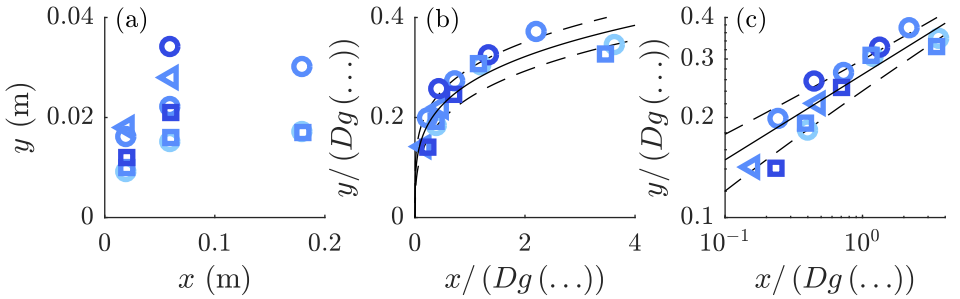

Figure 5: (a) Trajectories for all cases listed in Table 3. (b,c) Trajectories scaled using Equation 11. Solid lines indicate the fitted trajectory ($A = 0.27$, $n = 0.26$), dashed lines indicate the fit $\pm$ the rms of the residuals..

4 Discussion

The derived scaling for the trajectory of a synthetic jet issuing into a turbulent boundary layer as stated in Equation 11 depends on three non-dimensional groups.

Analogous to steady jets, the trajectory scales with the velocity ratio as $y/r^c \propto (x/r^c)^n$. As discussed above, for steady jets usually a value of $c = 1$ is stated, but in general $0 < c < 2$. The value found for synthetic jets, $c = 1.26$, is well within this range, showing analogy in the effect of the velocity ratio on trajectories of steady jets and synthetic jets.

The friction Reynolds number is found to only have a small influence on the trajectory of the jet, scaling as $y/Re_\tau^{-0.04} \propto \left(x/Re_\tau^{-0.04}\right)^n$. This coefficient may be considered to be within experimental uncertainty. Therefore, the trajectory of the jet in the cross flow is at best weakly dependent on the Reynolds number of the boundary layer and is most likely to be independent of it. This suggests that further studies can be performed in other facilities which do not have the capability of reaching high Reynolds numbers. It should be noted that U_τ may have an additional influence on the trajectory which could not be independently measured due to the dependence of C_f on Re_τ.

It is found that the trajectory scales with the term fD/U_∞, where D is a representative slot dimension added from dimensional arguments. The exact nature of D can only be determined by varying the slot dimensions, which was outside the scope of the parametric

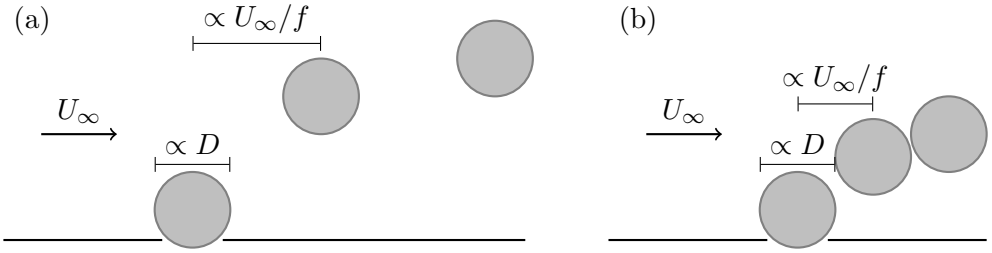

Figure 6: Schematic indicating the physical meaning of the non-dimensional group fD/U_∞ which is considered as the ratio between length scales U_∞/f, representing the streamwise distance between subsequent pulses of the jet and D, representing the size of these pulses. (a) A case with $fD/U_\infty << 1$ and (b) the case $fD/U_\infty = 1$, showing an almost continuous jet.

study in the performed experiments, but it is assumed that D is a function of both the slot width d and length l. The term fD/U_∞ represents a ratio between two length scales, where U_∞/f is related to the separation distance between subsequent jet pulses created at time interval $1/f$ and with streamwise advection velocity $\propto U_\infty$. These length scales are schematically represented in Figure 6a, where it is assumed that the size of jet pulses/vortical structures depends on the representative size of the orifice D. As presented in Figure 6b, when increasing this ratio an interesting phenomenon occurs near unity where the pulses of the jet form a seemingly continuous jet. At the same time when $fD/U_\infty = 1$ (and neglecting the influence of $Re_\tau^{-0.04}$) the scaling factor in Equation 11 is given by $g(\dots) = r^{1.26}$, recovering the scaling for a continuous jet.

Following the above arguments, the empirical scaling derived in this study can be considered to be "universal" for pulsed jets and forced continuous jets.

5 Conclusions

Scaling of the trajectory of a synthetic jet issuing into a turbulent boundary layer is derived. This problem can be described by the slot length l and width d, the jet frequency f and mean blowing velocity $\bar{u}$, the free-stream velocity U_∞, the boundary-layer thickness δ, the friction velocity U_τ and the kinematic viscosity ν. Six independent non-dimensional groups can be formed out of these parameters. However, due to the nature of the experiment the aspect ratio of the jet $AR = l/d$ as well as the ratio U_∞/U_τ are fixed, leaving four independent non-dimensional groups to describe scaling of the trajectory of the jet. Fitting of trajectories for a wide parametric study showed that only three independent non-dimensional groups are required to describe these trajectories. The trajectories are shown to scale as

$$\frac{y/D}{r^{1.26}Re_\tau^{-0.04}\left(fD/U_\infty\right)^{-0.56}} = A\left(\frac{x/D}{r^{1.26}Re_\tau^{-0.04}\left(fD/U_\infty\right)^{-0.56}}\right)^n,$$

where the scaling factors in the denominator are given by:

(i) $r^{1.26}$, showing analogy to trajectories of steady jet in cross flow which scales with r^c for typical values of $0 < c < 2$.

(ii) $Re_\tau^{-0.04}$, indicating only a weak dependence on the friction Reynolds number. This enables future studies in facilities with lower Reynolds numbers.

(iii) $(fD/U_\infty)^{-0.56}$, where D is an unknown combination of the slot dimensions l and d. This term indicates the relevant non-dimensional number for the jet frequency. This group gives the ratio between two length scales; U_∞/f, relating to the streamwise spacing between subsequent pulses and D, relating to the size of these pulses. It can be argued that when the separation between pulses equals the pulse size a continuous jet is formed. At the same time, when this ratio goes to unity the scaling for the trajectory of a steady jet in cross flow is recovered. It may be assumed that the scaling derived in this study holds for pulsed and forced jets.

The nature of the relevant orifice dimension D and the relation to the pulse size as hypothesised above is a subject for further study.

Paper 4

Effects of vortex-induced velocity on the wake of a synthetic jet issuing into a turbulent boundary layer

Tim Berk and Bharathram Ganapathisubramani

Aerodynamics and Flight Mechanics Research Group, University of Southampton, Southampton SO17 1BJ, UK

Manuscript under preparation

A synthetic jet issuing into a cross flow influences the velocity of the cross flow. At the jet exit the jet has a wall-normal velocity, while the cross flow has a streamwise velocity. This difference in velocity leads to a momentum transfer between the jet and the cross flow. At some point downstream (the end of the near-field) the pulses created by the jet have the same velocity as the surrounding flow, meaning that the jet is no longer blocking the cross flow. However, the velocity field in this regime is not equal to the inflow velocity of the cross flow. In fact, the jet is creating a momentum-flux deficit in the cross flow far downstream of the viscous near-field of the jet. In the literature this momentum-flux deficit is often attributed to viscous blockage or to up-wash of low-momentum fluid. The present paper proposes and quantifies a third source of momentum deficit: a velocity induced opposite to the cross flow by the vortical structures created by the synthetic jet. These vortical structures are reconstructed from measured data and their induced velocity is calculated using Biot-Savart. The three-dimensional three-component induced velocity fields show great similarity to the measured velocity fields, suggesting that this induced velocity is the main contributor to the velocity field around the synthetic jet. Variations with Strouhal number (frequency of the jet) and velocity ratio (velocity of the jet) are observed and discussed. An inviscid-flow model is developed which predicts the evolution of a given vortical input structure. Using the measured data as an input, this model is able to predict the deformation, (wall-normal) evolution and qualitative velocity field of the jet. The present study presents evidence that the velocity induced by the vortical structures forming a synthetic jet plays an important role in the velocity field around the jet.

1 Introduction

Synthetic jets have attracted a considerable amount of research over the past decades (e.g. Smith and Glezer (1998); Glezer and Amitay (2002); Cattafesta and Sheplak (2011)). The distinctive feature of synthetic jet actuators is the creation of a zero-net-mass-flux jet which has non-zero net momentum flux. These jets consist of alternating blowing and suction cycles through an orifice and are formed entirely from the working

fluid. During the suction phase surrounding fluid is ingested into the actuator. The blowing phase is often modelled as a slug of fluid being ejected by the actuator. Part of this fluid slug rolls up into a vortical structure around the edge of the jet exit. This ejected fluid propagates away from the actuator, driven by a combination of its self-induced velocity and the momentum created by the jet. Since this jet is created from the working fluid, synthetic jet actuators do not require a fluid supply, making them practical to integrate in a range of flow-control applications. Synthetic jets in cross flow are widely used in applications such as mixing enhancement (M'Closkey et al., 2002; Sau and Mahesh, 2008), control of turbulence (Rathnasingham and Breuer, 2003) or separation control (Dandois et al., 2007). In the present study the interaction of a synthetic jet with a turbulent boundary layer is considered where the jet is issuing in the direction normal to the bulk flow (i.e. in wall-normal direction).

The interaction between the synthetic jet and the cross flow influences the flow in both the near-field and the far-field of the jet. The near-field can be defined as the region close to the jet exit where the blowing- and suction motions through the orifice are dominant and where viscous effects play a large role. During the suction part of the cycle fluid from the cross flow is ingested into the actuator, creating a negative wall-normal component. This fluid is ejected during the blowing part of the cycle. Initially the ejected fluid has zero momentum in the streamwise (relating to the cross flow) direction but non-zero momentum in the wall-normal direction. This means that the ejected fluid is blocking the cross flow, causing a momentum flux from the cross flow to the ejected fluid and creating a viscous blockage effect. In a similar fashion the wall-normal momentum is transferred to the surrounding cross flow which has negligible wall-normal momentum. These momentum fluxes will accelerate the ejected fluid in the direction of the cross flow and decelerate the wall-normal component. The far-field can then be defined as the region where the streamwise velocity of the ejected fluid is similar to the surrounding fluid and the wall-normal velocity created by the blowing of the jet is negligible.

However, this does not mean that the flow in the far-field is equal to the inflow upstream of the jet. In fact, the interaction of the jet with the cross flow causes a considerable momentum deficit in the flow, persisting far beyond the viscous near-field. For most applications minimization of this momentum deficit is of importance for the efficiency of the pursued goal. In order to minimize it, the origin of the momentum deficit needs to be understood. In the literature, the momentum deficit is generally referred to as blockage (see for example Lardeau and Leschziner (2011)), or as caused by vortex induced up-wash of low-momentum fluid near the wall (see for example Rathnasingham and Breuer (2003)). However, these were qualitative descriptions and do not quantify the momentum deficit in any detail. This paper proposes a third origin and quantifies its momentum deficit: a velocity induced by the created vortical structures in the direction opposite to the cross flow. Furthermore, it will be reasoned that the effects of blockage and up-wash on the momentum deficit are limited. The total momentum deficit will be a combination of these three (and possibly other) factors, i.e. viscous blockage of the cross

flow, vortex induced up-wash of low-momentum fluid and a vortex induced velocity in the direction opposite to the cross flow. The ratio of contributions of these effects will vary with downstream distance and depends on the flow parameters and the type of vortical structures created by the synthetic jet.

The periodic velocity cycle of a synthetic jet can be characterized using a frequency f and velocity magnitude $\bar{u}$ (Glezer and Amitay, 2002). The velocity magnitude used here is the mean blowing velocity, calculated as $\bar{u} = \frac{1}{T}\int_0^{T/2} u(t)\mathrm{d}t$. The velocity of the jet is normalized using the free-stream velocity, U_∞, resulting in a velocity ratio, given by

$$r = \frac{\bar{u}}{U_\infty}. \tag{1}$$

The frequency of the jet is normalized using the free-stream velocity in combination with the slot length l, resulting in a Strouhal number given by

$$St = \frac{fl}{U_\infty}. \tag{2}$$

The vortical structures created by a synthetic jet issuing into a laminar boundary layer have been mapped onto a parameter space by Sau and Mahesh (2008) and by Jabbal and Zhong (2008). For low velocity ratios the shear in the boundary layer is strong enough to fully cancel the vorticity of opposite sign on the upstream side of the vortex ring, modifying this ring to a hairpin-like structure. For higher velocity ratios partial cancellation of the upstream side of the vortex ring occurs. The resulting vortical structure has a self-induced velocity in the wall-normal direction, transporting the structure upwards while being convected downstream by the cross flow. Since the upstream side of the structure is (partially) cancelled by the shear in the boundary layer, the downstream side experiences a larger self-induced velocity, causing the structure to tilt against the cross flow. This results in a hairpin structure that is very similar to eddies observed in and/or modelled for turbulent boundary layers (see for example Perry and Chong (1982)). A notable difference is that the vortical structures created by the synthetic jet are of a periodical nature and reappear at the exact same spot each cycle whereas eddies in a turbulent boundary layer have a statistical distribution.

The influence of orifice geometry and orientation on the three-dimensional interaction of a synthetic jet with a cross flow has been studied by Van Buren et al. (2016a,b), who found large qualitative differences. The influence of orifice shape is beyond the scope of the present paper. However, the global (qualitative) conclusions as well as the outlined analysis method are assumed to be applicable to a wide range of orifice geometries.

The formed vortical structure is linked to all three origins of the momentum deficit introduced above; the fluid ejected by the synthetic jet forming this structure causes viscous blockage of the cross flow, the structure induces a velocity component in the wall-normal direction causing up-wash of low-momentum fluid and it induces a streamwise-velocity component in the direction opposite to the cross flow. The present paper focusses on the

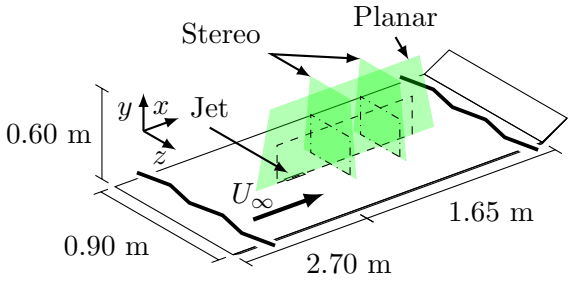

Figure 1: Schematic of experimental set-up (not to scale).

velocity induced by the vortical structure in streamwise direction. This induced velocity is calculated using Biot-Savart, similar to how contributions of eddies in the turbulent boundary layer are calculated (see for example recent work by de Silva et al. (2015) or Baidya et al. (2017)).

First, the measured momentum-flux deficit is presented in §3.1. Three different sources of momentum deficit are identified and discussed using these measurements. The measured vortical structures are reconstructed in §3.2.1 and their induced velocity is calculated in §3.2.2. This induced velocity is compared to the measured velocity deficit and the similarities/differences in the momentum-flux deficit for both cases is discussed. Using the measured vortical structures as an input, an inviscid-flow model is discussed in §3.3 which predicts the evolution of a train of these structures. This predictive model gives insight in the three-dimensional three-component velocity field as well as the deformation and evolution of the vortical structures.

2 Experimental set-up and procedures

2.1 Description of the flow and facility

Experiments are performed in the University of Southampton's 3 ft by 2 ft suction wind tunnel. The tunnel is fitted with a false floor, creating a test section of 4.35 m $\times$ 0.60 m $\times$ 0.90 m ($x \times y \times z$, as defined in Figure 1). Figure 1 presents a schematic of the experimental set-up. The elliptical leading edge of the floor is fitted with a boundary-layer trip. The angle of the trailing-edge flap is adjusted to ensure a zero-pressure-gradient turbulent boundary layer at the measurement location. The turbulent boundary layer has a free-stream velocity of $U_\infty = 10$ m/s and boundary-layer thickness of $\delta = 45$ mm ($Re_\tau = 1220$).

2.2 Description of the synthetic jet actuator

A synthetic jet with a rectangular orifice exit of dimensions $l = 13$ mm in x-direction and $d = 1$ mm in z-direction is used. The exit of the jet is flush with the boundary-layer

Table 1: Actuation parameters used for the different cases in the present study.

$\bar{u}$ (m/s)	8.8	8.8	8.8	8.8	4.5	1.35
f (Hz)	108	215	495	646	495	495
r	0.88	0.88	0.88	0.88	0.45	1.35
St	0.1	0.3	0.7	0.9	0.7	0.7

plate and the jet is issuing perpendicular into the boundary layer (i.e. in y-direction). The jet is driven loudspeaker, attached to a cavity of volume 1.85×10^{-5} m^3 and a nozzle with a neck length of 19.5 mm leading to the orifice exit. More details on the actuator can be found in Berk et al. (2016). Six cases are considered for which the actuation parameters are given in Table 1. These cases can be divided into a set of four Strouhal numbers for a fixed velocity ratio and a set of three velocity ratios for a fixed Strouhal number. For all cases the jet is operated using a sinusoidal waveform, leading to a near-sinusoidal velocity cycle.

2.3 Measurement procedures

Velocity fields are measured using particle image velocimetry (PIV). Planar-PIV measurements (giving two-dimensional, two-component velocity fields) are taken in the (x, y)-plane on the centreline of the orifice, spanning from $x = -2\delta$ to 7δ and $y = 0.05\delta$ to 2δ. For two of the measured cases ($St = 0.9$, $r = 0.88$ and $St = 0.7$, $r = 1.35$) a measurement error caused the measurement plane to end at $x = 3\delta$. For this measurement an array of three LaVision ImagerPro LX 16MP cameras is used. The planar velocity fields have a resolution of 0.34 mm per vector. Stereo-PIV measurements (giving two-dimensional, three-component velocity fields) are taken in the (z, y)-plane at streamwise positions of 3δ and 6δ downstream of the orifice, with the plane spanning from $z = -1\delta$ to 1δ and $y = 0.05\delta$ to 2δ. For this measurement two LaVision ImagerPro LX 16MP cameras are placed at opposite sides of the test section, pointing upstream with an internal angle of 60 degrees. The stereo velocity fields have a resolution of 0.35 mm per vector. Measurements are taken phase-locked to the actuation signal at eight equidistant phases (300 image pairs per phase).

2.4 Use of velocity, vorticity and momentum

The background flow is removed in order to measure the strength of the vortical structures imposed on the background flow. In the present study the local velocity components relative to the time-averaged incoming velocity are used as proxy for the background flow, i.e.

$$u^*(x,y) = u(x,y) - u_{in}(y), \tag{3}$$

$$v^*(x,y) = v(x,y) - v_{in}(y) \approx v(x,y), \tag{4}$$

$$w^*(x,y) = w(x,y) - w_{in}(y) \approx w(x,y), \tag{5}$$

where u, v and w indicate the streamwise-, wall-normal- and spanwise-velocity components respectively, u_{in} indicates the incoming velocity and u^* the velocity relative to the incoming flow. The incoming velocity profile is measured upstream of the actuator, averaged over $-1.5 < x/\delta < -1.0$. The spanwise and wall-normal components in the incoming boundary layer are found to be negligible. Using these relative components of velocity, the vorticity fields are given by

$$\omega_z^* = \frac{\partial v^*}{\partial x} - \frac{\partial u^*}{\partial y}, \tag{6}$$

for the relative spanwise vorticity in the (x,y)-plane and

$$\omega_x^* = \frac{\partial w^*}{\partial y} - \frac{\partial v^*}{\partial z}, \tag{7}$$

for the relative streamwise vorticity in the (z,y)-plane.

Vortices are identified in these vorticity fields using swirling strength (see Adrian et al. (2000)) which differentiates between vortices and shear layers. Unless noted otherwise, vorticity fields presented throughout this paper only show vorticity at locations identified by the swirling strength as belonging to a vortex.

In the present paper the terms momentum, momentum flux and streamwise-momentum flux are used interchangeably to indicate the flow of streamwise momentum through a point or plane, i.e. $\dot{P} = \mathrm{d}P/\mathrm{d}t = \rho u^2$, where ρ is the density of the fluid. The streamwise-momentum-flux deficit compared to the incoming flow is given by

$$\Delta\dot{P}(x,y) = -\left(\rho u^2(x,y) - \rho u_{in}^2(y)\right). \tag{8}$$

Using the relative velocity component defined in Equation 3 this equals

$$\Delta\dot{P}(x,y) = -\rho\left((u^* + u_{in})^2 - u_{in}^2\right) = -\rho\left((u^*)^2 + 2u^* u_{in}\right), \tag{9}$$

where u^* is either the measured relative velocity or the reconstructed velocity induced by the vortical structures.

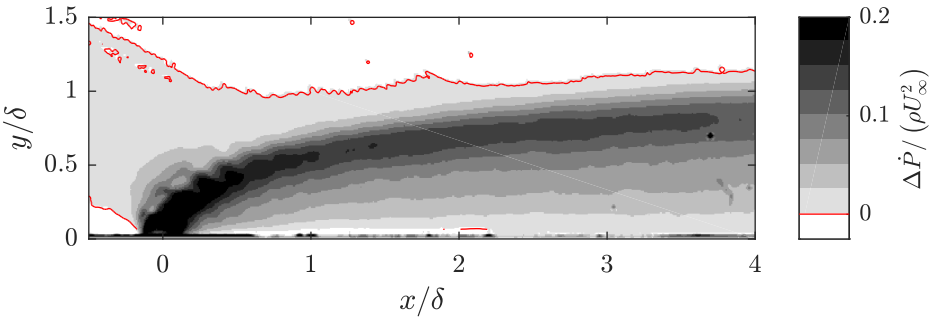

Figure 2: Measured momentum-flux deficit field for the $St = 0.1$, $r = 0.88$ case. The red contour line indicates $\Delta\dot{P} = 0$.

3 Results

As discussed above, the synthetic jet issuing into the turbulent boundary layer creates a momentum deficit in the cross-flow. The measured (streamwise) momentum deficit is presented and discussed in §3.1. The different sources of momentum deficit are identified and discussed using this measured data. The momentum deficit induced by the vortical structures of the jet is reconstructed from the measured velocity fields and discussed in §3.2. An inviscid flow model, predicting the evolution of a train of vortical structures, is presented in §3.3. Throughout the paper qualitative results (including maps of the velocity fields) are presented for the $St = 0.1$, $r = 0.88$ case. Unless stated otherwise, presented analysis methods and conclusions are similar for all cases.

3.1 Measured momentum-flux deficit

The momentum-flux deficit is calculated using Equation 8. The momentum-flux deficit for the $St = 0.1$, $r = 0.88$ case is presented in Figure 2.

Figure 2 shows a plume of streamwise-momentum-flux deficit originating from the orifice of the jet, indicating that the jet creates a wake in the cross flow. The red contour line in Figure 2 indicates the wall-normal height above which the momentum-flux deficit is negative, meaning that the momentum flux has increased. It is assumed that this increase in momentum flux around the wake of the jet is caused by conservation of mass. This implies that the volume flow through each cross plane in the wind tunnel must be equal and therefore if the velocity is decreased in one area, the flow has to speed up around it.

The streamwise-momentum-flux deficit is evaluated as function of streamwise location by integrating in wall-normal direction as

$$\Delta\dot{P}_x(x) = \int \Delta\dot{P}(x, y)\, \hat{z}\, \mathrm{d}y. \tag{10}$$

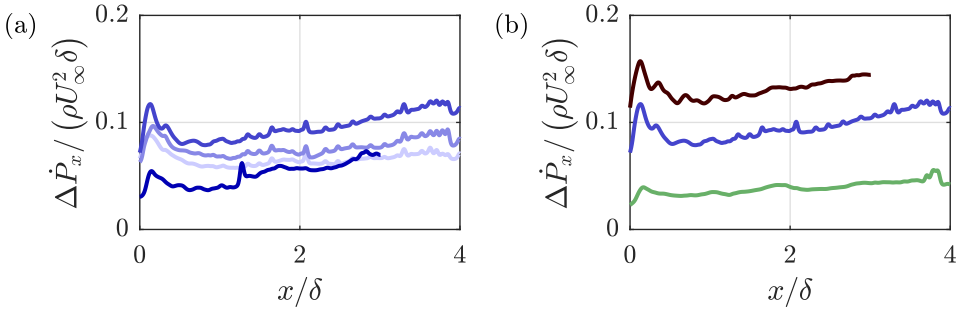

Figure 3: Variation of measured momentum-flux deficit with (a) Strouhal number for $r = 0.88$ and $St = 0.1$ (—), 0.3 (—), 0.7 (—) and 0.9 (—) and with (b) velocity ratio for $St = 0.7$ and $r = 0.45$ (—), 0.88 (—) and 1.35 (—).

This integral is evaluated over the wall-normal extend of the wake (from the wall up to the contour line in Figure 2) and is per unit length in the z-direction ($\hat{z}$). The momentum-flux deficit as function of streamwise distance is presented for all six cases in Figure 3.

The variation of momentum-flux deficit with Strouhal number (see Figure 3a) shows that (for $0.1 < St < 0.7$) the deficit slightly increases for increasing Strouhal number. For the highest Strouhal number ($St = 0.9$) the momentum-flux deficit is considerably lower. It is expected that this is caused by the actuation parameters of the synthetic jet approaching the formation criterion as proposed by Holman et al. (2005). This criterion states that if the ratio of $\bar{u}/f$ is too low, vortices created by the jet will be re-ingested during the suction phase, thereby greatly reducing the effectiveness of the jet and ultimately leading to no jet being formed at all.

The variation of momentum-flux deficit with velocity ratio (see Figure 3b) shows that the momentum-flux deficit increases for an increasing velocity ratio. This variation is intuitive as the velocity ratio is directly related to the strength (either fluidic power, total circulation or total ejected volume) of the jet.

The momentum-flux deficit for each case shows the same trend; a sharp increase followed by a decrease, forming a peak shortly downstream of the jet, after which it shows an almost linear increase. It is assumed that this trend is formed by the different sources of momentum deficit. These sources are represented schematically in Figure 4. Three sources of momentum deficit are identified; viscous blockage (A in Figure 4), increased skin friction (B) and induced velocity (C). It is assumed that the peak shortly downstream of the orifice is caused by viscous blockage of the cross flow by the jet. This is analogue to blockage by a slender column, which will create a quickly recovering blockage wake as presented schematically in Figure 4A (Sumner et al., 2004).

The vortical structures created by the synthetic jet (the shape of these structures will be discussed in §3.2) induce a flow in the wall-normal direction as shown schematically in Figure 4B. This flow is away from the wall between the legs of the structure and towards the wall outside the legs. These wall-normal components redistribute regions of low- and

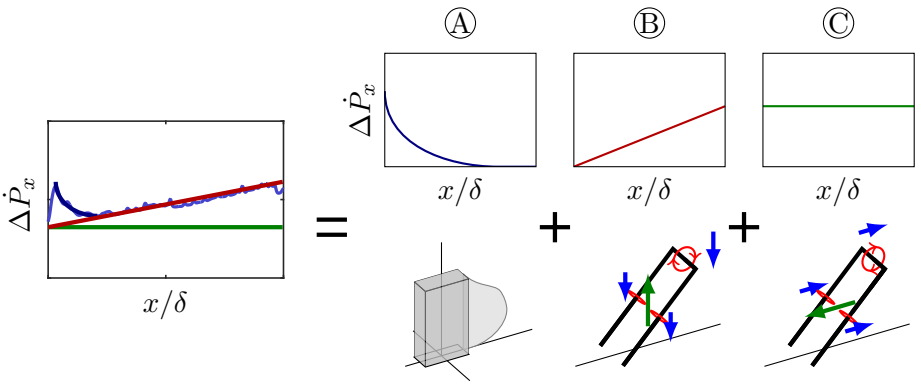

Figure 4: Schematic representation of momentum deficit as a sum of (A) viscous blockage, (B) increased skin friction due to down-wash and (C) induced streamwise velocity.

high momentum, effectively increasing the velocity close to the surface and therewith the skin friction. This increase in skin friction will act as a momentum sink, leading to a constant rate of increase of the momentum-flux deficit as shown in Figure 4B.

The same vortical structures also induce a velocity component in the streamwise direction as shown schematically in Figure 4C. Between the legs of the structure, at the centreline of the jet this component is mainly in the direction opposite to the cross flow, thereby directly inducing a velocity deficit and increasing the momentum-flux deficit. For a constant geometry and strength of the vortical structure, the induced streamwise-momentum-flux deficit is constant as represented schematically in Figure 4C.

A far-field can be defined from both the trajectory and the momentum-flux deficit as $x/\delta > 1$. In this far-field the effect of the vertical velocity on the trajectory (see Figure 2) and the effect of viscous blockage (see Figure 3) have diminished. Unless stated otherwise, in the remainder of this paper the far-field is considered.

The induced momentum-flux deficit in the far-field, as presented schematically in Figure 4C is reconstructed from the data and quantified in §3.2. An inviscid flow model, predicting the evolution of a train of vortical structures is presented in §3.3. This model predicts the induced velocity based on the geometry and strength (circulation) of an input structure.

3.2 Induced momentum-flux deficit

The geometry and strength (i.e. circulation) of the vortical structures created by the synthetic jet are determined using a combination of planar- and stereo-PIV. The reconstruction of these vortical structures is discussed in §3.2.1. Using these reconstructed structures, the vortex-induced velocity is calculated using Biot-Savart law in §3.2.2. The $St = 0.1$, $r = 0.88$ case is used to exemplify the reconstruction method.

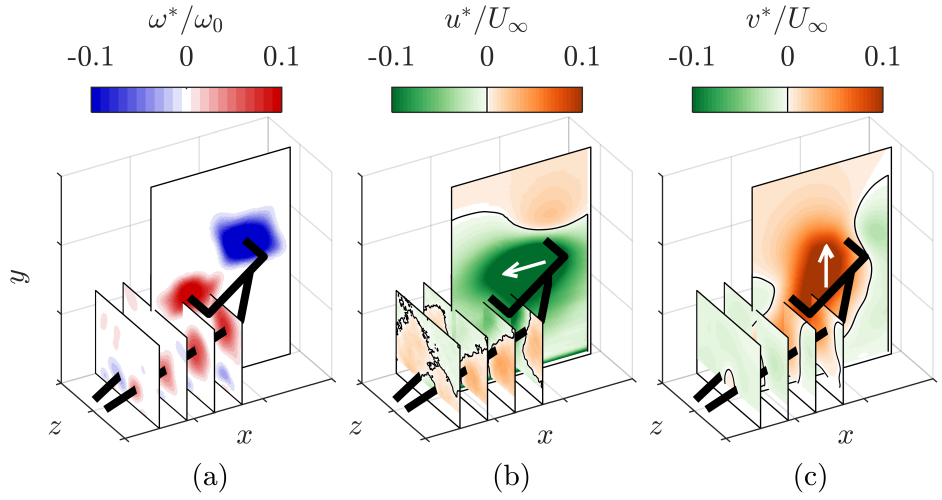

Figure 5: Three-dimensional reconstruction of a single vortical structure.

3.2.1 Reconstruction of vortical structures

As discussed above, the interaction of a synthetic jet with a turbulent boundary layer is expected to result in the creation of hairpin-like vortical structures. The geometry of these structures is reconstructed from a combination of different measurement planes as presented in Figure 5. The four presented spanwise–wall-normal planes are all measured at the same streamwise location during different phases of the jet. The transformation of this phase difference to a streamwise displacement is discussed below.

The observed vorticity fields do not resemble a classical hairpin. Instead, the vortical structure seems to consist of a tilted vortex ring with legs originating from midway the ring as indicated by the thick black line in Figure 5. The shape of this structure can be explained from the interaction of the synthetic jet with the boundary layer. During formation, the vortex ring created by the synthetic jet entrains vorticity from the cross-flow boundary layer. This entrained vorticity has opposite sign to the vorticity in the upstream side of the vortex ring but equal sign to the downstream side, leading to a redistribution of vorticity in the vortex ring. According to Helmholtz's vortex theorems (for inviscid flow) the strength of a vortex filament is constant along its length and cannot end in a fluid. This means that additional vortical filaments need to be formed, leading from midway between the upstream and downstream sides of the vortex ring to the surface, forming the legs of the observed structure. The strength of the legs is then given by the difference in strength between the two sides of the vortex ring. The asymmetry in vorticity distribution along the ring also causes tilting of the ring as the downstream side of the ring (with higher circulation) has a stronger self-induced vertical velocity. This tilting has previously been observed and explained for vortex rings in a shear flow by Lim et al. (2008) and Cheng et al. (2009).

The streamwise- and wall-normal-velocity components measured around the vortical structure are presented in Figure 5b and c. Although the shape of the structure is more

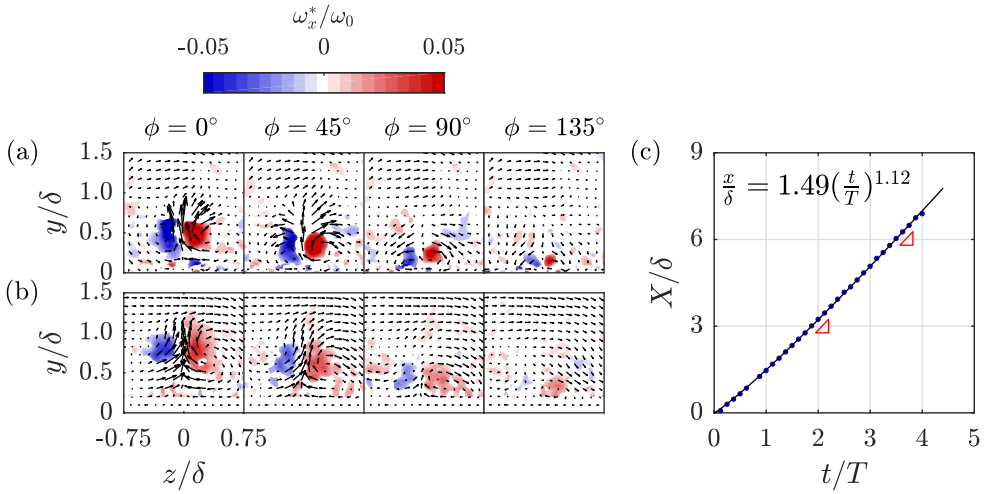

Figure 6: Streamwise vorticity measured using stereo-PIV during four phases, showing the legs of the vortical structure at $x/\delta = 3$ (a) and $x/\delta = 6$ (b). Streamwise position as function of time (c) tracked using planar-PIV. The advection velocity of the structures, given by the slope indicated by the red triangles defines the streamwise separation distance between subsequent fields in (a) and (b).

complicated than that of a single hairpin, the velocity components are similar to those expected from a hairpin (see the schematic representations in Figure 4B and C). The streamwise velocity field is dominated by negative velocity (opposite to the cross-flow direction) within the vortex ring and between the legs. The wall-normal velocity field is dominated by a positive velocity (away from the wall) within the ring and between the legs. The velocity components outside the structure are in the opposite direction, as can expected for the circular motion around vortical filaments. Inside the vortical structure the streamwise- and wall-normal-velocity components induced by the different parts of the structure act in the same direction, leading to a high velocity. Outside the structure the components induced by the different parts of the structure act in opposite directions, leading to a relatively low induced velocity.

The streamwise-vorticity fields of the legs are presented in more detail and for both the $x/\delta = 3$ and 6 locations in Figure 6. The legs can be identified as counter-rotating vortex pairs. The exact position of the legs is defined as the weighted centre of vorticity, calculated for both vortices independently and averaged over the presented range (i.e. $-0.75 < z/\delta < 0.75$ and $0 < y/\delta < 1.5$). As time (i.e. phase) increases, the vortex pair moves closer to the surface, leading to the inclination of the legs as in Figure 5. For both downstream locations the vortex pair is only visible during the four presented phases (out of a total of eight phases).

The advection velocity of the vortical structure is used to translate the temporal spacing between subsequent phases to a spatial distance. This velocity is determined by tracking the head of the vortical structure through time in the streamwise–wall-normal plane. The tracked streamwise position is presented in Figure 6c. The streamwise evolution shows

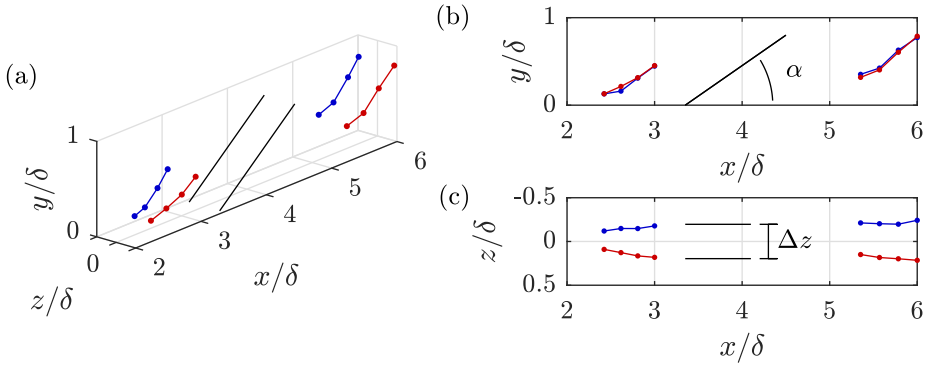

Figure 7: Measured geometry of the legs of the vortical structure at $x/\delta = 3$ and 6. Colours indicate sign of streamwise vorticity (red positive). The black structure indicates the modelled geometry with $\Delta z = 20d$ and $\alpha = 35°$.

a rapid acceleration to a relatively constant advection velocity. This evolution is fitted to a power law (indicated by the black line) which gives an accurate representation. The streamwise advection velocity is calculated as the derivative of this power law. The advection velocities at $x/\delta = 3$ and 6 (indicated by the red triangles) are used to translate the phase differences in Figure 6a and b to a streamwise separation between subsequent vorticity fields. The combination of this streamwise location of the measurement planes with the spanwise and wall-normal location of the vortices as determined from these planes leads to the three-dimensional geometry of the legs as presented in Figure 7.

The legs of the hairpin are presented at streamwise positions $x/\delta = 3$ and $x/\delta = 6$. The side-view presented in Figure 7b shows that although the structure moves away from the wall, the inclination angle of the legs compared to the wall is relatively constant. The top-view presented in Figure 7c shows that the legs are parallel to each other and have a relatively constant separation distance. The black lines show a modelled pair of legs with an inclination angle of $\alpha = 35°$ and a spanwise separation of $\Delta z = 20d$ (for $d = 1$ mm the orifice width) which closely matches the data. The inclination angle and spanwise separation for other cases are found to be similar.

3.2.2 Calculation of vortex-induced velocity

The geometry of the vortical structure is simplified by modelling it as the combination of two hairpins as presented in Figure 8a. These two hairpins originate from the counter-rotating vortices measured in the head of the structure. The vortical filaments forming these hairpins have constant circulation along their length given by Γ_{CW} and Γ_{CCW}, equal to the measured circulation of the clockwise and counter-clockwise vortices respectively. In-line with the above discussion $|\Gamma_{CW}| > |\Gamma_{CCW}|$. Both hairpins overlap in the legs of the structure, leading to partial cancellation of their effect. The velocity induced by the combination of these legs is equal to a velocity induced by legs of magnitude $\Gamma_{leg} = \Gamma_{CW} + \Gamma_{CCW}$. The geometry of the legs is fully determined by the vorticity fields

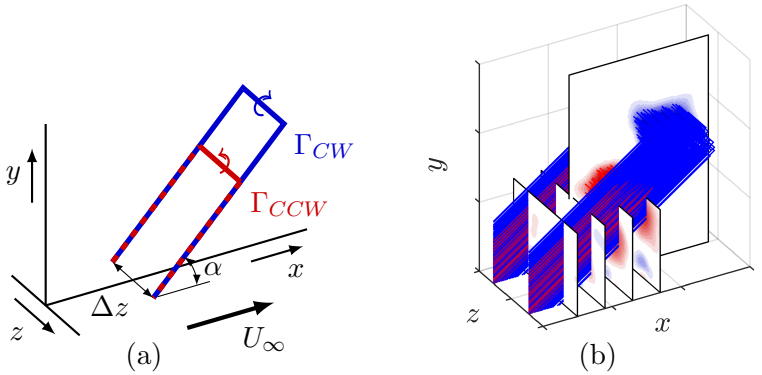

Figure 8: Simplified geometry of the vortical structure modelled as two counter-rotating hairpins (a) and implementation by using each data-point as a separate hairpin (b).

in the (z, y)-plane as discussed above. Using the constant spanwise separation Δz and inclination angle α to describe these legs, only the position and circulation of the head, measured from the vorticity field in the (x, y)-plane is required to fully reconstruct the hairpin vortices.

Instead of using a single hairpin per vortex, a hairpin is modelled at each data-point as presented in Figure 8b. Using each data point of the vorticity fields enables a more representative description of the vorticity distribution. The circulation of each filament is then given by $\Gamma = \omega_z^* \Delta x \Delta y$, which is the area integral of vorticity ω_z^* for data with grid spacing Δx and Δy. For numerical purposes, each filament is described using a finite number of three-dimensional line segments, whose geometry is described by $\vec{ds}$. Biot-Savart law states that the velocity induced by a segment ($\vec{u}_{ind,s}$) on any point (x, y, z) at distance $\vec{\ell}$ from the segment is given by

$$\vec{u}_{ind,s}(x, y, z) = \frac{\Gamma}{4\pi} \frac{\vec{ds} \times \vec{\ell}}{|\vec{\ell}|^3}. \tag{11}$$

The full velocity $\vec{u}_{ind}$ induced on a given point is calculated by summing over the velocities induced by all segments in all filaments, $\vec{u}_{ind}(x, y, z) = \sum \vec{u}_{ind,s}(x, y, z)$.

The three velocity components induced by the filaments in Figure 8b are presented in Figure 9. These velocity fields are the induced velocity components reconstructed from the measured velocity fields in Figure 5. Comparing the measured and induced streamwise and wall-normal components (u^* and v^*) shows great similarity. In general, the velocity within the structure (i.e. between the legs and inside the ring) is in the streamwise direction opposite to the cross flow and the wall-normal direction away from the wall, while the velocity outside the structure is in the opposite direction. The spanwise component of the induced velocity is presented in Figure 9c. Due to symmetry enforced by the hairpin model the spanwise component in the symmetry plane ($z = 0$) is zero.

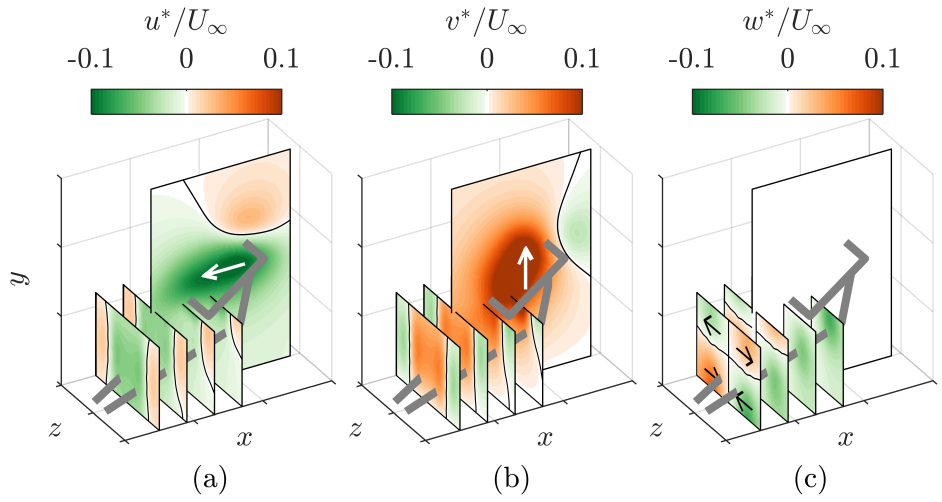

Figure 9: Velocity induced by the three-dimensional vortical structure.

The velocity fields in the spanwise–wall-normal plane located at $x/\delta = 3$ are presented in more detail for a single phase in Figure 10. The presented phase shows a cross-section of the legs of the vortical structure. The streamwise-, wall-normal- and spanwise-velocity components are presented in Figure 10a, b and c respectively. Each figure combines the measured velocity field (left, mirrored) with the induced velocity field (right) using the symmetry across $z/\delta = 0$. Qualitatively the induced velocity fields are largely similar to the measured velocity fields. The streamwise component (a) shows a velocity deficit between the legs and a velocity increase outside the legs. The measured velocity field indicates an increase in velocity above the legs while this is not present in the induced velocity field. This difference – caused by an increase in the velocity outside the wake due to conservation of mass – will be discussed below. The wall-normal component (b) indicates a velocity away from the wall between the legs and a velocity towards the wall outside the legs. These vertical motions redistribute regions of high- and low momentum as will be discussed below. The spanwise component (c) indicates a velocity towards the symmetry plane ($z/\delta = 0$) underneath the legs and a velocity away from this plane above the legs. The combination of the spanwise and wall-normal components indicates a circular motion around each leg as can be expected for the flow around a vortical filament.

The velocity fields in the streamwise–wall-normal plane at $z/\delta = 0$ are presented for a single phase in Figure 11. The presented streamwise extend shows the velocity fields associated with a train of three subsequent vortical structures. Measured (a,b) and induced (c,d) velocity fields are compared for the streamwise (a,c) and wall-normal (b,d) components. Although the strength and wall-normal location of the three structures varies the velocity fields surrounding these structures are qualitatively similar.

Time-averaged velocity fields in the streamwise–wall-normal plane at $z/\delta = 0$, averaged over eight phases, are presented in Figure 12. Measured (a) and induced (c) streamwise velocity components are qualitatively similar. The difference between the two, defined

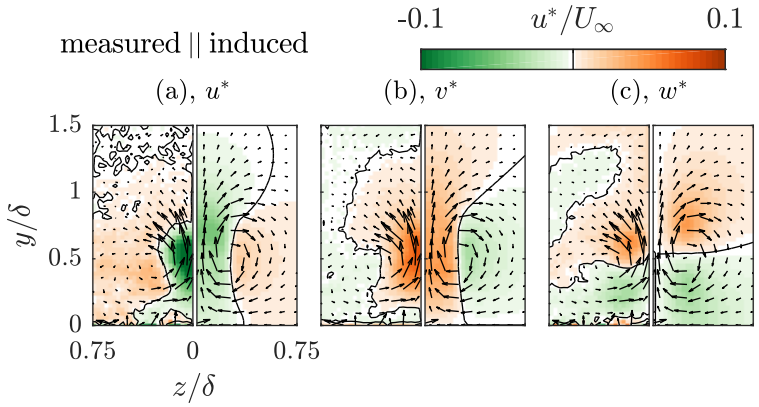

Figure 10: Comparison of phase-locked stereo-PIV data at $x/\delta = 3$ (left half of plots, mirrored) to the computed induced velocity (right half) for the (a) streamwise-, (b) wall-normal- and (c) spanwise-velocity components.

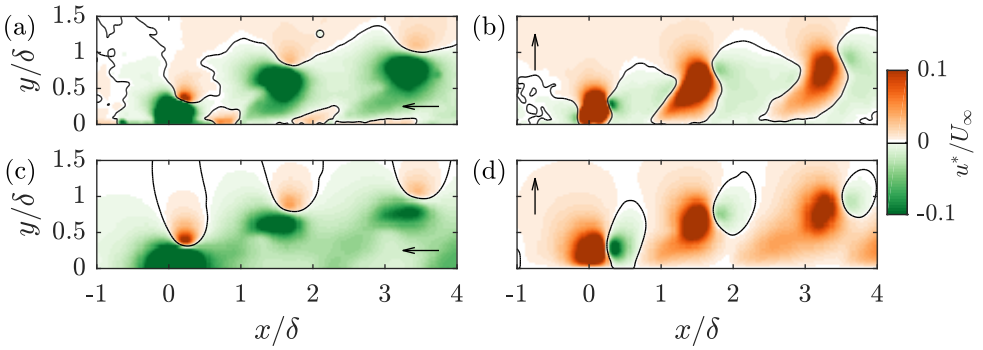

Figure 11: Comparison of phase-locked planar-PIV data at $z/\delta = 0$ (a,b) to the computed induced velocity (c,d) for the streamwise (a,c) and wall-normal (b,d) components.

as $\Delta u^* = u^*_{meas} - u^*_{ind}$ (e) shows three regions in the far-field (i.e. $x/\delta > 1$) where the measured and induced components are different. Region A, above the wake of the jet (roughly at $y/\delta > 1.0$), shows a higher measured than induced velocity. It is expected that this is caused by the conservation of mass through cross-planes in the wind tunnel. As the incoming velocity is slowed down in part of this plane (due to the wake of the jet), the velocity of the surrounding flow has to increase to keep the same mass flux through each plane. The difference in region B, roughly at $0.3 < y/\delta < 1.0$, indicates a measured velocity that is lower than the induced velocity (i.e. a stronger wake). It is assumed that this is due to the up-wash of low-momentum fluid as caused by the vertical component of the induced velocity. Similarly, region C (roughly at $y/\delta < 0.3$) indicates a higher measured than induced velocity. Analogue to the up-wash in region B it is assumed that this increase in velocity is caused by the down-wash of high-momentum fluid. The spanwise–wall-normal planes in Figure 10 showed that the vertical component of the velocity field consists of upward motions between the legs and downward motions next to the legs, i.e. low-momentum fluid is removed from the wall between the legs of the structure while high-momentum fluid is transported towards the wall outside the legs.

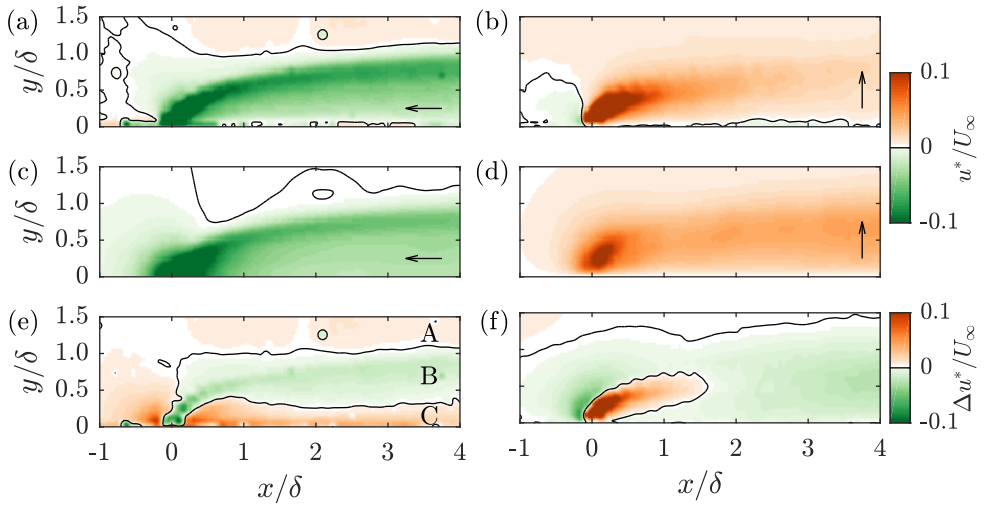

Figure 12: Comparison of time-averaged planar-PIV data at $z/\delta = 0$ (a,b) to the computed induced velocity (c,d) as well as the difference defined as $\Delta u^* = u^*_{meas} - u^*_{ind}$ (e,f) for the streamwise (a,c,e) and wall-normal (b,d,f) components.

Time-averaged measured and induced wall-normal components are presented in Figure 12b and d. The measured an induced velocity fields are qualitatively very similar and are both dominated by a velocity away from the wall. The difference between the two cases ($\Delta v^* = v^*_{meas} - v^*_{ind}$) (f) indicates that the measured vertical velocity is much higher than the induced velocity in the core of the jet but lower just upstream of the jet. This is caused by the fact that the jet has a given wall-normal velocity ($\bar{u}$) at the exit of the jet. This exit velocity is present in the measured velocity field, but not in the induced field, causing the core of the jet to be stronger for the measured case. Since synthetic jets are formed entirely from the surrounding fluid by alternating blowing and suction cycles, the flow upstream of the actuator is ingested into the jet as can be seen from the negative vertical velocity in the measured velocity field. In the far-field ($x/\delta > 1$), the wall-normal velocity is over-predicted in most of the flow field. It is assumed that this is caused by the boundary layer compensating for the upward motion of vortical structures. With these structures moving upward due to their induced velocity a low pressure region is created underneath these structures. It can be assumed that the flow between subsequent structures is downward to compensate this pressure difference. This viscous effect leads to the over-prediction of wall-normal velocity as observed in Figure 12.

The streamwise-momentum-flux deficit ($\Delta \dot{P}_x$) as was presented for the measured cases in Figure 3 is recalculated based on the induced velocity only. This induced streamwise-momentum-flux deficit is presented in Figure 13. Note that for the $r = 0.88$, $St = 0.9$ and $r = 1.35$, $St = 0.7$ cases the measurement plane is only up to $x/\delta = 3$. Due to the reconstruction of hairpin structures based on the location of the heads (i.e. based on the most downstream part of the structures) the end of the measurement plane has an influence upstream. This is visible in Figure 13 by the decline in induced momentum-flux deficit for these two cases shortly before reaching $x/\delta = 3$. Apart from this artificial

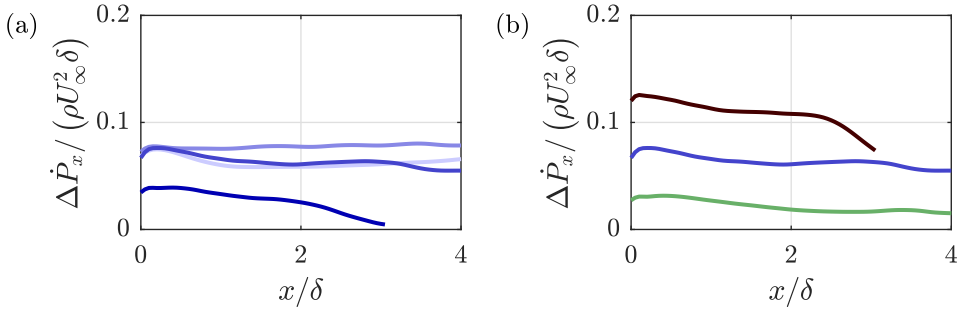

Figure 13: Variation of induced momentum-flux deficit with (a) Strouhal number for $r = 0.88$ and $St = 0.1$ (—), 0.3 (—), 0.7 (—) and 0.9 (—) and with (b) velocity ratio for $St = 0.7$ and $r = 0.45$ (—), 0.88 (—) and 1.35 (—).

decline, the induced deficit is relatively constant with streamwise location for all cases.

Figure 13a presents the induced momentum-flux-deficit for different Strouhal numbers. For the three lowest Strouhal numbers the induced deficit is relatively equal. This can be explained using the theoretical circulation of vortex rings produced by the synthetic jet. During the formation of a vortex ring at the jet exit, the circulation grows with $\mathrm{d}\Gamma/\mathrm{d}t \approx u^2(t)/2$ (Shariff and Leonard, 1992), where $u(t)$ is the instantaneous centreline velocity. For a harmonic velocity cycle as used in the present study this implies that the circulation of a single structure (i.e. created during one cycle) scales with $\Gamma \propto \bar{u}^2/f$. The number of these structures created per unit time equals the frequency (i.e. $\Gamma_{TA} \propto \bar{u}^2$), cancelling the effect of frequency on the time-averaged strength of the train of vortices. As discussed above, for high Strouhal numbers the jet formation criterion is approached, leading to (partial) re-ingestion of circulation during the suction phase of the jet. This leads to a lower strength of the vortical structures for $St = 0.9$, explaining the lower induced momentum-flux deficit.

The induced streamwise-momentum-flux deficit is presented for different velocity ratios in Figure 13b. The induced deficit increases with velocity ratio. This can be expected from the larger strength of the vortical structures as discussed above.

The streamwise-momentum-flux deficit is averaged over $1 < x/\delta < 2$ for both the measured and the induced case. This mean momentum-flux deficit $\langle\Delta\dot{P}_x\rangle$ is presented in Figure 14 for the measured and induced cases as well as the difference between the two. Referring back to the decomposition as presented in Figure 4 it can be expected that for $x/\delta > 1$ the difference between the measured and induced momentum deficit is equal to the momentum deficit caused by an increase in skin friction. For an increasing Strouhal number the total (i.e. measured) momentum-flux deficit initially increases but decreases sharply for high Strouhal numbers. As discussed above this decrease is expected to be caused by the formation criterion. For low Strouhal numbers the measured and induced momentum deficit is equal, suggesting that the skin friction is not increased. This could be caused by the fact that for low Strouhal numbers subsequent vortical structures are separated far enough for the flow to recover between these structures. For

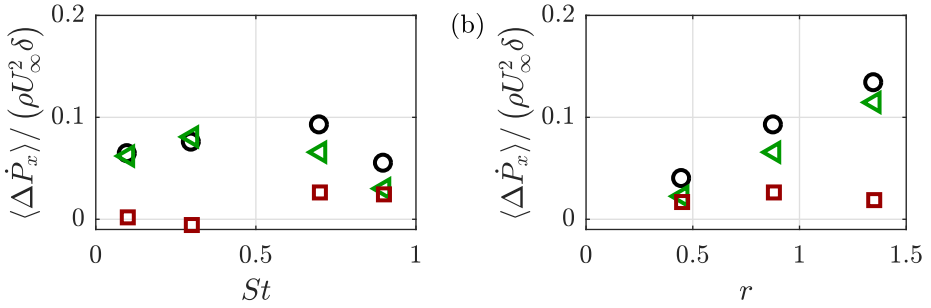

Figure 14: Mean wake strength averaged over $1 < x/\delta < 2$ using the measured data (○), reconstructed induced velocity (◁) and the difference between the two (□) for $r = 0.88$ (a) and $St = 0.7$ (b).

higher Strouhal numbers the separation between the structures is smaller which does not give the flow near the surface time or space to recover, leading to an increase in velocity close to the wall (due to down-wash of high-momentum fluid) and subsequently an increase in skin friction. This increase in skin friction is manifested as the difference between the measured and induced momentum deficit for high Strouhal numbers. The total momentum-flux deficit increases with velocity ratio which can be expected as discussed above. The difference between the measured and induced momentum-flux deficit is relatively constant, suggesting that there is a constant increase in skin friction.

3.3 Predictive inviscid-flow model

An inviscid-flow model is developed to predict the temporal evolution of a train of vortical structures. The Matlab code for the model is given in the supplementary material. The model is based on an input vortical structure which moves due to a specified cross-flow advection velocity, its self-induced velocity and the velocity induced by other vortical structures. The input structure used here is presented in Figure 15a but can easily be changed in the developed model. Similar to the hairpins in the analysis discussed above, the vortical filament is divided into a finite number of segments where each segment is located between two nodes. At every time-step the velocity induced on each node is determined by adding the contributions of all segments. The displacement of each node is then given by the velocity induced on the node multiplied by the specified time step.

The inviscid-flow model is used purely for qualitative comparisons to the measurement data and a qualitative description of the flow. Results of the model can be used to evaluate (i) the deformation of the input geometry of the vortical structures, (ii) the instantaneous and time-averaged three-dimensional three-component velocity fields and (iii) the wall-normal evolution (i.e. trajectory) of the vortical structures.

Results are presented for an example structure based on structures observed in the present study for the $St = 0.1$, $r = 0.88$ case.

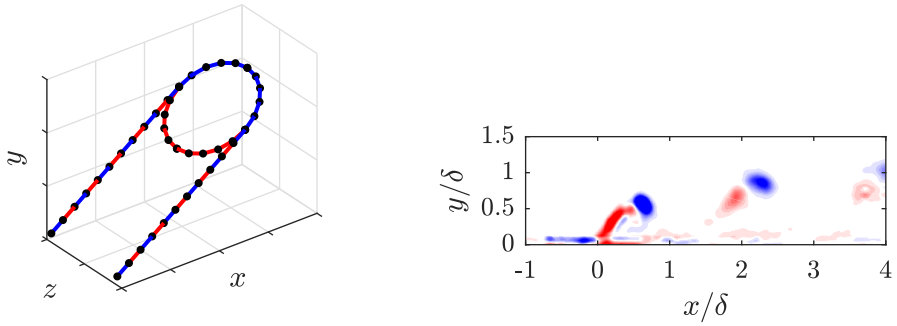

(a) (b)

Figure 15: Input structure for the inviscid flow model (a) and measured vorticity field for $St = 0.1$, $r = 0.88$ showing roll-up of vortices up to $x/\delta \approx 1$ (b).

3.3.1 Initial conditions

The geometry of the used input structure is presented in Figure 15a. This geometry is based on the double hairpin presented in Figure 8a and consists of a circular ring with legs leading from the sides of the ring to the surface. The downstream half of the ring has a circulation Γ_{CW}, the upstream side has a circulation Γ_{CCW} and the legs have a circulation $|\Gamma_{leg}| = |\Gamma_{CCW}| - |\Gamma_{CW}|$. The initial position of the structure is defined using the centre of the ring. Together with the inclination angle and spanwise separation between the legs (equal to the diameter of the ring), this starting position fully defines the geometry presented in Figure 15a.

For the results presented below the initial conditions are based on the data as presented above. The inclination angle and spanwise separation of the legs are $\alpha = 35°$ and $\Delta z = 20$ mm ($\Delta z/\delta = 0.44$) respectively. The initial position of the structure as well as the circulation of both sides of the vortex ring are measured in the phase-locked vorticity fields as presented in Figure 15b. This vorticity field shows that the vortical structure is fully rolled up at approximately $x/\delta = 1$ (the start of the far-field as defined in this study), at which the wall-normal position is approximately $y/\delta = 0.6$. At this location the circulation of the two vortices can be determined by integrating the vorticity over the area of the vortex. For the case shown here ($St = 0.1$, $r = 0.88$) the initial circulation of the vortices is given by $\Gamma_{CW} = 0.06$ m^2/s and $\Gamma_{CCW} = -0.04$ m^2/s respectively.

3.3.2 Time evolution

The model uses a certain time step Δt based on the frequency of the jet (here $\Delta t/T = 1/32$ is used). At each time step nodes are displaced driven by a combination of an advection velocity of the cross flow and velocity components induced by each segment. The velocity $\vec{u}_{ind,s}$ induced on a point (x, y, z) by a segment $\vec{ds}$ is calculated using

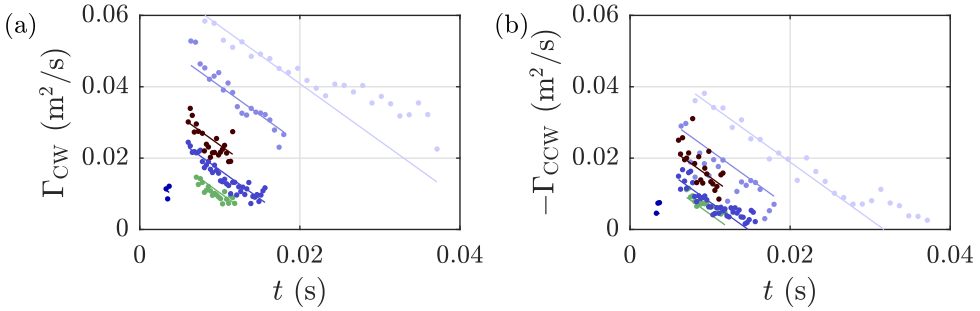

Figure 16: Decay of circulation for (a) the clockwise vortex and (b) the counter-clockwise vortex as function of time for $r = 0.88$ and $St = 0.1$ (●), 0.3 (●), 0.7 (●) and 0.9 (●) and (b) $St = 0.7$ and $r = 0.45$ (●), 0.88 (●) and 1.35 (●).

Biot-Savart law, given by

$$\vec{u}_{ind,s}(x,y,z) = \frac{\Gamma}{4\pi} \frac{\vec{ds} \times \vec{\ell}}{|\vec{\ell}| \left(\max\left[|\vec{\ell}|, R\right]\right)^2}, \tag{12}$$

where $\vec{l}$ is the vector from the centre of the segment to the point (x, y, z) and R is a Rankine vortex radius. A Rankine vortex is used to limit the velocity close to the centre of the vortex. In the real flow this limitation is enforced by the viscous core of the vortex. The total induced velocity is determined by summing over the contributions of all segments, i.e. $\vec{u}_{ind}(x,y,z) = \sum \vec{u}_{ind,s}(x,y,z)$.

The displacement of each node at every time step Δt is given by

$$\Delta\vec{x} = (\vec{u}_{ind} + \vec{u}_{adv})\,\Delta t, \tag{13}$$

where $\vec{u}_{adv}$ is the advection velocity caused by the cross flow. For the cases in the present study the advection velocity in streamwise direction is equal to approximately 80% of the free-stream velocity, i.e. $\vec{u}_{ind}/U_\infty = [0.8,\ 0,\ 0]^{\mathrm{T}}$.

The circulation of the vortical structures decays over time. The circulation of the measured cases in the present study is presented in Figure 16a and b for the clockwise and counter-clockwise vortex respectively. A linear trend is added to the data, indicating a constant decay of $\mathrm{d}\Gamma/\mathrm{d}t = 1.61$ m^2/s^2.

3.3.3 Results of the model

As discussed above the developed model predicts the evolution of a given train of input structures. The resulting strength and location of these structures can be used to study (i) the deformation of the vortical structures, (ii) the three-dimensional three-component induced velocity field and (iii) the wall-normal penetration of the structures in the cross flow (i.e. the trajectory). Results are discussed here based on the $St = 0.1$, $r = 0.88$ case.

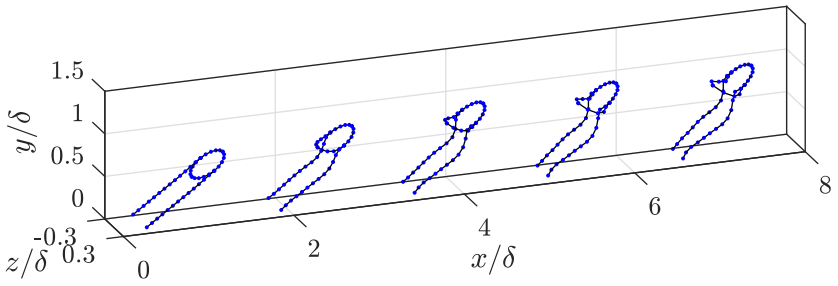

Figure 17: Instantaneous result of the inviscid-flow model for $St = 0.1$, $r = 0.88$.

(i) An instantaneous snapshot of the vortical structures resulting from the model is presented in Figure 17. The shape of the structures shows a deformation from the input geometry (around $x/\delta = 1$) to a geometry resembling the shape of the reconstructed structures as presented in Figure 5a (around $x/\delta = 7$). The deformation to this shape indicates that the induced velocity is the driving force leading to this geometry rather than viscous effects or initial conditions.

(ii) Given the position of vortical structures as presented in Figure 17, the three components of the induced velocity can be calculated at any point (x, y, z) using Biot-Savart. The velocity induced in the streamwise–wall-normal plane at the centreline of the jet ($z/\delta = 0$) is presented in Figure 18. The instantaneous streamwise- and wall-normal-velocity components (corresponding to the position of the structures as presented in Figure 17) are presented in a and b respectively. Results are qualitatively similar to the measured and reconstructed phase-locked velocity fields presented in Figure 11. The time-averaged (constructed from 32 phases) streamwise- and wall-normal-velocity components are presented in c and d respectively. Excluding the start-up phenomena, the time-averaged velocity fields are qualitatively similar to the reconstructed velocity fields presented in Figure 12c and d with the streamwise component dominated by a flow in opposite direction of the cross flow and the wall-normal component dominated by a flow away from the wall. Both velocity components are strongest at the wall-normal location of the head of the vortical structure rather than the legs, indicating that the momentum deficit as well as up-wash are mainly driven by the vortex ring. Both components show a clear decay with streamwise distance caused by the decay of circulation of the vortical structure.

For most of the present paper the velocity and the momentum-flux deficit have been considered in the streamwise–wall-normal centreline plane. Due to the nature of the flow around a vortex, the velocity components are of opposite direction inside and outside the legs of the vortical structure (see for example the schematics in Figure 4). This makes it important to consider the velocity outside the structure (i.e. in off-centreline planes) as well. The inviscid-flow model enables computation of the three-dimensional three-component velocity field (as opposed to being restricted to a given measurement

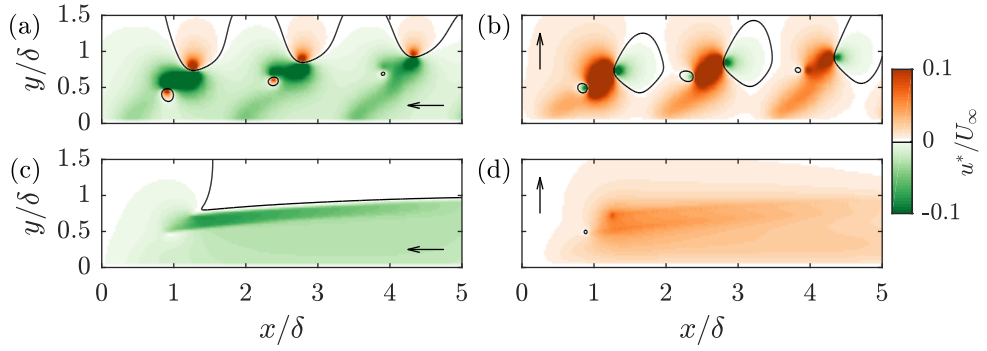

Figure 18: Phase-locked (a,b) and time-averaged (c,d) streamwise (a,c) and wall-normal (b,d) velocity components computed by the inviscid-flow model for the $St = 0.1$, $r = 0.88$ case.

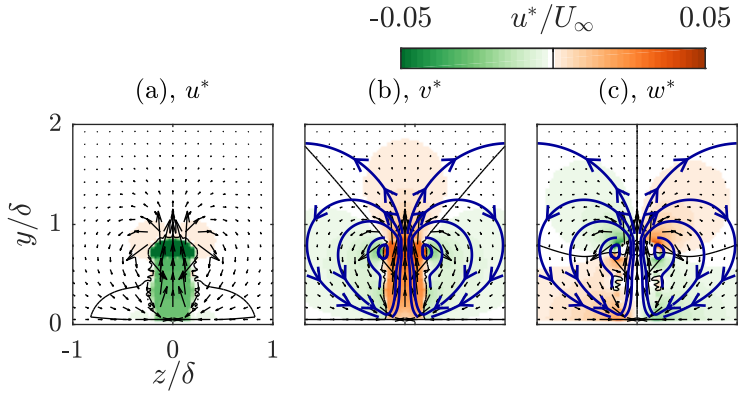

Figure 19: Time-averaged (a) streamwise-, (b) wall-normal- and (c) spanwise-velocity components in the spanwise–wall-normal plane at $x/\delta = 3$ computed by the inviscid-flow model for the $St = 0.1$, $r = 0.88$ case. Selected streamlines are plotted in blue. Contour lines at $u^*/U_\infty = 0$ are plotted in black.

plane in the performed PIV experiments). The time-averaged velocity in the spanwise–wall-normal plane at $x/\delta = 3$ is presented in Figure 19 for the (a) streamwise-, (b) wall-normal- and (c) spanwise-velocity components. The streamwise component (a) indicates that within the structure there is a strong negative component as seen in the centreline plane. Outside the structure (both above and to the sides) the induced velocity is slightly positive, indicating a flow in the same direction as the cross flow. However, this component is negligible compared to the negative component and decays even further with distance from the structure. The wall-normal component (b) shows that within the structure the velocity is away from the wall, as seen in the centreline plane. In contrast, to the sides of the structure the induced velocity is towards the wall. These vertical components lead to the up-wash of low-momentum fluid at the centreline of the structures and down-wash of high momentum fluid at the sides of the structure. The spanwise component (c) shows a velocity away from the centreline above the structure and towards the centreline below the head of the structure. Selected in-plane streamlines are overlaid on the velocity maps. These streamlines indicate a time-averaged circular

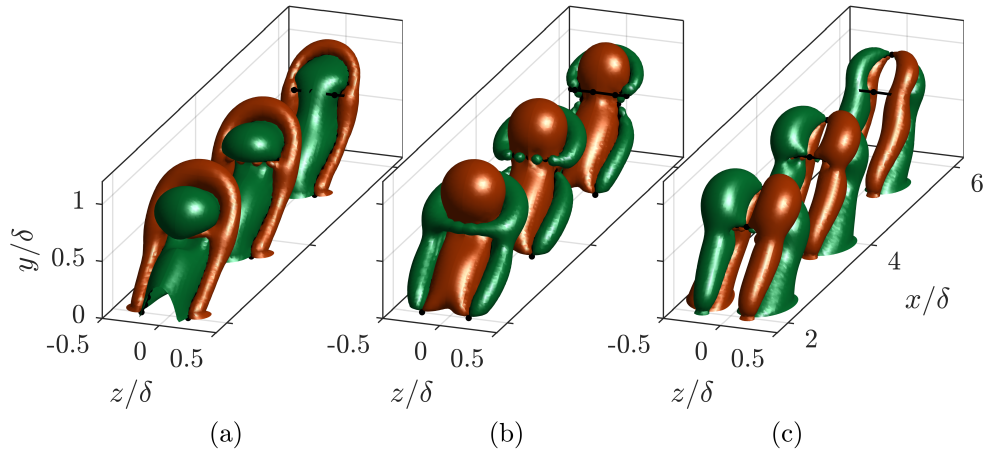

Figure 20: Iso-contours of the (a) streamwise-, (b) wall-normal-, and (c) spanwise-velocity component computed by the inviscid-flow model for the $St = 0.1$, $r = 0.88$ case. Iso-contours indicate $u^*/U_\infty = \pm 0.02$. Vortical filaments are indicated by black dots (nodes) and lines (segments).

motion similar to the flow around a steady counter-rotating vortex pair (also called streamwise rollers) as widely observed for steady jets in cross flow (Mahesh, 2013). Large streamwise rollers have been observed both instantaneously and in time-averaged sense for synthetic jets in cross flow by for example Van Buren et al. (2016a). The time-averaged circular motion causes a net increase in streamwise momentum near the wall and around the vortical structures and a net decrease away from the wall and within the vortical structure. This increase in streamwise momentum near the wall was observed in Figure 12e and leads to an increase in skin friction, adding to the momentum-flux deficit.

The instantaneous three-dimensional velocity field is presented in Figure 20 using iso-contours of velocity at $u^*/U_\infty = \pm 0.02$ for the (a) streamwise, (b) wall-normal and (c) spanwise components respectively. These three-dimensional structures indicate the same circular motions around the vortical filaments as observed above in streamwise–wall-normal and spanwise–wall-normal plane and as can be expected from vortices. The dominance of the component opposite to the cross flow as well as the component away from the wall is clearly visible in these three-dimensional representations.

The time-averaged three-dimensional velocity field, averaged over 32 phases, is presented in Figure 21 using iso-contours of velocity at $u^*/U_\infty = \pm 0.02$ for the (a) streamwise, (b) wall-normal and (c) spanwise components respectively. These time-averages show that the non-dominant components (i.e. in the direction of the cross flow, towards the wall and spanwise components) are either cancelled-out due to the time-averaging or decay to below the level of the iso-contour. In contrast, the dominant components (i.e. opposite to the cross flow and away from the wall) are still visible. This is in agreement with the time-averages in the spanwise–wall-normal planes presented in Figure 19 where

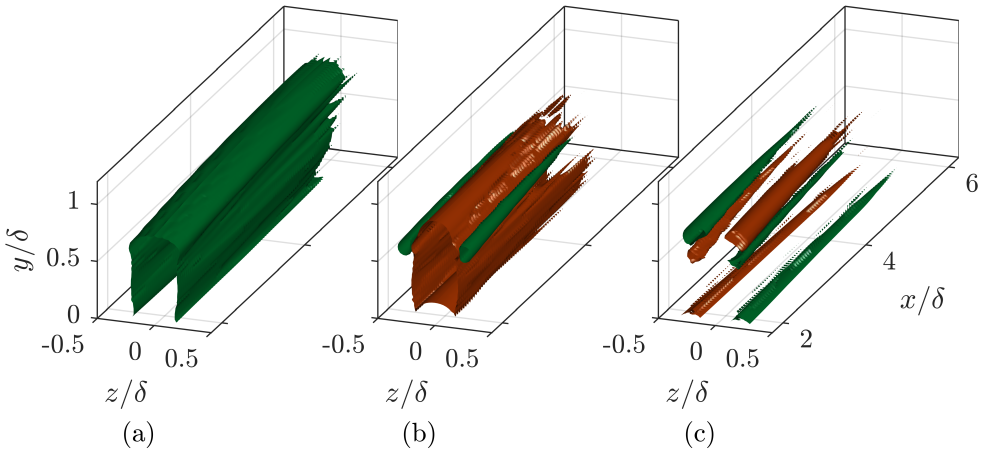

Figure 21: Iso-contours of the (a) streamwise-, (b) wall-normal-, and (c) spanwise-velocity component computed by the inviscid-flow model for the $St = 0.1$, $r = 0.88$ case. Iso-contours indicate $u^*/U_\infty = \pm 0.02$. Vortical filaments are indicated by black dots (nodes) and lines (segments).

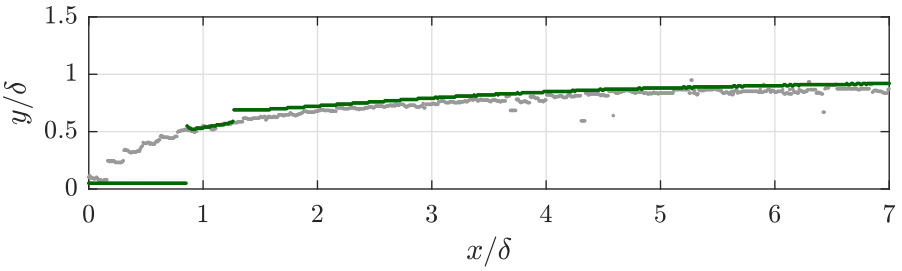

Figure 22: Trajectory computed by the inviscid flow model (green dots) compared to the measured trajectory (grey dots).

the dominant components are of much larger magnitude than other components. The three-dimensional velocity fields also visualize the decay of both the wake and up-wash as the iso-contours disappear around $x/\delta = 5$, indicating that velocity components have fallen below $u^*/U_\infty = \pm 0.02$.

It is important to note that although the time-averaged flow corresponds to the flow around steady streamwise rollers, the instantaneous velocity fields (see Figure 20) indicate a significant spatial variation of the flow.

(iii) The trajectory of the jet in the model is compared to the measured trajectory for the $St = 0.1$, $r = 0.88$ case in Figure 22. The trajectory is defined as locations of maximum velocity deficit. Note that in the model the vortical structures are created at $x/\delta = 1$ at a wall-normal height of $y/\delta = 0.6$ as determined from the data. Downstream of this location the measured and modelled jet show the same trajectory. This implies that downstream of $x/\delta = 1$, i.e. in the far-field of the jet, the trajectory is driven by the induced velocity of the vortical structures. This means that in this far-field the effect of the vertical momentum created at the jet exit has disappeared.

4 Conclusions

The interaction of a synthetic jet with a cross flow leads to a momentum-flux deficit in the cross flow. In the literature this deficit is often ascribed to either viscous blockage of the cross flow by the synthetic jet or by the up-wash of low-momentum fluid. The present paper has introduced and discussed a third source of the momentum-flux deficit: a velocity induced in the direction opposite to the cross flow by the vortical structures created by the synthetic jet.

It is shown that the momentum deficit created by viscous blockage recovers quickly downstream of the jet exit. It is hypothesized that the main influence of up-wash is the accompanying down-wash of high-momentum fluid, increasing the effect of skin friction which acts as a momentum sink.

The effect of vortex-induced velocity is determined by reconstructing the vortical structures created by the synthetic jet using measured velocity fields. The velocity induced by these reconstructed structures is calculated by applying Biot-Savart law to these measured structures. This induced velocity shows large qualitative and quantitative similarity to the measured velocity fields, indicating that the driving source of velocity fluctuations is the induced velocity, rather than blockage or up-wash. It is shown that for low Strouhal numbers the momentum deficit downstream of the blockage wake is entirely caused by the velocity induced in the direction opposite of the cross flow. This implies that the increase in skin friction is negligible for these low Strouhal numbers, which can be explained by the large separation between subsequent structures, enabling the flow to recover between structures. For higher Strouhal numbers a constant offset between the measured and induced momentum deficit is observed, suggesting a constant increase in skin friction. The momentum-flux deficit starts to decrease for high Strouhal numbers, caused by the approach of the formation criterion, meaning that part of the synthetic jet is re-ingested during the suction phase of the jet, decreasing its strength. The momentum deficit increase with velocity ratio, caused by the increasing strength of vortical structures created by the jet. It is shown that the increase in skin friction is relatively constant with velocity ratio.

An inviscid-flow model is developed in which the evolution of a train of input structures of given geometry and circulation is predicted. Results of the model are presented for a single case equal to one of the measured cases. It is shown that the geometry of the vortical structure in the model deforms from the simplified input structure to a shape resembling the measured vortical filaments. This suggests that the shape of the vortical structures is driven by the induced velocity rather than viscous effects or initial conditions. The inviscid-flow model is able to reconstruct three-dimensional three-component velocity fields. Velocity fields computed by the model in planes equal to the measurement planes show a great (qualitative) similarity of the measurements to the inviscid computations. The instantaneous velocity field is dominated by a component

opposite to the cross flow and away from the wall within the vortical structure. Outside the vortical structure a weaker component is present in the direction of the cross flow and towards the wall. The same is true in the time-averaged velocity field.

The far-field trajectory of the vortical structures in the inviscid-flow model is equal to the measured trajectory of the synthetic jet.

The present paper has presented evidence that the velocity induced by vortical structures created by a synthetic jet plays an important role in the velocity field around the jet. In the far-field of the jet this induced velocity is the main contributor to the momentum deficit in the cross flow as well as the development (both the trajectory and structure) of the jet.

References

Abbassi, M. R., Baars, W., Hutchins, N., and Marusic, I. (2017). Skin-friction drag reduction in a high-Reynolds-number turbulent boundary layer via real-time control of large-scale structures. *Int. J. Heat Fluid Flow*, 67(B):30–41.

Adrian, R. J., Christensen, K. T., and Liu, Z. C. (2000). Analysis and interpretation of instantaneous turbulent velocity fields. *Exps. Fluids*, 29(3):275–290.

Adrian, R. J. and Westerweel, J. (2011). *Particle Image Velocimetry*. Cambridge Aerospace Series. Cambridge University Press.

Airbus (2017). Airbus family figures, June 2017 edition.

Amitay, M. and Cannelle, F. (2006). Evolution of finite span synthetic jets. *Phys. Fluids*, 18(5):054101.

Athanassiadis, A. G. and Hart, D. P. (2016). Effects of multijet coupling on propulsive performance in underwater pulsed jets. *Phys. Rev. Fluids*, 1(034501):034501.

Avdis, A., Lardeau, S., and Leschziner, M. (2009). Large eddy simulation of separated flow over a two-dimensional hump with and witwith control by means of a synthetic slot-jet. *Flow Turbul. Combus.*, 83:343–370.

Aydemir, E., Worth, N. A., and Dawson, J. R. (2012). The formation of vortex rings in a strongly forced round jet. *Exps. Fluids*, 52(3):729–742.

Baidya, R., Philip, J., Hutchins, N., Monty, J. P., and Marusic, I. (2017). Distance-from-the-wall scaling of turbulent motions in wall-bounded flows. *Phys. Fluids*, 29:020712.

Barros, D., Borée, J., Noack, B., Spohn, A., and Ruiz, T. (2016a). Bluff body drag manipulation using pulsed jets and coanda effect. *J. Fluid Mech.*, 805:422–459.

Barros, D., Borée, J., Noack, B. R., and Spohn, A. (2016b). Resonances in the forced turbulent wake past a 3D blunt body. *Phys. Fluids*, 28(6):065104.

Berk, T. and Ganapathisubramani, B. (2017). Effects of vortex-induced velocity on the wake of a synthetic jet issuing into a turbulent boundary layer. Manuscript under preparation.

Berk, T., Gomit, G., and Ganapathisubramani, B. (2016). Vectoring of parallel synthetic jets: a parametric study. *J. Fluid Mech.*, 804:467–489.

Berk, T., Hutchins, N., Marusic, I., and Ganapathisubramani, B. (2017a). Trajectory of a synthetic jet issuing into high reynolds number turbulent boundary layers. *J. Fluid Mech.* Manuscript submitted for publication.

Berk, T., Medjnoun, T., and Ganapathisubramani, B. (2017b). Entrainment effects in periodic forcing of the glow over a backward-facing step. *Phys. Rev. Fluids*, 2:074605.

Canton, J., Örlü, R., Chin, C., Hutchins, N., Monty, J., and Schlatter, P. (2016). On large-scale friction control in turbulent wall flow in low Reynolds number channels. *Flow Turbul. Combus.*, 97(3):811–827.

Carpy, S. and Manceau, R. (2006). Turbulence modelling of statistically periodic flows: Synthetic jet into quiescent air. *Int. J. Heat Fluid Flow*, 27(5):756–767.

Cater, J. E. and Soria, J. (2002). The evolution of round zero-net-mass-flux jets. *J. Fluid Mech.*, 472:167–200.

Cattafesta, L. N. and Sheplak, M. (2011). Actuators for active flow control. *Annu. Rev. Fluid Mech.*, 43(1):247–272.

Chauhan, K. A., Monkewitz, P. A., and Nagib, H. M. (2009). Criteria for assessing experiments in zero pressure gradient boundary layers. *Fluid Dyn. Res.*, 41(021404):1–23.

Cheng, M., Lou, J., and Lim, T. T. (2009). Motion of a vortex ring in a simple shear flow. *Phys. Fluids*, 21(8):081701.

Chun, K. B. and Sung, H. J. (1996). Control of turbulent separated flow over a backward-facing step by local forcing. *Exps. Fluids*, 21:417–426.

Dahan, J. A., Morgans, A. S., and Lardeau, S. (2012). Feedback control for form-drag reduction on a bluff body with a blunt trailing edge. *J. Fluid Mech.*, 704:360–387.

Dandois, J., Garnier, E., and Sagaut, P. (2007). Numerical simulation of active separation control by a synthetic jet. *J. Fluid Mech.*, 574:25–58.

de Silva, C. M., Hutchins, N., and Marusic, I. (2015). Uniform momentum zones in turbulent boundary layers. *J. Fluid Mech.*, 786:309–331.

del Álamo, J. C., Jiménez, J., Zandonade, P., and D., M. R. (2004). Scaling of the energy spectra of turbulent channels. *J. Fluid Mech.*, 500:135–144.

Fan, Y., Arwatz, G., Van Buren, T., Hoffman, D. E., and Hultmark, M. (2015). Nanoscale sensing devices for turbulence measurements. *Exps. Fluids*, 56(138).

Gad-el-Hak, M. (1994). Interactive control of turbulent boundary layers: A futuristic overview. *AIAA J.*, 32(9):1753–1765.

Gad-el-Hak, M. (2007). *Flow Control: Passive, Active and Reactive Flow Management*. Cambridge University Press, first edition.

Ganapathisubramani, B., Hutchins, N., Monty, J. P., Chung, D., and Marusic, I. (2012). Amplitude and frequency modulation in wall turbulence. *J. Fluid Mech.*, 712:61–91.

Gautier, N. and Aider, J.-L. (2014). Feed-forward control of a perturbed backward-facing step flow. *J. Fluid Mech.*, 759:181–196.

Gautier, N., Aider, J.-L., Duriez, T., Noack, B. R., Segond, M., and Abel, M. (2015). Closed-loop separation control using machine learning. *J. Fluid Mech.*, 770:442–457.

Gharib, M., Rambod, E., and Shariff, K. (1998). A universal time scale for vortex ring formation. *J. Fluid Mech.*, 360:121–140.

Glezer, A. (1988). The formation of vortex rings. *Phys. Fluids*, 31(12):3532.

Glezer, A. and Amitay, M. (2002). Synthetic jets. *Annu. Rev. Fluid Mech.*, 34(1):503–529.

Goodfellow, S. D., Yarusevych, S., and Sullivan, P. E. (2013). Momentum coefficient as a parameter for aerodynamic flow control with synthetic jets. *AIAA J.*, 51(3):623–631.

Head, M. R. and Bandyopadhyay, P. (1981). New aspects of turbulent boundary-layer structure. *J. Fluid Mech.*, 107:297–338.

Hearst, R. J. and Ganapathisubramani, B. (2015). Quantification and adjustment of pixel-locking in particle image velocimetry. *Exps. Fluids*, 56(10):191.

Henning, L. and King, R. (2007). Robust multivariable closed-loop control of a turbulent backward-facing step flow. *J. Aircraft*, 44(1):201–208.

Hervé, A., Sipp, D., Schmid, P. J., and Samuelides, M. (2012). A physics-based approach to flow control using system identification. *J. Fluid Mech.*, 702:26–58.

Holman, R., Utturkar, Y., Mittal, R., Smith, B. L., and Cattafesta, L. (2005). Formation criterion for synthetic jets. *AIAA J.*, 43(10):2110–2116.

Hucho, W. and Sovran, G. (1993). Aerodynamics of road vehicles. *Annu. Rev. Fluid Mech.*, 25(1):485–537.

Hussain, A. and Reynolds, W. (1970). The mechanics of an organized wave in turbulent shear flow. *J. Fluid Mech.*, 41:241–258.

Hutchins, N. and Marusic, I. (2007a). Evidence of very long meandering features in the logarithmic region of turbulent boundary layers. *J. Fluid Mech.*, 579:1–28.

Hutchins, N. and Marusic, I. (2007b). Large-scale influences in near-wall turbulence. *Philos. Trans. R. Soc. London Ser. A*, 365(1852):647–64.

Hutchins, N., Monty, J. P., Ganapathisubramani, B., Ng, H. C. H., and Marusic, I. (2011). Three-dimensional conditional structure of a high-Reynolds-number turbulent boundary layer. *J. Fluid Mech.*, 673:255–285.

Hutchins, N., Nickels, T. B., Marusic, I., and Chong, M. S. (2009). Hot-wire spatial resolution issues in wall-bounded turbulence. *J. Fluid Mech.*, 635:103–136.

Jabbal, M. and Zhong, S. (2008). The near wall effect of synthetic jets in a boundary layer. *Int. J. Heat Fluid Flow*, 29(1):119–130.

Jabbal, M. and Zhong, S. (2010). Particle image velocimetry measurements of the interaction of synthetic jets with a zero-pressure gradient laminar boundary layer. *Phys. Fluids*, 22(6):063603.

Jiménez, J., Hultmark, M., and Smits, A. J. (2010). The intermediate wake of a body of revolution at high Reynolds numbers. *J. Fluid Mech.*, 659:516–539.

Kang, Y.-D., Choi, K.-S., and Chun, H. H. (2008). Direct intervention of hairpin structures for turbulent boundary-layer control. *Phys. Fluids*, 20(10):101517.

Kasagi, N., Suzuki, Y., and Fukagata, K. (2009). Microelectromechanical systems-based feedback control of turbulence for skin friction reduction. *Annu. Rev. Fluid Mech.*, 41:231–235.

Kim, J. and Bewley, T. R. (2007). A linear systems approach to flow control. *Annu. Rev. Fluid Mech.*, 39(1):383–417.

Kim, K. C. and Adrian, R. J. (1999). Very large-scale motion in the outer layer. *Phys. Fluids*, 11(2):417.

Kim, W., Kim, C., and Jun Jung, K. (2012). Separation control characteristic of synthetic jets depending on exit configuration. *AIAA J.*, 50(3):559–570.

Kiya, M., Shimizu, M., Mochizuki, O., Ido, Y., and Tezuka, H. (1993). Active forcing of an axisymmetric leading-edge turbulent separation bubble. In *3rd AIAA Shear Flow Conference*, number 3245, Orlando, FL, USA. AIAA.

Klewicki, J. (2010). Reynolds number dependence, scaling, and dynamics of turbulent boundary layers. *J. Fluids Eng.*, 132(9):094001.

Lardeau, S. and Leschziner, M. A. (2011). The interaction of round synthetic jets with a turbulent boundary layer separating from a rounded ramp. *J. Fluid Mech.*, 683:172–211.

Lawson, J. M. and Dawson, J. R. (2013). The formation of turbulent vortex rings by synthetic jets. *Phys. Fluids*, 25(10):105113.

Lim, T. T., Lua, K. B., and Thet, K. (2008). Does kutta lift exist on a vortex ring in a uniform cross flow? *Phys. Fluids*, 20(5):051701.

Littlewood, R. P. and Passmore, M. A. (2012). Aerodynamic drag reduction of a simplified squareback vehicle using steady blowing. *Exps. Fluids*, 53(2):519–529.

Luo, Z.-B. and Xia, Z.-X. (2005). The mechanism of jet vectoring using synthetic jet actuators. *Mod. Phys. Lett. B*, 19:1619–1622.

Luo, Z.-B. and Xia, Z.-X. (2008). PIV measurements and mechanisms of adjacent synthetic jets interactions. *Chin. Phys. Lett.*, 25(2):612–615.

Mahesh, K. (2013). The interaction of jets with crossflow. *Annu. Rev. Fluid Mech.*, 45(1):379–407.

Marusic, I., Mathis, R., and Hutchins, N. (2010a). Predictive model for wall-bounded turbulent flow. *Science*, 329(5988):193–196.

Marusic, I., McKeon, B. J., Monkewitz, P. A., Nagib, H. M., Smits, A. J., and Sreenivasan, K. R. (2010b). Wall-bounded turbulent flows at high Reynolds numbers: Recent advances and key issues. *Phys. Fluids*, 22(6):065103.

Mathis, R., Hutchins, N., and Marusic, I. (2009). Large-scale amplitude modulation of the small-scale structures in turbulent boundary layers. *J. Fluid Mech.*, 628:311–337.

Mathis, R., Hutchins, N., and Marusic, I. (2011). A predictive inner-outer model for streamwise turbulence statistics in wall-bounded flows. *J. Fluid Mech.*, 681:537–566.

M'Closkey, R. T., King, J. M., Cortelezzi, L., and Karagozian, A. R. (2002). The actively controlled jet in crossflow. *J. Fluid Mech.*, 452:325–335.

Milanovic, I. M. and Zaman, K. B. (2005). Synthetic jets in crossflow. *AIAA J.*, 43(5):929–940.

Mittal, R. and Rampunggoon, P. (2002). On the virtual aeroshaping effect of synthetic jets. *Phys. Fluids*, 14(4):1533–1536.

Monty, J. P., Dogan, E., Hanson, R., Scardino, A. J., Ganapathisubramani, B., and Hutchins, N. (2016). An assessment of the ship drag penalty arising from light calcareous tubetube fouling. *Biofouling*, 32(4):451–464.

Nagib, H. M., Reisenthel, P. H., and Koga, D. J. (1985). On the dynamic scaling of forced unsteady separated flows. In *AIAA Shear Flow Control Conference*, number 0553, Boulder, CO, USA. AIAA.

Nickels, T. B., Marusic, I., Hafez, S., and Chong, M. S. (2005). Evidence of the k_1^{-1} law in a high-Reynolds-number turbulent boundary layer. *Phys. Rev. Lett.*, 95:074501.

O'Farrell, C. and Dabiri, J. O. (2014). Pinch-off of non-axisymmetric vortex rings. *J. Fluid Mech.*, 740:61–96.

Oxlade, A. R., Morrison, J. F., Qubain, A., and Rigas, G. (2015). High-frequency forcing of a turbulent axisymmetric wake. *J. Fluid Mech.*, 770:305–318.

Perry, A. E. and Chong, M. S. (1982). On the mechanism of wall turbulence. *J. Fluid Mech.*, 119:173–217.

Persoons, T., O'Donovan, T. S., and Murray, D. B. (2009). Heat transfer in adjacent interacting impinging synthetic jets. In *2009 ASME Summer Heat Transfer Conference*, number 88440, San Francisco, CA, USA. ASME.

Rathnasingham, R. and Breuer, K. S. (2003). Active control of turbulent boundary layers. *J. Fluid Mech.*, 495:209–233.

Rosenfeld, M., Rambod, E., and Gharib, M. (1998). Circulation and formation number of laminar vortex rings. *J. Fluid Mech.*, 376:297–318.

Roupassov, D. V., Nikipelov, A. A., Nudnova, M. M., and Starikovskii, A. Y. (2009). Flow separation control by plasma actuator with nanosecond pulsed-periodic discharge. *AIAA J.*, 47(1):168–185.

Saffman, P. and Baker, G. (1979). Vortex interactions. *Annu. Rev. Fluid Mech.*, 11:95–122.

Sano, M., Suzuki, I., and Sakuraba, K. (2009). Control of turbulent channel flow over a backward-facing step by suction. *J. Fluid Sci. Technol.*, 4(1):188–199.

Sau, R. and Mahesh, K. (2008). Dynamics and mixing of vortex rings in crossflow. *J. Fluid Mech.*, 604:389–409.

Savill, A. and Mumford, J. (1988). Manipulation of turbulent boundary layers by outer-layer devices: skin-friction and flow-visualization results. *J. Fluid Mech.*, 191:389–418.

Schoppa, W. and Hussain, F. (1998). A large-scale control strategy for drag reduction in turbulent boundary layers. *Phys. Fluids*, 10(5):1049.

Schultz, M. P. (2007). Effects of coating roughness and biofouling on ship resistance and powering. *Biofouling*, 23(5):331–341.

Sciacchitano, A., Neal, D. R., Smith, B. L., Warner, S. O., Vlachos, P. P., Wieneke, B., and Scarano, F. (2015). Collaborative framework for PIV uncertainty quantification: comparative assessment of methods. *Meas. Sci. Technol.*, 26(7):074004.

Shariff, K. and Leonard, A. (1992). Vortex rings. *Annu. Rev. Fluid Mech.*, 24:235–279.

Shuster, J., Pink, R., McEligot, D., and Smith, D. (2005). The interaction of a circular synthetic jet with a cross-flow boundary layer. In *35th AIAA Fluid Dynamics Conference and Exhibit*, number 4749, Toronto, CA. AIAA.

Smith, B. L. and Glezer, A. (1998). The formation and evolution of synthetic jets. *Phys. Fluids*, 10(9):2281–2297.

Smith, B. L. and Glezer, A. (2002). Jet vectoring using synthetic jets. *J. Fluid Mech.*, 458:1–34.

Smith, B. L. and Glezer, A. (2005). Vectoring of adjacent synthetic jets. *AIAA J.*, 43(10):2117–2124.

Smith, D. R. (2002). Interaction of a synthetic jet with a crossflow boundary layer. *AIAA J.*, 40(11):2277–2288.

Smits, A. J., McKeon, B. J., and Marusic, I. (2011). High Reynolds number wall turbulence. *Annu. Rev. Fluid Mech.*, 43(1):353–375.

Sumner, D., Heseltine, J. L., and Dansereau, O. J. P. (2004). Wake strudcture of a finite circular cylinder of small aspect ratio. *Exps. Fluids*, 37:720–730.

Talamelli, A., Persiani, F., Fransson, J. H. M., Alfredsson, P. H., Johansson, A. V., Nagib, H. M., Ruedi, J.-D., Sreenivasan, K. R., and Monkewitz, P. A. (2009). CICLoPE–a response to the need for high Reynolds number experiments. *Fluid Dyn. Res.*, 41:021407.

Tropea, C. (2007). *Springer Handbook of Experimental Fluid Mechanics*. Springer.

Van Buren, T., Beyar, M., Leong, C. M., and Amitay, M. (2016a). Three-dimensional interaction of a finite-span synthetic jet in a crossflow. *Phys. Fluids*, 28(3):037105.

Van Buren, T., Leong, C. M., Whalen, E., and Amitay, M. (2016b). Impact of orifice orientation on a finite-span synthetic jet interaction with a crossflow. *Phys. Fluids*, 28(3):037106.

Van Buren, T., Whalen, E., and Amitay, M. (2014a). Vortex formation of a finite-span synthetic jet: effect of rectangular orifice geometry. *J. Fluid Mech.*, 745:180–207.

Van Buren, T., Whalen, E., and Amitay, M. (2014b). Vortex formation of a finite-span synthetic jet: High Reynolds numbers. *Phys. Fluids*, 26:014101.

Vukasinovic, B., Rusak, Z., and Glezer, A. (2010). Dissipative small-scale actuation of a turbulent shear layer. *J. Fluid Mech.*, 656:51–81.

Wen, X., Tang, H., and Duan, F. (2015). Vortex dynamics of in-line twin synthetic jets in a laminar boundary layer. *Phys. Fluids*, 27(8):083601.

Yang, A.-S. (2009). Design analysis of a piezoelectrically driven synthetic jet actuator. *Smart Materials and Structures*, 18(12):125004.

Yoshioka, S., Obi, S., and Masuda, S. (2001). Organized vortex motion in periodically perturbed turbulent separated flow over a backward-facing step. *Int. J. Heat Fluid Flow*, 22:301–307.

Zhou, J., Tang, H., and Zhong, S. (2009). Vortex roll-up criterion for synthetic jets. *AIAA J.*, 47(5):1252–1262.